

**GALLIUM NITRIDE RESONATORS FOR INFRARED DETECTOR
ARRAYS AND RESONANT ACOUSTOELECTRIC AMPLIFIERS**

by

Vikrant Jayant Gokhale

A dissertation submitted in partial fulfillment
of the requirements for the degree of
Doctor of Philosophy
(Electrical Engineering)
in the University of Michigan
2014

Doctoral Committee:

Assistant Professor Mina Rais-Zadeh, Chair
Professor Yogesh Gianchandani
Professor Katsuo Kurabayashi
Professor Euisik Yoon

© Vikrant Jayant Gokhale

All rights reserved

2014

To
Family, Friends, and Teachers

Acknowledgements

First and foremost I would like to thank my advisor, Professor Mina Rais-Zadeh, for providing me the opportunity to pursue this research and supporting me through the years. Her help and advice have been instrumental in achieving the results I write about in this dissertation. I also thank my thesis committee members, Professor Yogesh Gianchandani, Professor Katsuo Kurabayashi, and Professor Euisik Yoon for their help and support as teachers and for the insightful comments I received from them regarding my research.

I would like to take this opportunity to thank my group members in the Resonant MEMS group. From the day we started our research, Yonghyun, Zhengzheng and Vikram were the best of colleagues and friends. In subsequent years, Azadeh, Adam and more recently Muzhi, Cesar, and Feng have continued that tradition. I was ably supported by Yu Sui and Paul Myers, who worked with me for more than a year each. I will be forever grateful for their help and support and for providing a friendly and conducive research environment in the lab.

WIMS, the umbrella organization for research in Microsystems at the University of Michigan, has played a strong role in my development as a MEMS researcher. This work has benefited profusely due to the ancillary support provided through WIMS to student members. Interactions with other WIMS students at official and semi-official events have broadened the scope of my technical knowledge.

This work would not have been complete without the support, guidance and the patience of the Lurie Nanofabrication Facility staff. I would like to thank them for

bearing with me through the years and supporting my research efforts in the cleanroom. I would also like to thank my colleagues from other research groups for providing company, moral support, and process training in the cleanroom. The long nights spent in the cleanroom were enjoyable to a large part due to their support and friendship.

My friends at Michigan, many who started at the same time as I, have been a constant source of support and camaraderie. Without them I would not have made it through the long years. My friends from my time at the Vellore Institute of Technology, in India, where I did undergraduate studies have remained my best friends; extending their support for over ten years and from half a world away.

I would like to thank my extended family in Chicago who provided me a home away from India whenever I wanted.

My girlfriend Lindsay has supported me, encouraged me, and helped me through the tougher times for the last three years. Meeting her was one of the best things that happened to me in Michigan. I cannot express how grateful I am for her being there for me. Last and definitely not the least, I want to express my deepest gratitude and love to my parents and brother who have always encouraged me to pursue my goals and had the fullest confidence that I would succeed in my endeavors.

Table of Contents

Dedication	ii
Acknowledgements.....	iii
List of Figures	ix
List of Tables	xxviii
List of Abbreviations	xxix
ABSTRACT	xxxii
Chapter 1 Introduction.....	1
1.1. Infrared Detectors: A Brief History	1
1.2. Uncooled Infrared Detectors	2
1.3. Uncooled Resonant Infrared Detectors	4
1.4. Comparison of Resonant Detectors with Contemporary Technology	5
1.5. Basic Principles of Operation of Devices in This Work	7
1.5.1. Resonant Detector.....	8
1.5.2. IR Absorbing Coatings and Structures	10
1.5.3. Differential Operation and Detector Arrays	12
1.6. Characterization of GaN Resonators.....	14
1.7. Phonon-Electron Loss in GaN Resonators.....	15
1.8. Acoustoelectric Amplification in GaN BAW Resonators.....	17
1.9. Contributions.....	18
1.10. Organization of the Thesis	19

Chapter 2	Resonant IR Detectors and Arrays	21
2.1.	Theoretical Model and Resonator Design.....	21
2.1.1.	Thermal Dependencies of Resonator Frequency.....	23
2.1.2.	Design for Low NETD	27
2.1.3.	Thermal Design of the Resonator Element.....	31
2.2.	Prototype Detectors and Sense-Reference Pairs	34
2.2.1.	Fabrication Process.....	34
2.2.2.	Prototype Measured Results	35
2.2.3.	Differential Sensing.....	37
2.3.	Resonant IR Detector Arrays	41
2.3.1.	Measured Results of Small Formal Arrays.....	43
2.3.2.	Response Time	46
2.4.	IR Detector Arrays using Other Materials	48
2.4.1.	AlN	49
2.4.2.	AlN-on-Si	50
2.4.3.	PZT-on-SiO ₂	51
2.5.	Expected Performance for Various Material Combinations	52
2.5.1.	Dynamic Range	52
2.5.2.	Temperature Coefficients of Offset & Sensitivity.....	54
2.5.3.	Packaging of Imaging Cores.....	54
2.5.4.	Expected Performance for Various Material Combinations.....	55
2.6.	Broadband CNT-ND Nanocomposite Absorbers.....	58
2.6.1.	Motivation: Thin, Broadband IR Absorbers.....	58
2.6.2.	Fabrication of CNT/DND/Polymer Nanocomposite	59
2.6.3.	Measured IR Absorption	62
2.7.	Narrowband Spectrally-Selective Plasmonic Metamaterial Absorbers	65
2.7.1.	Motivation	65
2.7.2.	Theory and Design.....	66
2.7.3.	Fabrication and Characterization.....	67

Chapter 3	Characterization of GaN Resonators.....	70
3.1.	Need for Electromechanical Characterization of GaN.....	70
3.2.	Epitaxial GaN films.....	71
3.2.1.	Epitaxial Growth.....	71
3.2.2.	Crystal Quality.....	72
3.2.3.	Dry Etching of GaN.....	73
3.3.	Electromechanical Properties of GaN.....	74
3.3.1.	Elastic and Hardness Moduli.....	74
3.3.2.	Acoustic Properties.....	75
3.4.	Performance Metrics for GaN Resonant Devices	77
3.4.1.	Quality Factor and $f \times Q$ Limits.....	77
3.4.2.	Coupling Efficiency and the $k_{eff}^2 \times Q$ Metric.....	79
3.4.3.	Temperature Coefficient of Frequency.....	81
3.4.4.	Power Handling and IIP_3	82
Chapter 4	Phonon-Electron Interactions in Piezoelectric-Semiconductor BAW Resonators	84
4.1.	Theory of Acoustoelectric Amplification in Resonators.....	86
4.1.1.	Standing Waves in Resonators	86
4.1.2.	Frequency Dependence of Gain and Loss	93
4.1.3.	Other Loss Mechanisms in Piezoelectric Semiconductor BAW Resonators ..	96
4.1.4.	Influence on Total Intrinsic Q	98
4.1.5.	Limiting Values of $f \times Q$ product	99
4.2.	Experimental Findings	102
4.2.1.	Fabrication.....	102
4.2.2.	Measurement Procedures and Controls	102
4.2.3.	Analytical Extraction of Q_m	105
4.2.4.	Equivalent Electrical Model Fitting	107

4.3. Comparison of Experimental Data and Models	109
4.4. Material Dependencies for Acoustoelectric Loss/Gain.....	111
4.5. Experimental Controls.....	117
4.5.1. Effect of Contact Non-Linearity.....	117
4.5.2. Effect of RF power	119
4.5.3. Effect of Temperature.....	120
4.6. Potential Materials for Acoustoelectric Amplification	122
4.7. Limits of Acoustoelectric Amplification.....	124
4.8. Discussion	126
Chapter 5 Summary and Future Work.....	128
5.1. Summary	128
5.2. Future Research Directions	129
5.2.1. Resonant IR Detector Arrays.....	129
5.2.2. AlN-on-SiO ₂ with SiO ₂ Tethers.....	131
5.2.3. Readout Circuits	133
5.2.4. Characterization using a Blackbody Source.....	134
5.2.5. Quality Factor Improvement and its Effect on IR Sensitivity.....	135
5.2.6. Loss Mechanisms in Resonators.....	136
Appendix A- Derivation of Phonon-Electron Interactions for Travelling Waves in Piezoelectric Semiconductors	138
Bibliography	149

List of Figures

Fig. 1.1: (a) Schematic of a photonic infrared detector using a mercury cadmium telluride material system. Detection of IR radiation depends on the bandgap transition in the semiconductor upon irradiation. For best results, the device must be cooled to low temperatures. (b) Schematic of a microbolometer with silicon nitride membrane coated with a vanadium dioxide layer. Vanadium dioxide changes its resistance as a function of temperature, thus imparting this structure the ability to sense heat absorbed due to infrared radiation. This is a popular design, and has proven performance as a low cost uncooled detector. Images from [1]. 3

Fig. 1.2 : Comparison of contemporary, commercially available IR imagers using uncooled bolometer arrays. Table from a review paper by Niklaus *et al* [6]. 6

Fig. 1.3 : (a) The resonant IR detector is a thin-film micromechanical resonator mechanically suspended by thin tethers. The resonator body accounts for most of the thermal mass of the device, while the tethers isolate the resonator thermally. The resonator is coated with an IR absorber layer that efficiently absorbs incoming radiation. (b) The transduction mechanism can be separated as the absorption of IR radiation resulting in a temperature shift, resulting in a proportional frequency change for the resonator. (c) A depiction of the reduction of frequency of a resonator due to IR illumination. For most materials, increased temperature causes a reduction in frequency. 8

Fig. 1.4 : Schematic showing the absorption, transmission and reflection of infrared radiation by an IR absorber coating on the resonator substrate. The absorption can be

broadband over a large spectrum, or designed to be narrowband at a specific wavelength, based on the intended application. Within the absorption band, the goal is to increase absorption while reducing transmission and reflection. Both broadband and narrowband absorbers are experimentally demonstrated in this work..... 11

Fig. 1.5 : (a) Schematic of the conceptual approach to differential resonant IR sensing. A sense-reference resonator pair is shown. Upon IR irradiation, the sense resonator, which is coated with an IR absorbing layer, undergoes a frequency shift, while the reference resonator does not absorb radiation and remains frequency-invariant. (b) A representative circuit that can be used for differential measurement. Both resonators are used in identical feedback loops as self-sustaining oscillators. The oscillator signals are mixed together and the beat frequency is extracted. The beat frequency is a function of the IR signal power, but eliminates common mode signals such as temperature drift. The effective sensitivity of the differential signal is larger than that of a single sensor..... 13

Fig. 1.6 : (a) A scanning electron microscope (SEM) image of a fabricated array of 4×4 resonators. Bilayer routing is seen here and can be replaced by flip-chip bonding with a readout IC. (b) A schematic showing the FPA composed of a number of resonant IR detectors. The focusing optics are standard equipment for FPAs and depend on the spectral range to be detected. 14

Fig. 1.7 : (a) Intrinsic material $f \times Q$ limits for GaN-based BAW resonators. For longitudinal acoustic wave resonators, the dominant loss mechanisms are phonon-phonon loss and phonon-electron loss. The electron loss is highly dependent on the free carrier

concentration in the material. Based on analytical values, it is possible that the phonon-electron scattering is significant or even dominant for GaN (b) Measured $f \times Q$ values for GaN resonators (red dots) in comparison with the theoretical limits provide qualitative validation of this hypothesis. 16

Fig. 1.8 : Schematic showing the simple experimental setup and the effect of acoustoelectric amplification on the performance of GaN resonators. (a) Acoustoelectric amplification in GaN resonators can be seen by applying a DC bias to the device during normal RF operation. (b) We see an improvement in Q and insertion loss (IL) and a narrowing of the bandwidth of the device. This is a dynamic improvement and can be switched on/off or tuned during operation. Measured results shown later exhibit up to 35% improvement in Q , with DC bias values as low as 20 V. This thesis proves that the measured performance improvement is due to the acoustic gain resulting from phonon-electron gain in piezoelectric semiconductor BAW resonators, and eliminates all other potential causes by careful experimental controls. 17

Fig. 2.1 : (a) General model of a thermal IR detector. Image from [1]. (b) Scanning electron micrograph image of a released two-port GaN resonator with dimensions of $80 \mu\text{m} \times 80 \mu\text{m} \times 12 \mu\text{m}$. The suspended membrane acts as the IR radiation collector, while thermally connected to the substrate (thermal sink) only by the mechanical tethers which have a low thermal conductance by virtue of their thin and long structure, and ideally the use of material that possess low thermal conductivity..... 22

Fig. 2.2 : Predicted values of resonant frequency change due to electrostriction in GaN. This calculation assumes a 2.15 μm thick film and a pyroelectric coefficient of value 1×10^5 V/m-K. The accurate value of M_{31} is not known and an approximate, conservative value is used. This plot is derived based on the theoretical model for electrostriction in GaN [55]. 26

Fig. 2.3: The modeled NETD design space as a function of the GaN resonator area and the total thermal conductance between the GaN resonator and its surroundings. This particular graph assumes ideal absorption. The radiation limit denotes the point at which radiation losses dominate the heat loss. When not limited by radiation, the tether conductance and detector area are the two most important design parameters for determining the NETD. This graph assumes $f/1$ optics with 80% transmissivity, a pixel fill factor β of 80% and ideal IR absorption η . Frequency instability is assumed to be 10^{-10} 30

Fig. 2.4 : Examples of fabricated resonators show the evolution of the tether design for high thermal isolation, while retaining the total area occupied by the resonator ‘pixel’. This is generally achieved by using bent or meandered tethers that increase effective length. The SEM images show (a) a prototype with simple, short tethers, (b) a tether-suspended thickness mode FBAR, (c) a resonator with single-bend crableg tethers, and (d) a resonator with a two-bend crableg tether. Fabrication and characterization of these resonators are presented in subsequent sections of this chapter. 33

Fig. 2.5 : Fabrication process flow for GaN resonator prototypes. The GaN films are lithographically patterned to define the resonator. Top electrodes are defined by e-beam evaporation and liftoff. After the IR absorber layer is patterned, the resonator is released using through-wafer DRIE. Sputtered metal is used for the back electrode..... 35

Fig. 2.6 : (a) Schematic showing the IR measurement setup of the GaN resonant sensors. Both sensor and reference resonators are measured using an identical procedure. (b) The radiant power output of the source/optical fiber system as per vendor specifications [69], and the absorption efficiency of the silicon nitride layer, measured using NIR spectroscopy. The boxed area is the spectral region that describes the NIR radiation absorbed by the sense resonators. 36

Fig. 2.7 : (a) An SEM image of a fabricated GaN resonator with silicon nitride absorber. The dimensions of the device are $120\ \mu\text{m} \times 80\ \mu\text{m} \times 2.15\ \mu\text{m}$. (b) A comparison of the nominal and irradiated RF (transmission and reflection) performance of the resonator with $156\ \mu\text{W}$ of incident power ($\sim 30\ \mu\text{W}$ of absorbed power). All the relevant operating parameters (frequency, Q , IL, and bandwidth) of the resonator change simultaneously. 36

Fig. 2.8 : (a) Measured data for the sense and reference resonator pair, showing the response upon IR illumination with $156\ \mu\text{W}$ of radiated IR power ($\sim 30\ \mu\text{W}$ of absorbed power). Note that the span of the Y axis is the same for both graphs, and thus in comparison to the sense resonator, the reference resonator is almost invariant upon IR irradiation. (b) The beat frequency change upon IR irradiation. Relative change in the beat frequency when the IR signal of $156\ \mu\text{W}$ is turned ON is about 15%. This is much

larger than the relative change of the sense resonator alone. Using this differential measurement also eliminates common mode signals such as ambient temperature changes, acceleration sensitivity, and pressure sensitivity. 40

Fig. 2.9 : SEM images of successfully fabricated 2×2 arrays ((a) and (b)) and 4×4 arrays ((c) and (d)) with local reference resonators. 43

Fig. 2.10 : (a) Measured response of all the first length extensional mode resonance for the 80 μm × 80 μm resonator array shown in Fig. 2.11. (b) Magnified range shows that the reference resonator has a slightly different frequency and IL than the sense resonators. This is expected due to the mass loading and stress caused by the silicon nitride absorber layer. The sense resonators themselves have near-identical performance, with a standard deviation of 0.0037% (37 ppm) with respect to the average. 44

Fig. 2.11 : (a) 2 × 2 resonator array. Each resonator has dimensions of 80 μm × 80 μm. Three sense resonators are coated with 200 nm thick SiNx absorber layers. The reference resonator is uncoated. (b) Color map indicating the relative change in beat frequency for the 2 × 2 resonator array. The reference resonator is the baseline, while the three sense resonators show as much as a -5.5 % shift in the relative beat frequency upon illumination with 102 μW incident IR power (~20.4 μW absorbed power). 45

Fig. 2.12 : (a) SEM image of a fabricated 4 × 4 resonator array. Each resonator has dimensions of 28 μm × 38 μm. Twelve sense resonators are coated with 200 nm thick SiNx absorber layers. The four reference resonators (at the corners of the array) are

uncoated. (b) Color map indicating the relative change in beat frequency for the 4×4 resonator array with $\sim 30 \mu\text{W}$ incident IR power. The reference resonators are the baseline, while the sense resonators show as much as a -1.6 % shift in the relative beat frequency upon illumination. 46

Fig. 2.13 : (a) S_{21} amplitude of the sense resonator under switched near-IR illumination. Measurements are acquired at high speeds to measure the resonator response. Magnified ranges showing cooling and heating time constants based on measured data and curve fitting using double exponential functions to extract the thermal time constants. The slow time constant is due to the non-ideal substrate and surroundings, while the fast time constant ($556 \mu\text{s}$) is a function of the thermal properties of the sensors. The calculated time constant for this device is $270 \mu\text{s}$ [63]. 47

Fig. 2.14 : (a) Array of AlN-based designs, with single-bend crableg designs. The devices are mechanically released using XeF_2 . This particular batch was also used as a platform for integrating spectrally selective plasmonic IR absorbers, details of which are provided in Section 2.7 (b) The AlN arrays were successfully fabricated and characterized, and found to have good performance as resonators and IR detectors. 49

Fig. 2.15 : (a) Measured response of an AlN-on-Si resonator fabricated using a commercial foundry MEMS process. The mechanical performance of the resonator is one of the best achieved so far, with a measured frequency (42 MHz) close to the design value (44 MHz), low IL (-12 dB) and high Q (1950). Inset shows a microscope image of the device. The MEMS dies have been bonded at the wafer level to CMOS ROICs for

routing and pinout. (b) The IR response of the device when illuminated by $\sim 96 \mu\text{W}$ of power. The response time was separately calculated to be on the order of 4 ms. 50

Fig. 2.16 : (a) An SEM image of the PZT-on-SiO₂ IR detector arrays developed in collaboration with ARL. The tethers only have low thermal conductivity materials such as PZT, SiO₂, and thin Pt. (b) While the resonators were found to be working, there is a lot of room for improvement in terms of performance and stability. (c) IR response of the one of these device, coated with PECVD SiN_x, when exposed to $\sim 70 \mu\text{W}$ of absorbed power. The drift of the resonator frequency needs to be addressed. This is part of ongoing and future work..... 51

Fig. 2.17 : Normalized calculated linear response range and the input dynamic range for a resonant IR detector with a surface area of $80 \mu\text{m} \times 80 \mu\text{m}$, and an absorber efficiency of 100%. Input dynamic range is defined as the range of temperatures that the device can detect with a response that is 1% linear or better. Increasing the thermal conductance of the tethers improves the maximum linear sensing temperature, at the expense of NETD. The dynamic range is limited by the linearity of the radiative heating process and the linearity of the thermal dependence of frequency..... 53

Fig. 2.18: Predicted NETD of fabricated GaN resonant IR detectors (blue circles), with predicted performance improvements using optimized tether materials and designs (green circles) and with absorber efficiency $>99\%$ (red circles). The use of composite tethers and high efficiency absorbers can allow low NETD ($5 \text{ mK} - 10 \text{ mK}$) with small area ($\sim 100 \mu\text{m}^2$). 56

Fig. 2.19 : The expected NETD values as a function of the (a) tether conductance and (b) resonator area for different material combinations and designs that were part of this work. With resonators made from single, high thermal conductivity materials such as GaN or AlN, it is possible to achieve NETD lower than 100 mK, as seen in the measured results. The AlN-on-Si devices have low NETD but are larger in size due to the limitations of the foundry process used to fabricate them. It can be seen that achieving low NETD with both small area and low *G_{tether}* is possible with composite material stacks. 56

Fig. 2.20 : (a), (b) Large agglomerates seen in the CNT/polymer films without the charged DND particles. (c) A SEM image of a thin film of CNT/DND in the PMMA matrix, showing that CNTs are stably enmeshed in the film with the addition of charged DNDs. (d) Magnified image of the same layer as (c), showing the grid like structure of the film. (e) Dispersion mechanism of CNT bundles by charged DND clusters via debundling and dispersion in a polymer/solvent mixture [93]. The dispersion remains stable and the CNTs remain separated even when the volatile liquid solvent evaporates and the polymer/CNT is baked into a solid film. 62

Fig. 2.21: A schematic of the normal incidence transmission and reflection test setup. The measurements are normalized using uncoated glass substrates for transmission and a standard gold reference for reflection. 63

Fig. 2.22 : (a) The reflection, transmission, and the absorption of the 1600 nm and 2000 nm films. The average absorbance for both films is ~95% across the entire spectral region.

(b) Transmission measurement for a 2000 nm thick layer of PMMA on a glass substrate, indicating that the PMMA itself does not contribute significantly to the IR absorption. . 64

Fig. 2.23 : (a) Extracted effective n for the measured films. (b) Extracted effective k for these films is more than 10 \times higher than that for aligned CNT forests, resulting in increased absorption in a significantly lower thickness..... 65

Fig. 2.24 : (a) Simulated EM field confinement for the MIM structure used as the selective plasmonic absorber. The design is for a maximum absorption in the LWIR spectrum, at a wavelength of 10.15 μm . (b) Measured data acquired using a spectrometer, compares favorably with simulation with respect to wavelength, but the absorption magnitude has room for improvement. Inset shows the polarization angle dependence of the grating absorbers. 68

Fig. 2.25 : (a) A SEM image of an array of resonant IR detectors with three sense resonators covered with the MIM plasmonic structures and one uncoated reference. (b) & (c) Magnified SEM images showing the well-defined plasmonic grating with 750 nm wide strips and fabricated gap of 90 nm (design value was 100 nm). (d) Frequency response of a 30 μm \times 14 μm AlN+plasmonic resonant detector to human hands (~ 30 $^{\circ}\text{C}$) briefly held 10 cm above the detector, and a heated solder tip at (~ 260 $^{\circ}\text{C}$), Both thermal sources change the resonant IR detector response. This is the first measured result for LWIR plasmonic absorbers integrated with resonant detectors. 69

Fig. 3.1: (a) Cross-section SEM images of a cleaved GaN film grown on a Si (111) substrate. A transition or buffer layer of AlN and $\text{Al}_x\text{Ga}_{1-x}\text{N}$ is necessary in order to reduce the lattice mismatch between the Si and GaN crystals. This buffer layer is seen in the SEM image. (b) Schematic of the GaN wafer along with optical images of each layer after etching down using dry etching. The transition from the polycrystalline AlN nucleation layer to the single crystal GaN can be clearly seen. 71

Fig. 3.2: A representative result showing XRD spectroscopy on a GaN thin film grown on a Si (111) substrate using MOCVD. Inset: Rocking curve of the (0002) GaN plane exhibits a very clear peak and a FWHM of 1296 arcsec. 72

Fig. 3.3: Calculated slowness curves for GaN for in-plane and out-of-plane acoustic wave propagation. The green shaded regions indicate the slowness values extracted from the frequency of resonators in this work and reported in [64, 91, 108, 111, 126-128]. The measured velocities match well with theoretical estimates. 76

Fig. 3.4: The best Q measured in our lab was on a $40\ \mu\text{m} \times 80\ \mu\text{m}$ length-extensional mode GaN resonator. The RF transmission (S_{21} curve) at room temperature and ambient pressure is shown in red, showing a Q of 8113. The Q improves to 12185 at 77 K and 10 μTorr . IL also improves at the lower temperature and pressure, while frequency increases. 78

Fig. 3.5: Calculated values of the $f \times Q$ limits for the dominant intrinsic dissipation mechanisms in GaN. Measured results from this work are shown in red dots. The

measured values compare favorably with work by other researchers [126, 127, 133-135].

..... 79

Fig. 3.6: Measured values of (a) $keff2$ as a function of Q and (b) $keff2 \times Q$ as a function of frequency. Data are consistent with published work by other researchers [64, 126, 127, 142]. 81

Fig. 3.7: The change in the frequency of two length-extensional GaN resonators as a function of temperature, showing a negative TCF with experimentally measured values of ~ -17 ppm/K. 82

Fig. 3.8: Measured IIP_3 for a GaN mechanical resonator. The data are measured on a 2.1 GHz with a frequency separation of 5 KHz. The measured GaN bulk acoustic wave resonator shows Q of ~ 500 83

Fig. 4.1 : (a) Schematic cross-section of a piezoelectric semiconductor BAW resonator, depicting the fundamental thickness mode of vibration. The schematic indicates the various intrinsic loss mechanisms (phonon-phonon scattering, TED and phonon-electron scattering) in addition to the reflection losses. In the absence of other external losses, such as air damping, the total energy loss per cycle is dominated by these loss mechanisms. For a piezoelectric semiconductor material, under the right conditions, the phonon-electron scattering losses can be inverted to achieve acoustoelectric gain. (b) A representative set of output responses for BAW resonators, denoting damped, undamped, and amplified responses ($\alpha > 0$, $\alpha = 0$, and $\alpha < 0$ respectively). (c) The same

responses can be visualized by the strain distribution of BAW resonator cross-sections under ideal, damped and amplified conditions ($\alpha > 0$, $\alpha = 0$, and $\alpha < 0$ respectively). The cross-section images show higher order standing wave BAW resonance modes, and visually exaggerated damping/amplification envelopes for clarity of concept. The color map shows areas of positive (red) and negative (blue) strain. 93

Fig. 4.2 : (a) The phonon-electron loss/gain in a representative GaN material system with respect to resonant frequency and the velocity ratio η . Increasing the applied electric field (and thus η) reduces the phonon-electron loss across all frequencies. Here, $\eta = 0, 1, 2, \dots$ correspond to electric field values $ED = 0 \text{ kV/m}, 400 \text{ kV/m}, 800 \text{ kV/m} \dots$ as per Eqn. 4.15. Within a certain range of η , the phonon-electron loss is negative, indicating acoustic gain. (b) The total loss in the system is clearly affected by phonon-phonon loss and thermoelastic damping, but still includes regions where loss is negative predicting the possibility of acoustoelectric amplification in the resonator that can theoretically overcome all other intrinsic losses in the material. Note that this is the frequency dependence loss for the piezoelectric semiconductor material, not the resonator. The mechanics of the BAW resonator itself imposes further frequency selectivity, allowing only those modes that conform to the resonance condition $n\lambda = 2L$ 94

Fig. 4.3 : (a) The $f \times Q$ limits for the various intrinsic loss mechanisms in piezoelectric semiconductor GaN ($f = \omega/2\pi$). For low to moderately doped piezoelectric semiconductor GaN, the phonon-electron mechanism is the significant limiting factor, lower than the anharmonic phonon-scattering and TED. (b) For a representative

frequency, (here, 1.5 GHz), the piezoelectrically coupled model for phonon-electron interaction is significant only for a range of values of moderate doping. Beyond this range, other interactions dominate. The $f \times Q$ limit due to phonon-electron interaction is highly dependent on the effective electron concentration. Two important mechanisms of phonon-electron interaction are (c) piezoelectric and (d) deformation-potential (DP) coupling. At low to moderate doping, the piezoelectric interaction dominates, and the two loss mechanisms achieve parity only at a concentration of $\sim 1 \times 10^{18} \text{ cm}^{-3}$ for GaN. 101

Fig. 4.4 : (a) A schematic of a two-port thin film BAW resonator made from epitaxially grown GaN. The resonator is normally driven using only an RF stimulus, but a DC bias applied across the resonant cavity causes a change in the performance. The resonator is seen in (b) a SEM and (c) a microscope image that shows the edge of the released GaN membrane. Scale bar corresponds to 100 μm . (d-e) RF transmission measurements (S_{21}) of the resonator with indicating both nominal operation and the evolution of BAW resonator performance improvement with an increasing DC bias. (f) This improvement can be quantified by the improved IL, decreased bandwidth, and consequently increased Q . (g) The extracted mechanical Q , Q_m , which is free of all parasitic effects. Q_m shows significant improvement with applied DC, demonstrating that there is a fundamental reduction in internal loss and consequently an improvement in the energy confinement in the BAW resonator. 103

Fig. 4.5 : The values of R_m extracted from the measured data for the BAW device shown in Fig. 4.4. The values of Q_m are based on these extracted values. 106

Fig. 4.6 : (a) Cross section electron micrograph of a GaN film epitaxially grown on a Si (111) wafer. (b) In order to mitigate the lattice mismatch between GaN and Si, a graded buffer layer consisting of AlN and AlGa_N layers is used. (c) A modified version of the two-port Butterworth-van Dyke (BVD) model of a resonator can be used to map mechanical quantities with their equivalent motional quantities. The parasitic effect of the buffer layers associated with the body of the resonator and the contact pads has been included for a more accurate fit. The model is symmetric with respect to its ports. 107

Fig. 4.7 : BVD model fit for the RF transmission magnitude and phase of the 1.5 GHz resonator shown in this work. It can be seen that the model provides an accurate match with measured RF transmission parameters. The lumped element values for the 1.5 GHz device used for this fitting are shown in Table 4.II. The transmission response of the resonator at each value of DC bias can be matched using the BVD model and corroborates the lowering of R_m . The value of R_m for this resonator at varying DC bias is shown in Fig. 4.5 108

Fig. 4.8 : Qualitative comparison of the improvement in Q_m for representative resonators on multiple wafers, using the full intrinsic loss model. Approximate estimates for the effective electron concentrations of each wafer are determined using this comparison. Error bars for Wafer C denote the maximum/minimum data over multiple data sets for the same devices. 110

Fig. 4.9 : Measured values of $f \times Q$ for devices above, and the limiting values imposed by the phonon-electron loss. The phonon-electron limits of $f \times Q$ depend on the specific

values of N for each individual wafer. The difference between the $f \times Q$ limit and the measured values is due to reflection loss and other extrinsic losses not accounted for in the model. Reflection loss can be lowered by more optimized resonator design, while other losses can be reduced by reducing the defect density of the material lattice, operating the device in a vacuum and at low temperatures. 111

Fig. 4.10 : (a) Phonon-electron loss/gain $\alpha_{Piezope}$ as a function of frequency and applied DC electric field, for the wurtzite GaN system with a fixed carrier concentration $N = 10^{15} \text{ cm}^{-3}$ and carrier mobility $\mu=200 \text{ cm}^2/\text{V}\cdot\text{s}$. The gain region $\alpha_{Piezope}\omega r, ED < 0$ is clearly seen. Subsequent plots (b)-(e) denote loss $\alpha_{Piezope}$ as a function of ED , at representative frequencies, ω_{max} and 1.5 GHz, with variations in N and μ . The nature of $\alpha_{Piezope}$ is highly dependent on these parameters. A similar analysis can be carried out for other piezoelectric semiconductor materials, in order to identify the optimum material properties and design for low-loss or high-gain resonant piezoelectric semiconductor BAW amplifiers. 112

Fig. 4.11 : The critical velocity ratio η_{th} is the threshold value at which $\alpha_{Piezope} = 0$. Any further increase in the velocity ratio (achieved by applying a higher electric field) would drive the resonator into the gain regime $\alpha_{Piezope} < 0$. The possible solution space for the gain regime (shown shaded here for the wurtzite GaN system under consideration) is dependent on the electronic properties (N, μ) and the resonant frequency. The upper bound for amplification in any real material is set by the electron saturation velocity..... 114

Fig. 4.12 : (a) Relative improvement in Q_m for multiple resonators as a function of frequency and modeled N for four GaN wafers. Planar projections indicate the trends with respect to frequency for a fixed set of material properties (Wafer A). (b) Relative improvement in experimentally measured and extracted Q_m for four BAW resonators concurrently fabricated on Wafer A (and thus possessing the same material properties). As predicted by the model, increasing the resonance frequency ($\omega \rightarrow \omega_{max}$) increases the relative improvement in Q_m . As expected from the model, increasing electron concentration reduces piezoelectrically coupled phonon-electron interactions due to screening, and leads to (c) a higher nominal $f \times Q$ (lower loss) but also (d) a lower relative acoustoelectric improvement in Q_m 116

Fig. 4.13 : (a) DC I-V curves and (b) measured resonator Q for two similarly designed BAW resonators. In both cases, positive voltages result in similar trends in improvement of Q . In devices designated type A, a negative voltage results in negligible Q amplification, while in devices of type B, there is a perceptible change in the Q with a negative bias. This is well correlated with the nature of the DC current seen in both type of devices; devices that do not show large currents in the negative bias region do not show improvements in the Q . Further investigation into the n-GaN/Ti/Au contact is necessary to fully characterize and control contact resistance and consequently the Q amplification with negative DC bias..... 118

Fig. 4.14 : Change in (a) measured Q and (b) IL of the 70 MHz BAW resonator (Wafer A) with applied DC bias at different levels of RF input power. We can see that increasing

the input power temperature improves the Q and IL slightly. (c) & (d) The same data plotted as a function of the RF power, at select values of DC bias. Increasing RF power improves performance slightly, but not significantly when compared to the DC bias... 119

Fig. 4.15 : Change in (a) measured Q and (b) IL of a 70 MHz BAW resonator (Wafer A) with applied DC bias at various temperatures. We can see that elevated temperature reduces the Q and IL. (c) & (d) The same data plotted as a function of the temperature, at select values of DC bias. The reduction in Q improvement at low temperature needs further investigation..... 121

Fig. 4.16 : Potential piezoelectric semiconductor materials for achieving acoustoelectrically amplified BAW resonators. Representative plots for $\alpha SW p e \omega, \eta$ for other piezoelectric semiconductor materials that can potentially exhibit acoustoelectric amplification via piezoelectric interactions between phonons and electrons. Each material is investigated up to the limit η_{sat} set by the respective electron saturation velocity. Other loss mechanisms are not considered here. Material properties used for modeling are provided in Table 4.III. Note that the axes are scaled individually for visual clarity..... 122

Fig. 5.1: A medium format array with 256 pixels. The total area of the FPA is $900 \mu\text{m} \times 900 \mu\text{m}$. High packing density can be achieved in this format by using polysilicon traces. The polysilicon layers will be under the AlN layers, separated by thick isolating oxide layers. The resonators will be released using a dry gas-phase XeF2 etch. 130

Fig. 5.2 : Schematic showing the device cross-section for a composite material thin-film resonator for low NETD IR detection. The structural layer is 300 nm SiO₂, with 250 nm AlN on the resonator plate for actuation, and up to 200 nm of SiN_x for IR absorption. The tethers are comprised of low thermal conductance Ti- SiO₂-Ti. Molybdenum or platinum is used as a seed layer for improving AlN crystal quality, but is not present on the tethers, and does not contribute to thermal conduction. 132

Fig. 5.3 : (a) An SEM image of a fabricated AlN-on-SiO₂ resonant IR detector. (b) The tethers are made solely of SiO₂ and thin Ti in order to reduce the thermal conductance of the tethers. 132

Fig. 5.4 : Schematic showing a Pierce oscillator constructed using a GaN MEMS resonator and a GaN HEMT transistor. The two GaN elements can be co-fabricated on the same substrate, as demonstrated by Ansari *et al* [128]. 134

Fig. 5.5 : A schematic showing the importance of the Q in frequency-shifting resonant sensors. At a given frequency, the sensing resolution (by convention compared at the -dB bandwidth) improves by a factor of Q. All other factors kept constant, the insertion loss also improves, making it easier to interface the sensor with electronics. 136

List of Tables

Table 2.I A Comparison of Resonant IR Detectors in Literature	41
Table 2.II Thermal Properties of Materials.....	57
Table 3.I Process Parameters for ICP Etching of GaN.....	73
Table 3.II Mechanical Stiffness and Hardness Moduli for GaN	75
Table 4.I Material Properties used for Calculating Loss Components in GaN	94
Table 4.II Dimensions and Material Properties for the 1.5 GHz resonator	108
Table 4.III Potential Candidate Materials for Acoustoelectric Amplification.....	123

List of Abbreviations

Abbreviation	Meaning
AlN	Aluminum Nitride
ARL	Army Research Labs
BAW	Bulk Acoustic Wave
CdS	Cadmium Sulphide
CMOS	Complementary Metal Oxide Semiconductor
CNT	Carbon Nanotube
CVD	Chemical Vapor Deposition
CW	Continuous Wave
DC	Direct Current
DND	Detonation Nanodiamond
DRIE	Deep Reactive Ion Etching
FBAR	Film Bulk Acoustic Wave Resonator
FEA	Finite Element Analysis
FPA	Focal Plane Array
FWHM	Full Width at Half Maximum
GaN	Gallium Nitride
HEMT	High Electron Mobility Transistor
IC	Integrated Circuit
IL	Insertion Loss
IR	Infrared
LNF	Lurie Nanofabrication Facility
LTE	Linear Thermal Expansion
LWIR	Long Wavelength Infrared
MBE	Molecular Beam Epitaxy
MEMS	Microelectromechanical Systems

MIM	Metal-Insulator-Metal
MOCVD	Metallo-organic Chemical Vapor Deposition
MWIR	Mid-Wave Infrared
ND	Nanodiamond
NETD	Noise Equivalent of Temperature Difference
NIR	Near Infrared
PECVD	Plasma Enhanced Chemical Vapor Deposition
PMMA	Poly-(methacrylate)
PZT	Lead Zirconia Titanate
Q	Quality Factor
RF	Radio Frequency
ROIC	Readout Integrated Circuit
SEM	Scanning Electron Microscope
SOI	Silicon on Insulator
SPR	Surface Plasmon Resonance
TCE	Thermal Coefficient of Expansion
TCF	Temperature Coefficient of Frequency
TCR	Temperature Coefficient of Resistance
TED	Thermoelastic Damping
TPOS	Thin-film Piezoelectric on Silicon
UHF	Ultra High Frequency
VHF	Very High Frequency
XRD	X-Ray Diffraction
ZnO	Zinc Oxide

ABSTRACT

This thesis work presents the first comprehensive utilization of Gallium Nitride (GaN) in high-performance, high-frequency micromechanical resonators. It presents characterization of critical electromechanical properties of GaN and validation of high-performance designs.

The primary motivation behind this project is the use of GaN resonators as sensitive, low-noise, uncooled infrared (IR) detectors. IR response of micromechanical resonators is based on radiative absorption and a consequent shift in its resonant frequency. Mechanical resonators are expected to perform better than contemporary uncooled IR detectors as the noise equivalent temperature difference (NETD) is primarily limited by each resonator's thermomechanical noise, which is smaller than resistive bolometers. GaN is an ideal material for resonant IR detection as it combines piezoelectric, pyroelectric, and electrostrictive properties that lead to a high IR sensitivity up to -2000 ppm/K ($\sim 100\times$ higher than other materials). To further improve IR absorption efficiency, we developed two types of thin-film absorbers: a carbon nanotube (CNT)-polymer nanocomposite material with broad-spectrum absorption efficiency ($> 95\%$) and a plasmonic absorber with narrow-spectrum absorption ($> 45\%$ for a select wavelength) integrated on the resonator. Designs have also been successfully implemented using GaN-on-Si, aluminum nitride (AlN), AlN-on-Si, and lead zirconate titanate (PZT), and fabricated both in-house and using commercial foundry processes. Resonant IR detectors, sense-reference pairs,

and small-format arrays (up to 16 elements) are successfully implemented with NETD values of 10 mK, and ~ 1 ms-10 ms response times.

This work also presents the first measurements and analysis of an exciting, fairly unexplored phenomenon: the amplification of acoustic standing waves in GaN resonators using electrical energy, boosting the quality factor (Q) and reducing energy losses in the resonator. This phenomenon is based on phonon-electron interactions in piezoelectric semiconductors. Under normal conditions this interaction is a loss mechanism for acoustic energy, but as we discovered and consistently demonstrated, it can be reversed to provide acoustoelectric amplification (resulting in Q -amplification of up to 35%). We present corroborated analytical and experimental results that describe the phonon-electron loss/gain in context with other loss mechanisms in piezoelectric semiconductor resonators. Research into this effect can potentially yield insights into fundamental solid-state physics and lead to a new class of acoustoelectric resonant amplifiers.

Chapter 1 Introduction

1.1. Infrared Detectors: A Brief History

The discovery of the infrared (IR) spectrum is relatively new, with the astronomer William Herschel credited with the detection of infrared radiation in 1800. Herschel's detection system, which is the first thermal IR detector, was a prism that separated the infrared from the visible portions of the spectrum, and a thermometer that absorbed the radiation and showed an increase in temperature [1]. The next hundred years witnessed great advances in the understanding of blackbody radiation (Kirchoff-1860, Stefan-1879, Boltzmann-1884), and some thermal IR detector designs (Langley's bolometer-1878) but few practical implementations of IR detection. It took an understanding of the photoelectric effect (Einstein-1905) and advances in photoconductive materials for the first detectors that showed real promise. A thallium sulfide photonic detector was first used in 1917 to detect an aircraft at the range of 1 mile. This technology proliferated and improved greatly during World War II, with an emphasis on designing photoelectric materials with bandgaps that respond sensitively to the various regions of the IR spectrum [1]. While research on thermal detectors such as thermopiles continued in parallel, it was only in the 1970s, with the demonstration of the Honeywell microbolometer focal plane array (FPA), that

thermal detectors became competitive with photonic detectors [1, 2]. With the licensing of Honeywell's technology in the 1990s, the microbolometer FPAs became the standard for high-volume, low-cost IR detectors with applications ranging from the military, defense and security, medical, healthcare, automotive and consumer markets [1-3].

1.2. Uncooled Infrared Detectors

The IR spectrum ranges from 700 nm to 300 μm . For the purposes of thermography and IR imaging, the useful 'thermal radiation' range of 700 nm to ~ 14 μm is further divided into the near infrared (NIR) from 700 nm to 1.5 μm , the mid-wave infrared (MWIR) from 3 μm to 5 μm , and the long-wave infrared (LWIR) from 8 μm to 14 μm . The unused spectra between these ranges have very low transmission because of atmospheric absorption. Human bodies (at ~ 37 $^{\circ}\text{C}$) emit LWIR radiation, and objects at higher temperatures (industrial equipment, furnaces, missiles, aircraft engines) emit progressively from MWIR to NIR ranges as the temperature increases. This makes the detection of thermal radiation very useful for commercial, industrial, healthcare, military, defense and security applications.

As alluded to in the previous section, there are two main types of IR detectors: photonic detectors and thermal detectors (Fig. 1.1). Photonic detectors depend on bandgap transitions due to photonic excitation in materials specially engineered to respond to certain wavelengths. Although efforts are being made to develop high operating temperature photonic detectors [4], these detectors work best at low

temperatures on the order of 100 K, and require bulky, power hungry cooling equipment. Thermal detectors, as with Herschel's thermometer and Langley's bolometer, depend on the conversion of incident radiation to heat. The wavelength selectivity is solely dependent on the absorption band of the IR absorber coating. The absorbed heat is usually transduced into an electrical signal for measurement and signal processing. Thermal detectors typically do not require cooling and are designed to work at 300 K and higher. In the last decade, there has been a large surge in the number of solutions that use uncooled detectors, primarily due to the fact that cooled photonic sensors, even though they have enhanced sensitivity, require a bulky cooling/refrigeration unit that consumes both space and power in excess of the actual imaging system. The high cost of cooled detectors also makes them unattractive to the growing automotive and consumer market.

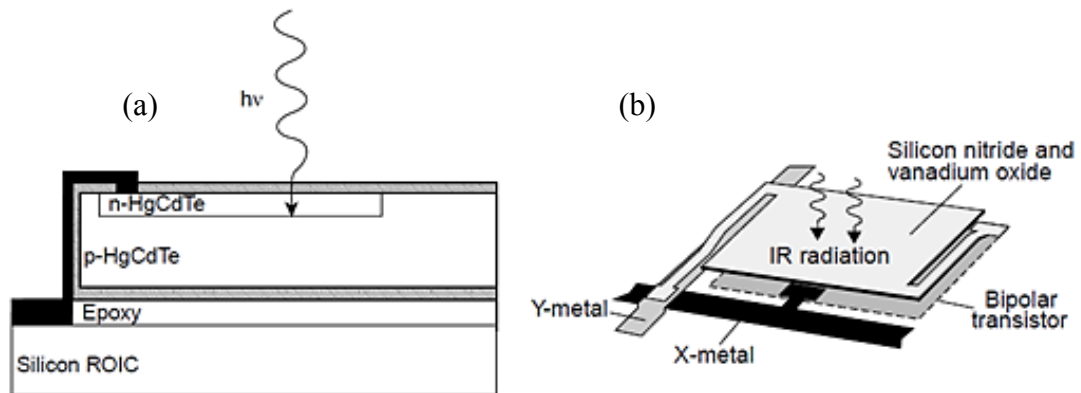


Fig. 1.1: (a) Schematic of a photonic infrared detector using a mercury cadmium telluride material system. Detection of IR radiation depends on the bandgap transition in the semiconductor upon irradiation. For best results, the device must be cooled to low temperatures. (b) Schematic of a microbolometer with silicon nitride membrane coated with a vanadium dioxide layer. Vanadium dioxide changes its resistance as a function of temperature, thus imparting this structure the ability to sense heat absorbed due to infrared radiation. This is a popular design, and has proven performance as a low cost uncooled detector. Images from [1].

Many successful commercial uncooled detector solutions rely heavily on technologies developed in the overall realm of microelectromechanical systems (MEMS) [1, 2, 5-7]. This includes single detectors and FPAs of thermopiles [8], bolometers [5], ferroelectric and pyroelectric vidicons [9]. The small size and low thermal mass of MEMS, along with the ability to fabricate uniform arrays of identical sensors make MEMS one of the most attractive choices of technology.

1.3. Uncooled Resonant Infrared Detectors

While contemporary uncooled IR imagers offer significant advantages in deployment and operational costs, they lag behind cooled photonic detectors in key technical metrics, chiefly the responsivity, the limiting noise levels, response time, and spectral selectivity [1]. This research proposes a relatively new and unexplored technology for uncooled micromechanical IR sensors that can offer high sensitivity and large signal to noise ratio with a small sensing area, along with the fast response time required for continuous video imaging. In the proposed sensor, we use micromechanical resonators that respond to IR radiation by a shift in their resonant frequency. This technology has been proposed by Vig and Kim [10, 11] to be a way to make high sensitivity, low noise IR detectors. Unlike resistive microbolometers, the limiting noise in micromechanical resonators operating in the 1 MHz – 1 GHz frequency range is due to the thermomechanical noise arising from random thermal fluctuations in the body of the resonator. The critical figure of merit for noise in IR detectors is the noise equivalent of temperature difference (NETD), which denotes the

noise-limited minimum resolvable temperature. Prototypes of such resonant IR detectors were fabricated using quartz in the past [12-14], but this technology was not amenable to making resonator arrays with element size and performance comparable to that of conventional microbolometer arrays. Furthermore, quartz, and in fact, most of the materials that are used for making resonators are dielectrics or wide-bandgap semiconductors and are thus not inherently sensitive to IR radiation. Decoupling the resonator operation from the efficient absorption of IR radiation is the best available solution for resonant IR detection. This can be achieved by coating the resonator surface with a thin film absorber that has a high absorption efficiency.

This work aims at developing micromachined arrays of resonant IR detectors with high sensitivity and low noise, and with absorber layers that efficiently convert IR radiation to heat.

1.4. Comparison of Resonant Detectors with Contemporary Technology

Contemporary state of the art uncooled IR detectors are generally high performance bolometer arrays intended for military and defense applications [1, 2, 5, 6]. A comparison of some commercially available instances is given in a review paper by Niklaus *et al* [6] (Fig. 1.2). It can be seen that the pixel pitch is as low as 17 μm , with NETD values as low as 35 mK.

Company	Bolometer type	Array format (pixels)	Pixel pitch (μm)	Detector NETD (F=1, 20-60 Hz)
FLIR, USA	VO _x bolometer	160x120 - 640x480	25	35 mK
L-3, USA	VO _x bolometer	320x240	37.5	50 mK
	α -Si bolometer	160x120 - 320x240	30	50 mK
BAE, USA	VO _x bolometer	320x240 - 640x480	28	30-50 mK
	VO _x bolometer (standard design)	160x120 - 640x480	R&D: 17	50 mK
DRS, USA	VO _x bolometer (umbrella design)	320x240	25	35 mK
	VO _x bolometer (umbrella design)	320x240	R&D: 17	50 mK
Raytheon, USA	VO _x bolometer	320x240 - 640x480	25	30-40 mK
	VO _x bolometer (umbrella design)	640x512	R&D: 17	50 mK
ULIS, France	α -Si bolometer	160x120, 640x480	25-50	35-100 mK
Mitsubishi, Japan	Si diode bolometer	320x240	25	50 mK
NEC, Japan	VO _x bolometer	320x240	23.5	75 mK
SCD, Israel	VO _x bolometer	384x288	25	50 mK

Fig. 1.2 : Comparison of contemporary, commercially available IR imagers using uncooled bolometer arrays. Table from a review paper by Niklaus *et al* [6].

The NETD of the bolometer based arrays is based on the Johnson noise, $1/f$ noise, thermal fluctuation noise, and noise in the circuitry. The motivation behind the use of resonant IR detectors is that resonators are generally limited by only the thermal fluctuation noise, with significantly lower levels of Johnson noise and $1/f$ noise [15, 16], and as we intend to demonstrate in this work, it is possible to achieve NETD values of under 10 mK using resonant IR detectors. Another important metric is the responsivity of the detector, which is defined as the output signal per unit incident radiation power. This metric is defined by the efficiency of radiation absorption, and the temperature dependencies that generate the output signal as a function of the absorbed heat. Contemporary bolometers use a quarter wavelength resonant cavity to absorb at a particular spectral wavelength, but are limited to 60% - 70% absorption

efficiency. We intend to show that it is possible to achieve $> 95\%$ absorption with novel absorber coatings, and thus boost the responsivity.

The thermal dependence of a bolometer is set by the bolometric material (*i.e.*, the material that changes its resistivity upon heating) that makes up the structural layer of the device. High quality devices use vanadium oxides (VO_2 , V_2O_3 and V_2O_5) that have a temperature coefficient of resistance (TCR) of up to $4\%/K$ under ideal laboratory conditions, but are generally limited to under $2\%/K$ [17]. This is a material property of the vanadium dioxide or any other bolometric material, and can only be improved incrementally. On the other hand, the thermal dependence of resonant IR detectors is determined by its temperature coefficient of frequency (TCF), which is a function of both the material properties and the design of the resonator. We show that it is possible to use resonator materials (such as GaN) that have a very large thermal dependence on temperature change, including both primary and secondary effects. Secondly, it is possible to design a resonator to exhibit higher TCF by designing the internal stress profile [18, 19]. Thus, resonant IR detector technology has the potential to achieve higher responsivity with lower noise and with comparable pixel footprints.

1.5. Basic Principles of Operation of Devices in This Work

We can consider the resonant IR detector to be comprised of two major functional components (Fig. 1.3): the resonant structure and the absorber. The operating principles of each component are discussed in detail separately.

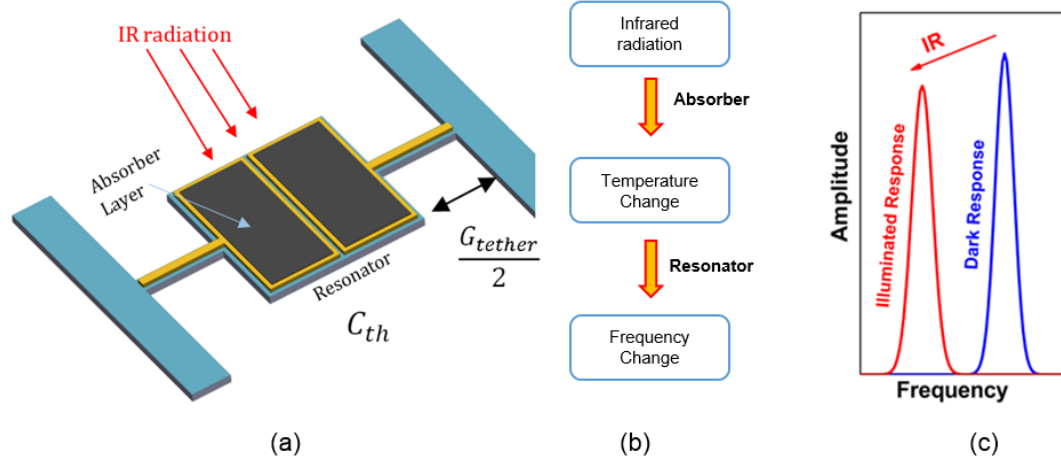


Fig. 1.3 : (a) The resonant IR detector is a thin-film micromechanical resonator mechanically suspended by thin tethers. The resonator body accounts for most of the thermal mass of the device, while the tethers isolate the resonator thermally. The resonator is coated with an IR absorber layer that efficiently absorbs incoming radiation. (b) The transduction mechanism can be separated as the absorption of IR radiation resulting in a temperature shift, resulting in a proportional frequency change for the resonator. (c) A depiction of the reduction of frequency of a resonator due to IR illumination. For most materials, increased temperature causes a reduction in frequency.

1.5.1. Resonant Detector

The resonator is a mechanically suspended structure (Fig. 1.3 (a)) that undergoes mechanical vibration as a result of either self-sustaining and stable oscillation conditions or a driving signal at the natural frequency of resonance. The natural frequency of resonance for micromechanical resonators (Eqn. 1.1) is set by the material properties and dimensions of the structure.

$$f_n = \frac{n}{2\pi} \sqrt{\frac{k_{eff}}{m_{eff}}} \propto \frac{n}{2D} \sqrt{\frac{E}{\rho}} \quad \text{Eqn. 1.1}$$

Here,

f_n is the natural frequency of resonance,

n is the mode of vibration for the resonator,

k_{eff} is the effective elastic stiffness of the resonator,
 m_{eff} is the effective vibrating mass of the resonator,
 L is the critical dimension of vibration of the resonator,
 E is the effective Young's modulus of the material,
 ρ is the mass density of the material.

Since both the material properties and dimensions are temperature-dependent, a change in the temperature of the device results in a proportional change in the frequency of the resonator. The transduction mechanism can be one of a number of mechanisms: capacitive, piezoelectric, thermal, magnetic, etc. In this work we use piezoelectric actuation, primarily using gallium nitride (GaN) for high sensitivity, but also other similar materials and combinations (GaN-on-Si, AlN, AlN-on-Si, and PZT). Most materials used as resonators respond to temperature changes through the temperature coefficient of frequency (TCF), which is in the range of -20 ppm/K to +80 ppm/K depending on the material. GaN is used as the material of choice since it is not only piezoelectric, but it is a strong pyroelectric and electrostrictive material. Changes in temperature cause fast and large changes in the net strain in a GaN layer due to the pyroelectric-electrostrictive mechanisms, leading to frequency shifts as large as -2000 ppm/K.

The tethers mechanically and thermally connect the resonator to the substrate. The thermal conductance of the tethers (G_{tether}) is an important property for optimizing the thermal performance of the device. For high sensitivity and low NETD, the resonator needs to be thermally isolated from the substrate, and thus G_{tether} should be

as low as possible. However, a high G_{tether} also slows down the response time. Therefore, the tether design needs to be optimized for the application in question. The thermal capacitance of the body of the resonator (C_{th}) is also significant for determining the response time, as well as the level of thermomechanical noise in the system. In addition, the material, size, and dimensions of the resonator and its tethers also determine its basic performance as a resonator and thus it is critical to optimize mechanical performance of the device as a resonator and its thermal and noise performance as an IR detector.

1.5.2. IR Absorbing Coatings and Structures

The thin-film absorber coating is needed to provide efficient absorption of incident radiation and conversion into thermal energy [1, 2, 20, 21]. Absorber layers for resonant IR detectors require the following attributes [21]: (i) high and polarization-independent absorption [22], (ii) absorption bandwidth that can be designed to specification and can be made narrow-band or broadband as desired, (iii) low thermal and inertial mass, (iv) good thermal conduction to the resonant detector, (v) stable and reproducible properties, and (vi) process-compatible with detector and electronics fabrication technologies. Fig. 1.4 shows a schematic of the thin-film absorber layer on the resonator substrate, with the fraction of energy absorbed by the layer given by Eqn. 1.2.

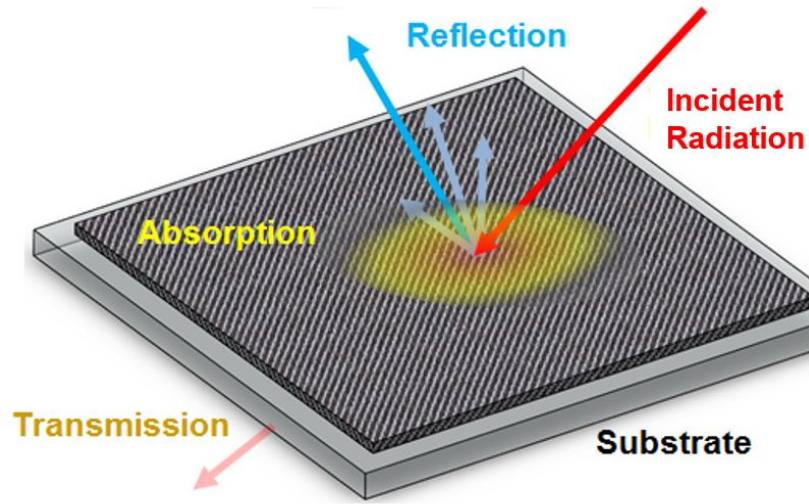


Fig. 1.4 : Schematic showing the absorption, transmission and reflection of infrared radiation by an IR absorber coating on the resonator substrate. The absorption can be broadband over a large spectrum, or designed to be narrowband at a specific wavelength, based on the intended application. Within the absorption band, the goal is to increase absorption while reducing transmission and reflection. Both broadband and narrowband absorbers are experimentally demonstrated in this work.

$$A(\lambda) = 1 - R(\lambda) - T(\lambda), \quad \text{Eqn. 1.2}$$

where

λ is the wavelength of radiation,

A , R , and T are the fractional absorption, reflection, and transmission.

Silicon nitride is widely used as the IR absorbing layer as it is CMOS-compatible and can be deposited at low temperatures. However its absorbance is at best ~80% and limited to a small region of the far-IR spectrum. In order to boost the efficiency of IR detection and to widen the spectral range of the sensor, we develop a new material that is highly absorptive (> 95%) across large parts of the near, mid, and far IR spectra. This material is a nanocomposite comprised of CNTs and nanodiamonds

(NDs) mixed into a polymer matrix for mechanical stability. Additionally such absorbers can be used for solar-thermal energy harvesting [23].

For surveillance applications and thermography, high-efficiency narrow-spectrum absorbers are needed that can isolate certain thermal phenomena (*e.g.*: LWIR absorption to distinguish human forms against a cold background). However, in recent years, there is interest in using multi-spectral and hyperspectral imaging that combines data across various spectra to get a better understanding of the target. This is useful for both surveillance and for remote sensing/astronomy. For photonic sensors, this can be achieved by using materials with different bandgaps. For thermal sensing, this can be achieved by multiple pixels each having an IR absorber layer sensitive to different narrow spectral bands. For this purpose, we design plasmonic metamaterial-based IR absorbers that can be designed to absorb a specific wavelength. The absorbed wavelength is based on the dimensions and material properties of the metamaterial, and can be designed according to the application. Measured results have demonstrated selectivity for a particular wavelength (with an absorption of > 45% and a pass band of 1.5 μm centered around 10 μm) and the ability to integrate these designs on a resonant detector platform.

1.5.3. Differential Operation and Detector Arrays

In order to boost the sensitivity of detection, and at the same time, eliminate the effects of interfering signals such as slow changes in ambient temperature, acceleration, rotation, pressure changes, and background radiation, we use a

differential measurement scheme with a resonant sensor, paired with a reference resonator that is invariant to IR radiation. The sense resonator is coated with the IR absorber, while the reference resonator is coated with a reflective metal that does not absorb IR radiation and thus does not undergo significant frequency shift in response to IR radiation (Fig. 1.5(a)). A number of readout schemes can be implemented to achieve differential sensing for these sense/reference pairs (Fig. 1.5 (b)).

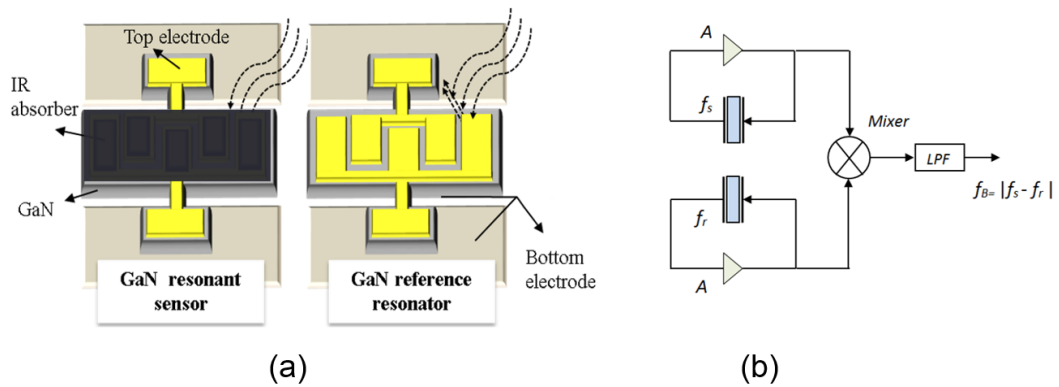


Fig. 1.5 : (a) Schematic of the conceptual approach to differential resonant IR sensing. A sense-reference resonator pair is shown. Upon IR irradiation, the sense resonator, which is coated with an IR absorbing layer, undergoes a frequency shift, while the reference resonator does not absorb radiation and remains frequency-invariant. (b) A representative circuit that can be used for differential measurement. Both resonators are used in identical feedback loops as self-sustaining oscillators. The oscillator signals are mixed together and the beat frequency is extracted. The beat frequency is a function of the IR signal power, but eliminates common mode signals such as temperature drift. The effective sensitivity of the differential signal is larger than that of a single sensor.

A major advantage of thin-film technology and standard MEMS processing techniques is the ability to fabricate not just single resonant IR detector elements (unlike quartz-based resonators), but to batch fabricate large arrays (Fig. 1.6) of identical resonant IR detector ‘pixels’. This is a critical step in achieving parity with conventional microbolometer-based FPAs. While this work has not reached the maturity of industrial FPA design and fabrication, we demonstrate small-format

arrays of up to 16 elements. Ongoing work is aimed at arrays with up to 256 elements. Important practical aspects to be considered while designing arrays are the pixel footprint, the pixel pitch, the routing, and the readout/signal processing scheme. The current limiting factor for the number of elements (in a research lab environment) is the routing design optimization, and not the design or fabrication of the actual resonant detectors. With mature industrial processes such as through-wafer vias or flip-chip bonding to a readout IC, it is possible to extend these designs to larger formats.

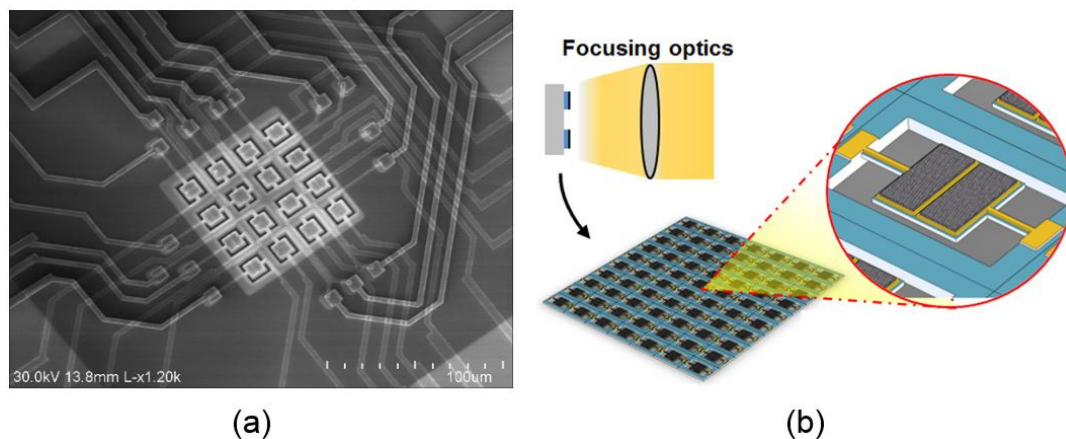


Fig. 1.6 : (a) A scanning electron microscope (SEM) image of a fabricated array of 4×4 resonators. Bilayer routing is seen here and can be replaced by flip-chip bonding with a readout IC. (b) A schematic showing the FPA composed of a number of resonant IR detectors. The focusing optics are standard equipment for FPAs and depend on the spectral range to be detected.

1.6. Characterization of GaN Resonators

In order to develop resonant IR detectors with high sensitivity, this work has pioneered high-frequency GaN-based micromechanical resonators based on extensional modes of vibration. Extensional modes of vibration allow us to reach frequencies ranging from 10 MHz to several gigahertz. As part of this work, a number of GaN resonators were designed, fabricated, and characterized. Important properties

of GaN such as the acoustic velocity, piezoelectric coupling coefficient, TCF, and acoustic loss were characterized. Characterizing these properties is critical to ensure that GaN resonators can be implemented reliably with high performance. Apart from their use as IR detectors, GaN resonators can be integrated homogeneously with GaN electronics to provide a high-frequency, high-power electromechanical signal processing system.

A substantial part of this thesis focuses on investigating acoustic losses in GaN, especially losses due to electrons (GaN is a piezoelectric semiconductor), and an interesting phenomenon: acoustic gain in GaN due to the acoustoelectric effect [24].

1.7. Phonon-Electron Loss in GaN Resonators

Bulk acoustic wave (BAW) resonators of the type discussed in this thesis rely on acoustic waves (phonons) trapped in the elastic cavity defined by the material. While ideal standing-wave BAW resonators are lossless, the energy confinement in practical materials is not ideal due to attenuation occurring via a number of phonon-scattering processes. This attenuation limits the Q of the BAW resonator. Analytical expressions for maximum Q limits for a variety of intrinsic scattering processes, such as anharmonic phonon-phonon loss and thermoelastic damping (TED), are well known and experimentally validated for commonly used acoustic materials [25-31]. An often neglected scattering process is the phonon-electron interaction [32-37], which is significant in materials that have both moderate-to-high doping concentrations and a mechanism facilitating strong electromechanical interactions. Piezoelectric

semiconductor materials such as ZnO, GaN and cadmium sulfide (CdS) fulfill both criteria and as we will show in this thesis, the phonon-electron scattering can be the dominant loss mechanism in such materials.

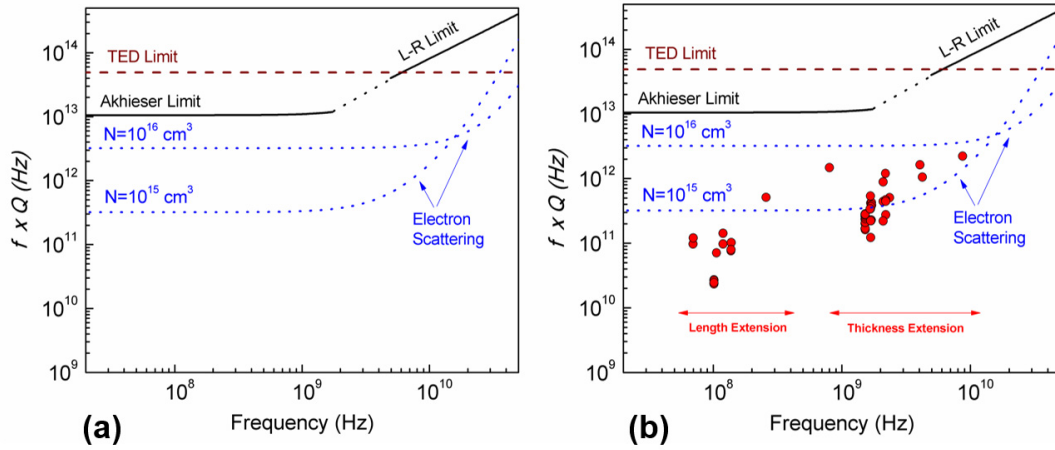


Fig. 1.7 : (a) Intrinsic material $f \times Q$ limits for GaN-based BAW resonators. For longitudinal acoustic wave resonators, the dominant loss mechanisms are phonon-phonon loss and phonon-electron loss. The electron loss is highly dependent on the free carrier concentration in the material. Based on analytical values, it is possible that the phonon-electron scattering is significant or even dominant for GaN (b) Measured $f \times Q$ values for GaN resonators (red dots) in comparison with the theoretical limits provide qualitative validation of this hypothesis.

A very popular figure of merit for describing intrinsic loss mechanisms across a wide range of frequencies is the limiting value of the frequency-quality factor product or $f \times Q$ ($f = \omega/2\pi$). The higher the $f \times Q$ value, the lower the loss. Fig. 1.7 demonstrates the theoretical values for the various loss mechanisms in GaN, and measured results across a wide range of frequencies. It can be seen that the measured values of $f \times Q$ are lower than that expected from the phonon-phonon loss, and that the phonon-electron loss is significant and potentially the dominant acoustic loss mechanism for GaN resonators.

1.8. Acoustoelectric Amplification in GaN BAW Resonators

Along with investigating the loss due to electron scattering, we show that phonon-electron interactions can lead to acoustic gain of standing waves in piezoelectric semiconductor BAW resonators and present, for the first time, a comprehensive model that explains the enhanced mechanical Q of these resonators under the acoustoelectric effect [38, 39].

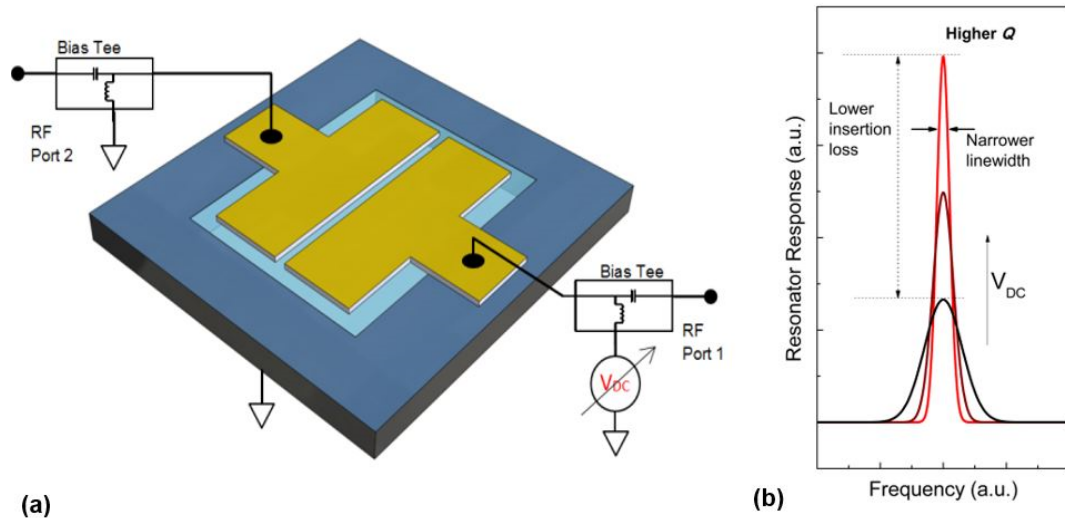


Fig. 1.8 : Schematic showing the simple experimental setup and the effect of acoustoelectric amplification on the performance of GaN resonators. (a) Acoustoelectric amplification in GaN resonators can be seen by applying a DC bias to the device during normal RF operation. (b) We see an improvement in Q and insertion loss (IL) and a narrowing of the bandwidth of the device. This is a dynamic improvement and can be switched on/off or tuned during operation. Measured results shown later exhibit up to 35% improvement in Q , with DC bias values as low as 20 V. This thesis proves that the measured performance improvement is due to the acoustic gain resulting from phonon-electron gain in piezoelectric semiconductor BAW resonators, and eliminates all other potential causes by careful experimental controls.

The measured data acquired on multiple BAW resonators with resonance frequencies ranging from 37 MHz to 8.7 GHz and fabricated using multiple wafers of single-crystal wurtzite GaN are consistent with theoretical trends. Measured results show up to a 35% increase in the Q of the resonator simply by applying a DC bias,

something that is unprecedented in piezoelectric materials. We explore the dependence of both gain and loss on factors such as charge carrier concentration, mobility, and resonance frequency. We show that it is possible to design piezoelectric semiconductor BAW resonators with (i) minimum phonon-electron scattering loss under normal operation, (ii) reduced total energy loss via acoustoelectric interaction, and (iii) acoustoelectric gain that can overcome all other losses, effectively creating a highly frequency-selective acoustoelectric resonant amplifier. We believe that this is a new area of research and deserves further analytical and experimental exploration.

1.9. Contributions

The important contributions of this thesis are as follows:

- Development of the first small-format resonant IR detector arrays using GaN as the structural layer. Measured results demonstrate high sensitivity and fast response time of less than 1 ms. Expected thermomechanical NETD values for various designs ranges from 10 mK to 100 mK.
- Development of a thin-film CNT nanocomposite with an absorbance of as high as 95% across a broad spectra. This is one of the highest performance IR absorbers with high absorption per unit thickness.
- Development of a plasmonic metamaterial structure that demonstrates narrowband IR absorption in the LWIR spectrum (1.5 μm passband centered on the 10 μm LWIR wavelength, with $> 45\%$ measured efficiency). These structures have been

integrated on an array of resonant IR detectors and the integrated detectors shows high selectivity to LWIR radiation.

- Characterization of GaN as an important material for use as a high-frequency electromechanical material.
- The first investigation of the phonon-electron interactions of GaN-based BAW resonators. This analysis is valid for all piezoelectric semiconductor materials and is thus an important result for the design of BAW resonators based on materials such as GaN, zinc oxide (ZnO), silicon carbide (SiC), gallium arsenide (GaAs), and CdS.
- First experimental demonstration of acoustoelectric amplification in piezoelectric semiconductor BAW resonators. We also develop the first theoretical model that explains this amplification, and corroborates to a large extent the measured data.

1.10. Organization of the Thesis

In Chapter 1, we discussed the overall scope of the thesis, and highlighted some of its key scientific contributions. In Chapter 2, we elaborate upon the design, fabrication, and characterization of resonant IR detectors, differential-sensing pairs and arrays. We explain the use of efficient broadband and narrowband absorbers for IR absorption and demonstrate measured results for the same. Chapter 3 deals with the basic characterization of GaN resonators necessary for high performance resonant devices. Chapter 4 details the phonon-electron interactions in piezoelectric semiconductor BAW resonators, from theory to measured results. We present the

concept of acoustoelectric amplification of standing waves, and present theory and corroborating experimental evidence. We conclude this thesis with some discussion of future research directions in Chapter 5.

Appendix A provides a full derivation of the phonon-electron loss coefficient in travelling waves, based on the work of A. R. Hutson and D.L. White [39-41], which is used as a basis for our work on understanding phonon-electron loss and acoustoelectric amplification in GaN and other piezoelectric semiconductor materials.

Chapter 2 Resonant IR Detectors and Arrays

This chapter deals with the use of arrays of high-performance micromechanical resonators as resonant IR detectors. Section 2.1 deals with the theoretical model and design principles behind low-noise resonant IR detectors. Sections 2.2-2.5 detail the fabrication and characterization of detectors and detector arrays made using GaN and other materials. Sections 2.6 and 2.7 provide details of two novel IR absorbers developed as part of this work, designed to provide broadband and spectrally-selective narrowband absorption respectively.

2.1. Theoretical Model and Resonator Design

The basic principle of transduction for a resonant IR detector is the change of its mechanical resonant frequency due to the temperature rise induced by the absorbed IR radiation. The mechanical resonator can be driven at its natural frequency in an open loop or used in a self-sustaining oscillator by using simple and common feedback circuits, allowing continuous operation with a very stable frequency. In this section, we focus on the design of the resonator as an IR sensing element. The resonant IR detector consists of a detector plate suspended by thin, high thermal resistivity tethers that thermally isolate the detector from the substrate (Fig. 2.1).

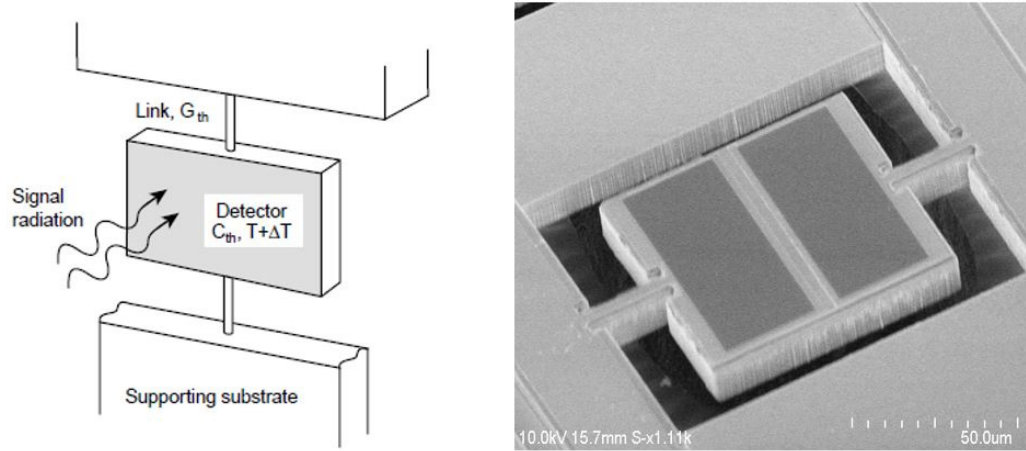


Fig. 2.1 : (a) General model of a thermal IR detector. Image from [1]. (b) Scanning electron micrograph image of a released two-port GaN resonator with dimensions of $80 \mu\text{m} \times 80 \mu\text{m} \times 12 \mu\text{m}$. The suspended membrane acts as the IR radiation collector, while thermally connected to the substrate (thermal sink) only by the mechanical tethers which have a low thermal conductance by virtue of their thin and long structure, and ideally the use of material that possess low thermal conductivity.

The resonator can be actuated in a number of ways such as capacitive, piezoelectric, thermal, and magnetic. We choose to use piezoelectric actuation as it is the best suited method to achieve high performance with low driving power and with a small resonator size. Different modes of resonance of the plate can be used for temperature sensing; here, we focus on the length-extensional resonant mode. The resonance frequency is a function of temperature and is given by Eqn. 2.1.

$$f(T) = \frac{1}{2L(T)} \sqrt{\frac{C_{eff}(T)}{\rho}} \quad \text{Eqn. 2.1}$$

Here L , C_{eff} , and ρ are the length, effective stiffness, and mass density, respectively. The detector surface that is to be exposed to radiation can be coated with a material that is an efficient thermal absorber of IR radiation. This decouples the

function of efficient thermal absorption from efficient resonator performance. This is critical since most resonator designs and materials are poor absorbers of infrared radiation. Commonly used absorber materials such as silicon nitride, gold black, experimental new materials such as nanocomposites, or designed plasmonic metamaterials can be used as IR absorbers [42-47]. A detailed discussion of the IR absorbers is provided in Section 2.6 and Section 2.7. The conversion of incident IR radiation power $\phi(\lambda)$ into temperature change is given by:

$$\Delta T = \frac{\eta(\lambda)\phi(\lambda)}{\sqrt{G_{th}^2 + \omega_{ir}^2 C_{th}^2}}, \quad \text{Eqn. 2.2}$$

where

G_{th} is the effective thermal conductance of the device,

C_{th} is the thermal capacity of the device,

ω_{ir} is the rate of change of the incident signal,

λ is the spectral wavelength of radiation, and

$\eta(\lambda)$ is the absorption efficiency of the IR absorber layer.

The relation between the increased temperature and the change in frequency of the resonator is determined by the thermal dependencies of the resonant frequency.

2.1.1.1. Thermal Dependencies of Resonator Frequency

The relative change in resonator frequency with respect to temperature is given by:

$$\alpha_T = \frac{1}{f(T)} \frac{\partial f}{\partial T} \quad \text{Eqn. 2.3}$$

This quantity is commonly known as the TCF and is expressed in parts per million per K (ppm/K). From Eqn. 2.1 and Eqn. 2.3, we can see that the significant temperature dependent properties are the length and the stiffness. The changes in the length and the effective stiffness with respect to temperature are given by:

$$L(T) = L(T_0)[1 + (\mathbf{LTE})(T - T_0)] \quad \text{Eqn. 2.4}$$

$$C_{eff}(T) = C_{eff}(T_0)[1 + (\mathbf{TCE})(T - T_0)], \quad \text{Eqn. 2.5}$$

where **LTE** and **TCE** are the coefficient of linear thermal expansion and thermal coefficient of elasticity, respectively. For most materials relevant in this context, the TCE is the dominant factor in setting the TCF and puts an upper bound on the thermal sensitivity of the resonator. Using Eqn. 2.3-Eqn. 2.5, for most materials, we get

$$TCF \cong \frac{\mathbf{TCE}}{2} \quad \text{Eqn. 2.6}$$

The choice of GaN as the resonant material is deliberately made with a view to boosting this TCF limited sensitivity by using some unique properties of GaN. GaN is known to be a pyroelectric material, with a theoretical pyroelectric voltage coefficient (P_v) of 7×10^5 V/m-K, and measured P_v as high as 1×10^4 V/m-K [48, 49].

$$V_{pyro} = P_v t \Delta T \quad \text{Eqn. 2.7}$$

This implies that the additional temperature ΔT due to IR radiation would induce a pyroelectric voltage V_{pyro} across the thickness t of the GaN film. It is theorized that this instantaneous voltage would generate a large strain across the film (in addition to the strain wave due to actuation RF voltage) due to a combination of linear piezoelectric and second-order electrostrictive effects, thus changing the frequency of the resonator drastically upon IR irradiation.

In GaN, it has been found that a significant quadratic (electrostrictive) dependence of strain on electric field exists [50]. Electrostriction can be described as the quadratic dependence of strain on the applied electric field, and is most simply included in the piezoelectric constitutive equations as $S_{ij} = sT + d_{ij}E + M_{ij}E^2$ where M_{ij} is the electrostrictive coefficient. If we include electrostrictive effects as per the analysis of Willatzen and Lew Yan Voon [51-55], we see that the temperature-dependent frequency equation changes to:

$$f(T) = \frac{n}{2L(T)} \sqrt{\frac{\epsilon'_{31}c_{11} + e_{31}e'_{31}}{\rho(\epsilon'_{31} + 2M_{31}E_{pyro}(T)e'_{31})}} \quad \text{Eqn. 2.8}$$

where $\epsilon'_{31} = (\epsilon_{31} - M_{31}E_{pyro}e_{31})$, $e'_{31} = (e_{31} + M_{31}E_{pyro}c_{31})$, and the coefficients ϵ, e , and their corresponding primed counterparts represent permittivity and piezoelectric strain tensors, respectively. M_{31} is the electrostrictive transverse coefficient and E_{pyro} is the electric field across the thickness of the film, caused by pyroelectric charge separation. Based on published values for the material properties of GaN and an assumed M_{31} value of $-6 \times 10^{-19} \text{ m}^2 \text{ V}^{-2}$, we get the relative frequency

sensitivity to temperature as large as -2000 ppm/K (Fig. 2.2). This is almost 100× the sensitivity of a TCF-limited material.

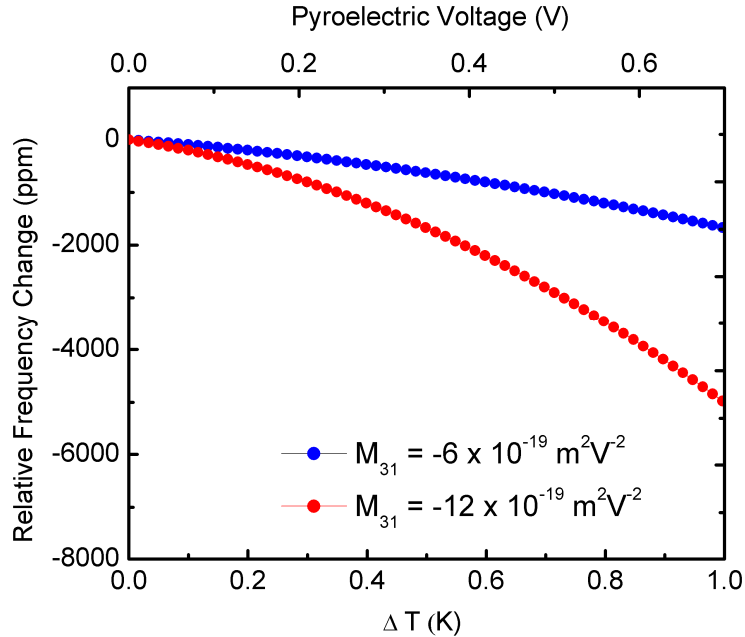


Fig. 2.2 : Predicted values of resonant frequency change due to electrostriction in GaN. This calculation assumes a 2.15 μm thick film and a pyroelectric coefficient of value $1 \times 10^5 \text{ V/m}\cdot\text{K}$. The accurate value of M_{31} is not known and an approximate, conservative value is used. This plot is derived based on the theoretical model for electrostriction in GaN [55].

A caveat to this analysis is that there is some debate about the actual values of M_{ij} for GaN, with theoretical estimates for M_{33} being on the order of $(1-10) \times 10^{-22} \text{ m}^2\text{V}^{-2}$ [24] and experimental results in the order of $1.2 \times 10^{-18} \text{ m}^2\text{V}^{-2}$ [25]. Therefore, we consider a range for M_{33} of GaN for estimating the elastic constants. In our model, we also use a value of $M_{31} = -6 \times 10^{-19} \text{ m}^2/\text{V}^2$ (half of M_{33} in magnitude). The sign of M_{31} is negative (opposite of M_{33}) to account for the fact that as the material expands due to M_{33} , it will contract in the M_{31} direction to conserve mass. (Fig. 2.2). Extracting theoretically and empirically consistent values for M_{ij} would require some fundamental experiments on GaN single crystal films in the future. Nevertheless, the

pyroelectric-electrostrictive interaction of GaN can be utilized to improve the sensitivity of the detection mechanism for resonant IR detectors. This effect, however, requires a shutter as it is sensitive to the rapid change in the temperature and not the absolute temperature of the resonator.

2.1.2. Design for Low NETD

The important metrics for comparison of thermal detectors are the response time, the detectivity (D_{th}^*) the thermal fluctuation noise floor (ΔT_{min}) (the dominant noise mechanism for mechanical resonators [10]), and the thermal NETD [1, 2, 10, 15]. The important IR detector metrics are given by the following equations:

$$D_{th}^* = \left(\frac{\eta^2 \beta A}{4k_B T_D^2 G_{th}} \right)^{1/2}, \quad \text{Eqn. 2.9}$$

$$\Delta T_{min} = \sqrt{\frac{k_B T^2}{c_{th}}}, \quad \text{Eqn. 2.10}$$

$$NETD = \frac{(4F^2 + 1)\sigma_N}{\tau_{opt}\beta A \mathfrak{R}} \left[\left(\frac{\Delta P}{\Delta T} \right)_{\lambda_1 - \lambda_2} \right]^{-1}, \quad \text{Eqn. 2.11}$$

where

F is the focal ratio of the focusing optics,

τ_{opt} is the transmissivity of the focusing optics,

β is the pixel fill factor

A is the area of the resonator,

σ_N is the frequency instability, and

α_T is the relative change in frequency with per unit change in temperature.

$\left(\frac{\Delta P}{\Delta T}\right)_{\lambda_1-\lambda_2}$ is the temperature dependence of the blackbody power emission function for the spectral band $\lambda_1 - \lambda_2$. For the 8-14 μm LWIR range, this value is 2.62×10^{-4} W/cm²K [2, 15]. \mathfrak{R} is the responsivity in terms of incident power radiated by a blackbody source, and is expressed as [15]:

$$\mathfrak{R}(\omega_{ir}) = \frac{\eta\alpha_T}{G_{th}\sqrt{(1+\omega_{ir}^2\tau^2)}}, \quad \text{Eqn. 2.12}$$

where

$$\tau = C_{th} G_{th}^{-1}. \quad \text{Eqn. 2.13}$$

The NETD can further be decomposed into spatial and temporal components [56]. The spatial NETD depends on the spatial variation of the IR response of large arrays of IR detectors and is not discussed here. The temporal thermal NETD can be calculated for every pixel, and is the focus of this work. State-of-the-art uncooled detectors demonstrate measured temporal NETD values between 30 mK to 50 mK [57]. As expected, there will need to be a tradeoff between responsivity and frequency instability. We can combine Eq. (10) and Eq. (11) to expand the relation for NETD in terms of all the operating parameters as follows

$$NETD = \frac{(4F^2 + 1)\sigma_N G_{th}\sqrt{(1 + \omega_{ir}^2\tau^2)}}{\tau_{opt}\beta A\eta(\alpha_T)} \left[\left(\frac{\Delta P}{\Delta T}\right)_{\lambda_1-\lambda_2} \right]^{-1}. \quad \text{Eqn. 2.14}$$

The critical design parameters here are the thermal conductance, resonator surface area, and α_T . We can make some design assumptions in order to set achievable goals for low thermal NETD values. For example, efficient absorbing materials can give us up to 90% or higher absorption over the desired spectral range [43-47, 58]. Of the

noise processes that could affect the micromechanical resonator frequency significantly, the dominant source is the temperature fluctuation induced frequency instability [15, 59]. For room temperature conditions, and assuming conservative values of resonator Q and input power levels, the limiting value for total short-term frequency noise can be estimated to be on the order of 10^{-11} [59, 60]. Practical MEMS oscillators have been able to achieve measured short-term frequency stabilities between 5×10^{-9} [61] and 6×10^{-10} [62] with larger resonators. The design optimization challenge will be to reach these values while maintaining the small footprint and thermal mass required for IR detectors. As seen in our measured results [63] and prior literature [59, 60], frequency instability scales inversely with the loaded Q . Values for Q on the order of $10^3 - 10^4$ in the frequency range of 1 MHz – 1 GHz using thin-film piezoelectric materials have been measured practically in prior literature and in the course of this work [31, 64-66]. Based on this we assume a frequency instability of $\sigma_N = 10^{-10}$. Higher Q values will only improve the noise performance and also improve the sensing resolution as the minimum detectable frequency shift for mechanical resonators scales inversely with \sqrt{Q} [67].

We can reorder Eqn. 2.14 in order to isolate the important parameters that can be optimized during design in order to achieve the lowest NETD performance.

$$NETD = \left\{ \frac{(4F^2 + 1)\sigma_N \sqrt{(1 + \omega_{ir}^2 \tau^2)}}{\tau_{opt} \beta(\alpha_T)} \left[\left(\frac{\Delta P}{\Delta T} \right)_{\lambda_1 - \lambda_2} \right]^{-1} \right\} \times \left[\frac{G_{th}}{\eta A} \right] \quad \text{Eqn. 2.15}$$

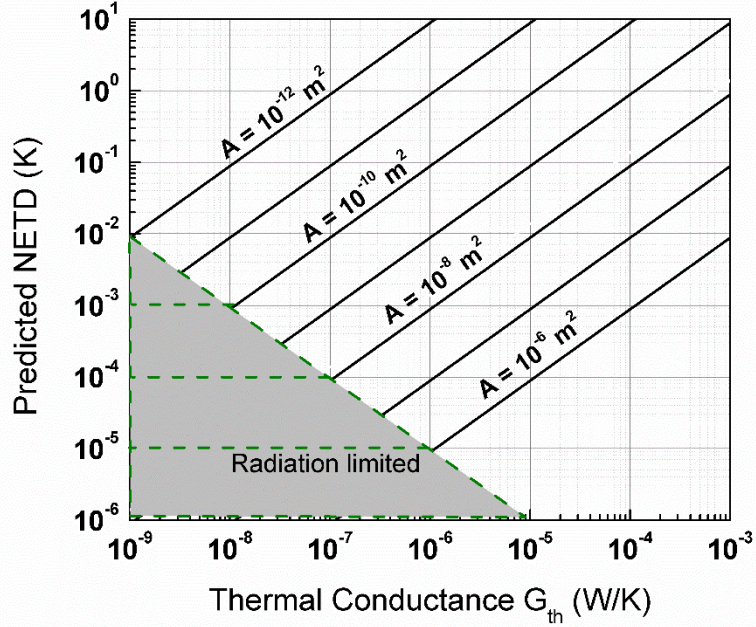


Fig. 2.3: The modeled NETD design space as a function of the GaN resonator area and the total thermal conductance between the GaN resonator and its surroundings. This particular graph assumes ideal absorption. The radiation limit denotes the point at which radiation losses dominate the heat loss. When not limited by radiation, the tether conductance and detector area are the two most important design parameters for determining the NETD. This graph assumes $f/1$ optics with 80% transmissivity, a pixel fill factor β of 80% and ideal IR absorption η . Frequency instability is assumed to be 10^{-10} .

In order to reduce NETD, it is necessary to reduce G_{th} , improve absorption η , and increase detector area. Clearly the latter requirement is at odds with the practical requirements of high spatial resolution: large arrays of small and tightly packed detectors. Thus, we try to optimize Eqn. 2.15 by reducing G_{th} and improving η , while trying to maintain a small pixel footprint (Fig. 2.3). Optimizing $\left[\frac{G_{th}}{\eta A}\right]$ is achieved by proper thermal design of the resonator element, and high efficiency absorbers, and is the focus of the succeeding sections.

2.1.3. Thermal Design of the Resonator Element

Important thermal parameters to consider while designing the resonator ‘pixel’ are the thermal conductance of the system and the thermal capacity of the body of the resonator given by

$$G_{th} = G_{tethers} + G_{air} + G_{rad} \quad \text{Eqn. 2.16}$$

and

$$C_{th} = \sum_i (\rho)_i (C_p)_i V_i \quad \text{Eqn. 2.17}$$

For a resonator made of multiple materials, including the piezoelectric film, the absorber, and metal electrodes, thermal conductance through the tethers is given by:

$$G_{tethers} = n \sum_i \frac{\kappa_i (A_t)_i}{(L_t)_i} \quad \text{Eqn. 2.18}$$

for every i^{th} material in the composite stack. The quantities κ , ρ , C_p , A_t , L_t , and V denote the thermal conductivity, mass density, specific thermal capacity, area of cross-section of the tethers, length of tethers, and the volume of the resonator body. Note that the conductance depends on the number of tethers ‘ n ’ that connect the resonator to the substrate. For a complete understanding of the limits of performance, we need to consider other relevant modes of heat loss from the resonator to its surroundings. The conductance through air and via radiation exchange (from both surfaces of the detector) is given by Eqn. 2.19 and Eqn. 2.20, respectively [68].

$$G_{air} = \frac{\kappa_{air}A}{d_{cavity}}, \quad \text{Eqn. 2.19}$$

$$G_{rad} = 4(\varepsilon_{top} + \varepsilon_{bot})A\sigma_b T^3 \approx 8\varepsilon_D A\sigma_b T^3, \quad \text{Eqn. 2.20}$$

where

κ_{air} and d_{cavity} are the thermal conductivity and height of the air column,
 A is the surface area of the detector,
 ε_{top} and ε_{bot} are the emissivity values of the top and bottom surfaces of the detector,
 σ_b is the Stefan-Boltzmann constant, and
 T is the absolute temperature of the detector.

The conduction model through air is valid down to pressures of about 20 μTorr . Estimated worst case scenario values for G_{air} and G_{rad} are generally smaller than the values of G_{tether} for the designs presented here (Fig. 2.3). The worst case scenario assumes the emissivity of the detector surfaces to be $\varepsilon_D = 1$, and κ_{air} of 0.026 W/m-K [68, 69].

State-of-the-art bolometers have values of G_{th} on the order of 10^{-8} W/K, before being limited by radiation effects [70]. Such values of thermal conductance are possible for resonators with thin films, and the goal is to achieve these values with resonant detectors as well.

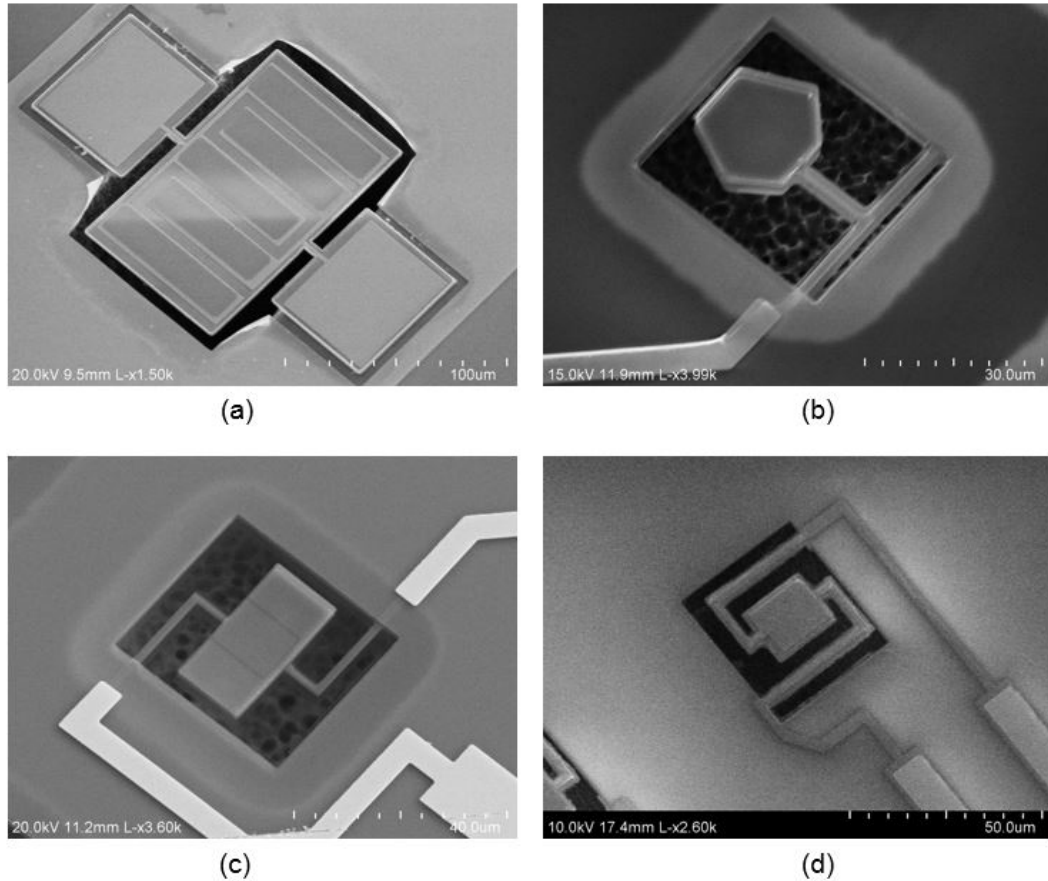


Fig. 2.4 : Examples of fabricated resonators show the evolution of the tether design for high thermal isolation, while retaining the total area occupied by the resonator ‘pixel’. This is generally achieved by using bent or meandered tethers that increase effective length. The SEM images show (a) a prototype with simple, short tethers, (b) a tether-suspended thickness mode FBAR, (c) a resonator with single-bend crableg tethers, and (d) a resonator with a two-bend crableg tether. Fabrication and characterization of these resonators are presented in subsequent sections of this chapter.

Other feasible ways to decrease G_{th} is to use single tether designs or meandered tethers, while taking care to maintain good mechanical performance of the resonator. In some of the more recent designs in this work, longer tether designs have been implemented using ‘crableg’ designs (Fig. 2.4) that allow a much longer effective tether length, with negligible increase in the total pixel area. It is important while designing such non-conventional tether structures to ensure that the Q of the resonator does not degrade significantly due to anchor loss.

2.2. Prototype Detectors and Sense-Reference Pairs

2.2.1. Fabrication Process

Complete details about the GaN films are provided in Chapter 3. The fabrication process used for the resonant detectors relies on conventional MEMS processing (Fig. 2.5). Four-inch GaN-on-Si wafers, acquired from vendors, are used as the starting substrates. First, thick silicon dioxide (SiO_2) layer is deposited on the backside of the wafer. The contours of the GaN resonator were defined using conventional lithography and plasma etched using Cl_2/BCl_3 chemistry. Top electrodes of 10 nm Ti and 100 nm of Au were deposited and patterned using lift-off. A 400 nm thick gold layer was deposited on the signal and ground pads to reduce the probe contact resistance. A 50 nm thin layer of PECVD silicon nitride was deposited as the absorber layer and patterned. The reference resonators did not have the silicon nitride layer. Devices were released using selective DRIE etching of silicon from the backside having SiO_2 as the mask and the AlN/AlGaN buffer layer as the etch stop. Finally, the bottom electrode (10 nm Ti/100 nm Au) was sputter deposited from the backside. This process flow is used for most of the GaN devices in this work, unless otherwise noted.

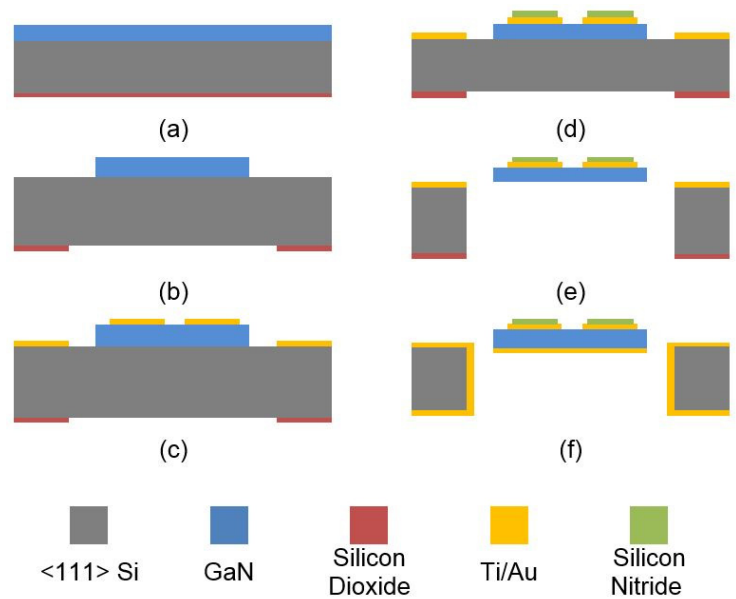


Fig. 2.5 : Fabrication process flow for GaN resonator prototypes. The GaN films are lithographically patterned to define the resonator. Top electrodes are defined by e-beam evaporation and liftoff. After the IR absorber layer is patterned, the resonator is released using through-wafer DRIE. Sputtered metal is used for the back electrode.

2.2.2. Prototype Measured Results

Single element sense and reference prototype resonant detectors using thin film GaN are fabricated and characterized. The experimental setup for measuring the frequency response of the GaN resonators is shown in Fig. 2.6. The RF performance of the GaN resonators is measured using an Agilent Vector Network Analyzer. IR illumination is provided by a Tungsten-Halogen lamp (Ocean Optics Inc.), and is coupled into the probe station using optical fibers. The near-IR power density per unit detector area is calibrated using a Thorlabs FDS 100 photodiode and is measured to be $16 \text{ nW}/\mu\text{m}^2$. Considering the total area of this particular resonator, the incident power is $156 \mu\text{W}$. The calculated incident power is $284 \mu\text{W}$ (ideal power is calculated from lamp and fiber optic cable datasheets, and does not include spreading losses and attenuation in air).

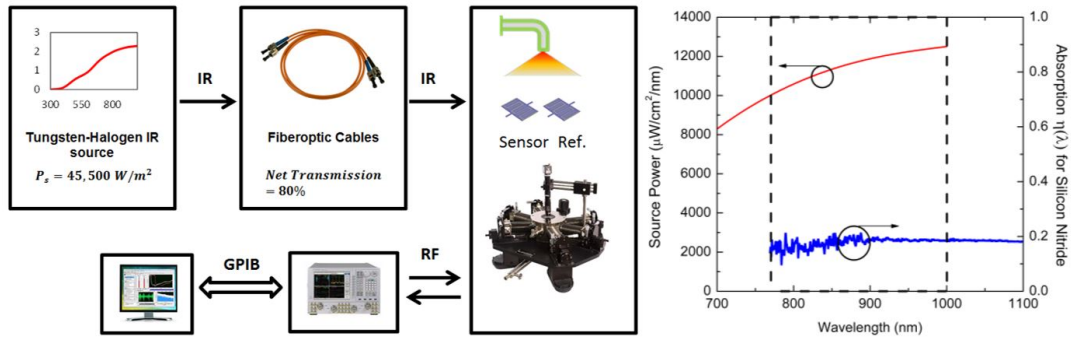


Fig. 2.6 : (a) Schematic showing the IR measurement setup of the GaN resonant sensors. Both sensor and reference resonators are measured using an identical procedure. (b) The radiant power output of the source/optical fiber system as per vendor specifications [69], and the absorption efficiency of the silicon nitride layer, measured using NIR spectroscopy. The boxed area is the spectral region that describes the NIR radiation absorbed by the sense resonators.

Fig. 2.7 shows an SEM image of the prototype sensor, and demonstrates the change in the frequency response of a representative sense resonator upon IR radiation. The shift in the frequency is clearly visible, as is the shift in the insertion loss. In fact, four important parameters of the resonator (frequency, Q , IL, and bandwidth) change simultaneously [71] and can be used as the metric of choice for alternate sensing schemes.

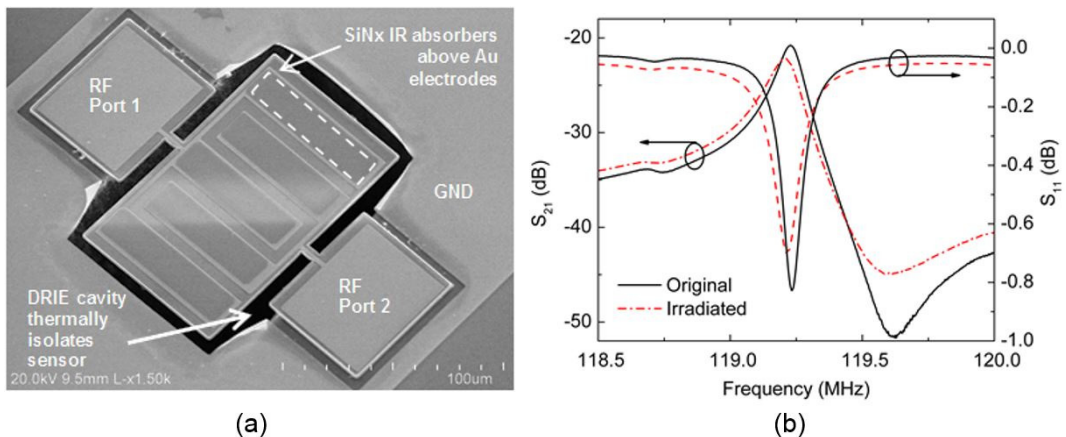


Fig. 2.7 : (a) An SEM image of a fabricated GaN resonator with silicon nitride absorber. The dimensions of the device are $120 \mu\text{m} \times 80 \mu\text{m} \times 2.15 \mu\text{m}$. (b) A comparison of the nominal and irradiated RF (transmission and reflection) performance of the resonator with $156 \mu\text{W}$ of incident power ($\sim 30 \mu\text{W}$ of absorbed power). All the relevant operating parameters (frequency, Q , IL, and bandwidth) of the resonator change simultaneously.

2.2.3. Differential Sensing

The IR sensors must be designed to work reliably at conditions that are sub-optimal for performance, in the presence of interfering signals due to shock, acceleration, rotation, and changes in ambient temperature. The best way to cancel out these interfering effects is to use a reference resonator that is similar to the sensor in all ways except one: the surface of the reference resonator does not have the absorber layer exposed. Ideally the reference resonator shall reflect all incident IR energy and remain invariant to radiative heating, while tracking the sense resonator when subject to the other interfering signals mentioned above. The small density difference caused by the absorber and the expected variations in fabrication offset the frequency of the reference by a small amount, as compared to the sensor. This difference is enough to cause a small beat frequency if the frequency outputs of the sense and reference resonators are mixed together. In order to reduce this beat frequency, further design iterations of the reference can have the absorber layer, but coated with half the thickness of the top electrode (other half is under the absorber layer). The frequencies of the two resonators can be described as functions of temperature by [72]:

$$f_s(T_s) = f_s(T_0) + a_s\Delta T_s + b_s\Delta T_s^2 + \dots \quad \text{Eqn. 2.21}$$

$$f_r(T_r) = f_r(T_0) + a_r\Delta T_r + b_r\Delta T_r^2 + \dots \quad \text{Eqn. 2.22}$$

Neglecting higher order expansion terms, we can write the beat frequency as

$$f_B(T) = f_s(T_s) - f_r(T_r) = [a_s\Delta T_s - a_r\Delta T_r] + f_B(T_0) \quad \text{Eqn. 2.23}$$

The subscripts s , r , and B indicate the sensor, reference, and beat frequencies, respectively. T_0 is the initial temperature. The coefficients a_i are the net coefficients of frequency change with respect to temperature, inclusive of all contributing mechanisms. Thus, the relative change in the beat frequency is a function of the incident IR radiation (Eq. 8). The beat frequency and the change thereof are easily measured using a mixer and frequency counter [72], and determines the responsivity of the differential measurement system:

$$\mathfrak{R}_{diff} = \frac{\Delta f_B / f_B(T_0)}{\phi(\lambda)} \quad \text{Eqn. 2.24}$$

Using Eqn. 2.21, Eqn. 2.24, and Eqn. 2.2 for slowly varying IR signals of a small magnitude, we get the differential responsivity to be:

$$\mathfrak{R}_{diff} = \frac{[a_s\Delta T_s - a_r\Delta T_r] / f_B(T_0)}{\phi(\lambda)} \approx \frac{a_{diff}\eta(\lambda)}{G_{th}f_B(T_0)} \quad \text{Eqn. 2.25}$$

Thus, for a given design, along with the thermal conductance and the absorber efficiency constant, the responsivity depends on a_{diff} , the net coefficient of frequency change for the resonator, inclusive of all mechanisms. Since the reference is almost invariant, a_{diff} is nearly equal to a_T for the sense resonator. Differential sensing can boost the system sensitivity, since the original beat frequency can be made extremely small, limited only by fabrication tolerances. Differential sensing also eliminates common-mode effects such as slow changes in ambient operating

temperature, pressure variations in the sensor package, and acceleration. Crucially, differential measurements using beat frequency detection for TCF-based sensing eliminates the need for a mechanical chopper, leading to savings in size, weight, and power.

The responses of the sense resonator and a reference resonator (identical to the sensor except the absence of the silicon nitride absorber) are measured as the IR signal is turned ON and OFF as shown in Fig. 2.8(a). Note that the frequency axis (Y-axis) on both graphs has the same span, visibly demonstrating the difference in response between the two devices. In comparison to the frequency shift of the sensor, the reference frequency is almost invariant. The beat frequency obtained from these two resonators is shown in Fig. 2.8(b). It is clear that the IR illumination causes ~30 kHz change in the sense resonator, which when compared to its original frequency of 119 MHz is small (252 ppm). The original beat frequency is ~205 kHz, and compared to this, the change in the beat frequency is again ~30 kHz, which is a 15% shift. Thus, the differential measurement can provide higher sensitivity to small changes in IR illumination.

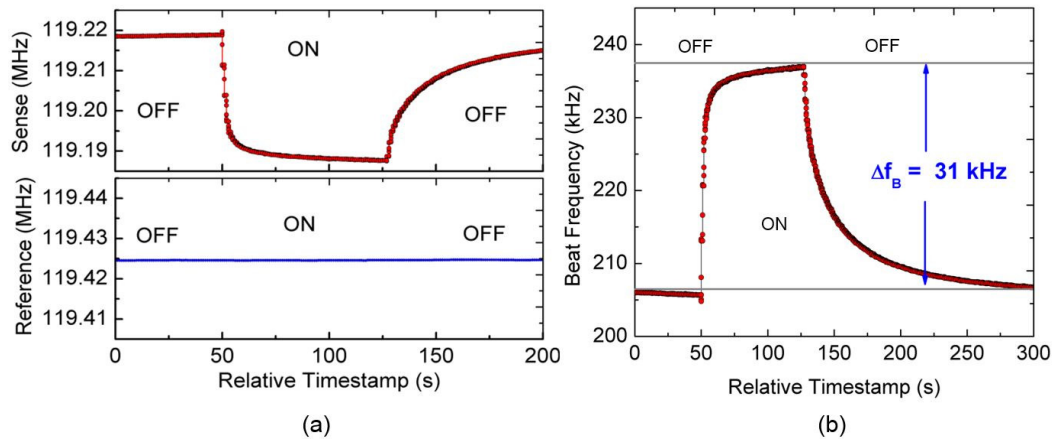
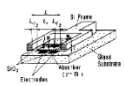
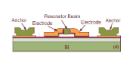
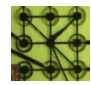

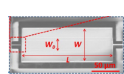




Fig. 2.8 : (a) Measured data for the sense and reference resonator pair, showing the response upon IR illumination with $156 \mu\text{W}$ of radiated IR power ($\sim 30 \mu\text{W}$ of absorbed power). Note that the span of the Y axis is the same for both graphs, and thus in comparison to the sense resonator, the reference resonator is almost invariant upon IR irradiation. (b) The beat frequency change upon IR irradiation. Relative change in the beat frequency when the IR signal of $156 \mu\text{W}$ is turned ON is about 15%. This is much larger than the relative change of the sense resonator alone. Using this differential measurement also eliminates common mode signals such as ambient temperature changes, acceleration sensitivity, and pressure sensitivity.

Table 2.I compares the performance of the single resonator and the sense-reference pair with the highest-performance resonant thermal detectors reported in the literature. It can be seen that the GaN resonators and sense-reference pairs can achieve high performance even with a small footprint. In comparison with the quartz devices, the GaN resonators are monolithically fabricated.

Table 2.I
A Comparison of Resonant IR Detectors in Literature

Material	Absorber	Dimensions	Absolute Responsivity (incident power)	Absolute Responsivity (absorbed power)	Ref.	
SiO ₂	p++ Si	1800 × 200 × 2 μm ³	-	450 ppm/μW	[73]	
Si	--	40 × 2.5 × 3 μm ³	347 ppm/K *	-	[74]	
Quartz	--	1000 μm dia., 18 μm thick	0.166 ppm/μW		[13]	
AlN	--	45 × 80 × 0.5 μm ³	-	0.3 ppm/μW ‡	[75]	
AlN	-	75 × 25 × 0.5 μm ³	N/A		[76]	
GaN (single resonator)	SiN _x	120 × 80 × 2 μm ³	1.6 ppm/μW	8 ppm/μW	THIS WORK	
GaN (differential pair)	SiN _x	120 × 80 × 2 μm ³	962 ppm/μW	4700 ppm/μW	THIS WORK	

* This is a temperature sensor. Radiant responsivity not given

‡ Temperature data is used to estimate radiant responsivity with appropriate assumptions.

2.3. Resonant IR Detector Arrays

After the successful demonstration of standalone prototypes and sense-reference pairs, the next step was to design and test arrays of such devices. Initial attempts using GaN films were unsuccessful, as most of the resonators broke during the release

process. The probable cause was the film stress in the thin ($\sim 1.3 \mu\text{m}$) GaN film that caused the entire array to break upon release, either using DRIE or isotropic gas phase SF_6 or XeF_2 etching. An alternate fabrication scheme was implemented utilizing a GaN-on-SOI substrate. The device layer of the SOI wafer is (111) Si, and is $10 \mu\text{m}$ thick. The device layer is etched from the front similar to the contours of the GaN device, forming a resonant structure that is a GaN-on-Si stack. The device layer provides mechanical stiffness to the resonators and improves release yield to almost 100 %. This approach has the added advantage of not requiring a sputtered Ti/Au back plane electrode as the Si device layer has a low resistivity ($0.001\text{-}0.01 \Omega\cdot\text{cm}$). Another advantage of growing GaN on an SOI wafer rather than on bulk Si is the lower built-in stress in the GaN film when grown on a thinner Si device layer which in turn results in a better quality thin film and fewer dislocations [77].

Two array formats, 2×2 and 4×4 , were designed and successfully fabricated using a GaN-on-SOI wafer as shown in Fig. 2.9. In order to accommodate the higher number of electrical traces for the 4×4 arrays, a two layer routing scheme was used, with a 500 nm thick SiO_2 spacer to provide isolation. Care was taken to minimize capacitive feedthrough between two ports of each resonator. These are, to the best of our knowledge, the first monolithically fabricated resonant IR sensor arrays.

The designs so far have more than one reference resonator in the larger array to provide redundancy. With the GaN-on-SOI process, yield was almost 100%; therefore, this redundancy eventually proved unnecessary. In future designs, we can decrease the number of references per array to improve the density and reduce the

dead area. As this design and fabrication matures, the bilayer routing shall be replaced by flip-chip bonding to a readout IC in order to optimize the pixel placement, spacing and the routing itself. A readout IC also has the advantage of allowing direct circuit integration, switching and signal processing. This is one part of the ongoing and future work for the project.

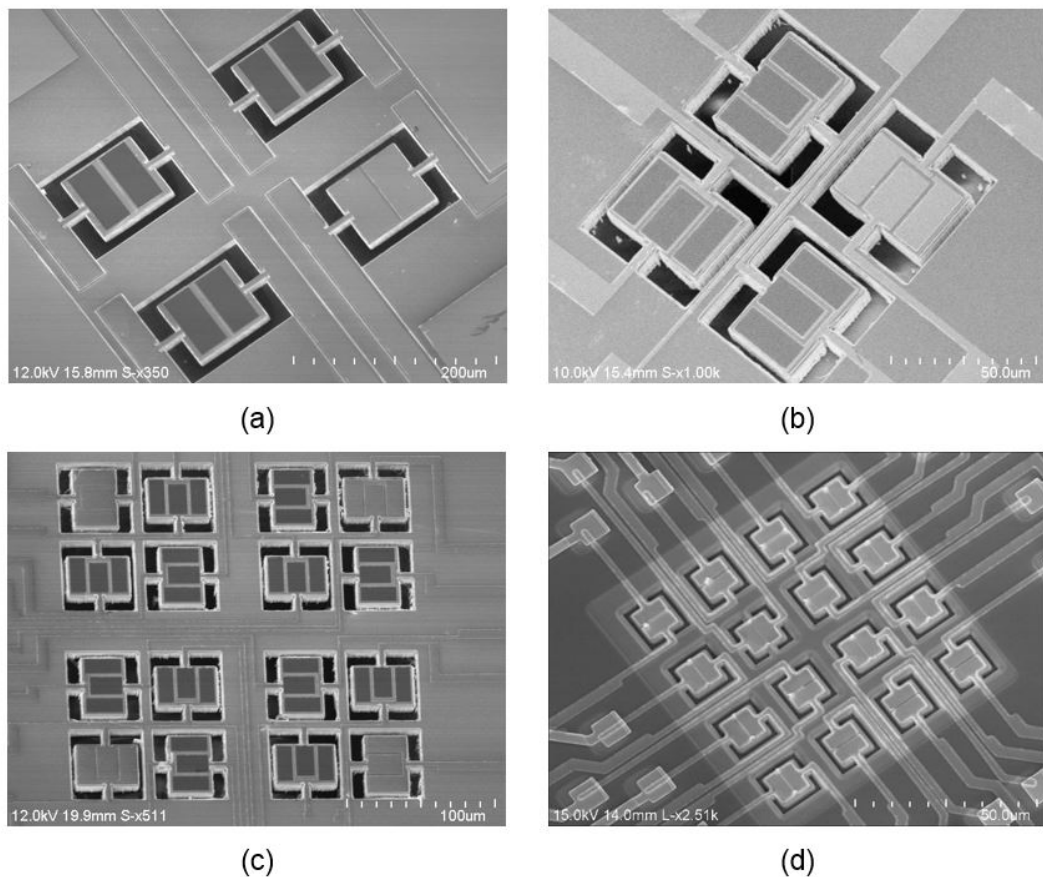


Fig. 2.9 : SEM images of successfully fabricated 2×2 arrays ((a) and (b)) and 4×4 arrays ((c) and (d)) with local reference resonators.

2.3.1. Measured Results of Small Formal Arrays

An important and desirable attribute of the IR detector array is that the nominal response and the illuminated response of each element of the array should be near-identical. Apart from reducing spatial variation in the array, it also facilitates the use

of similar electronic interface circuitry and reduces the calibration costs. For large format arrays, where the outputs of the sense resonators will be sequentially sampled by the same circuit, this is a critical requirement.

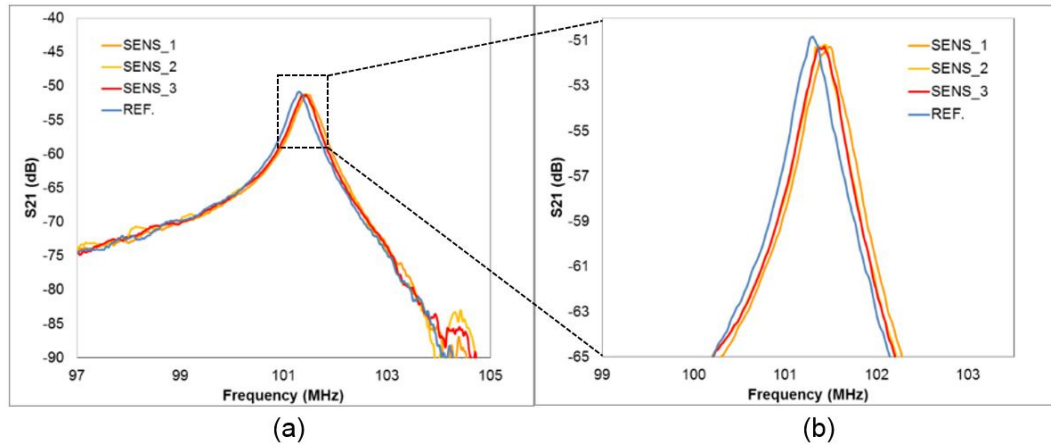


Fig. 2.10 : (a) Measured response of all the first length extensional mode resonance for the $80 \mu\text{m} \times 80 \mu\text{m}$ resonator array shown in Fig. 2.11. (b) Magnified range shows that the reference resonator has a slightly different frequency and IL than the sense resonators. This is expected due to the mass loading and stress caused by the silicon nitride absorber layer. The sense resonators themselves have near-identical performance, with a standard deviation of 0.0037% (37 ppm) with respect to the average.

Fig. 2.10 shows the measured RF response of a 2×2 array of resonators. Three of these devices are sensors coated with 200 nm SiNx absorber layers, and the sole uncoated device, clearly seen in the SEM image, is the local reference resonator. It can be seen that the nominal variation is very small (37 ppm for the sense resonators) in the array. The reference resonator has a slightly different response due to the differences in mass loading and stress caused by the absence of the silicon nitride absorber. The array in question is shown in Fig. 2.11 (a).

The relative change in beat frequency is mapped for the 2×2 array in Fig. 2.11. The reference resonator serves as the baseline. Based on the radiation incident on the detector surface (calibrated using the FDS 100 photodiode), and taking into account

the measured NIR absorption characteristics of the silicon nitride absorber we can calculate the temperature rise of ~ 70 mK (100 mK based on TCF data for the same devices) [63], or a frequency shift of ~ 36 ppm/K. This is significantly smaller ($60\times$ smaller) than the frequency shift seen in the prototype GaN-only sensor. It is expected that with the GaN-on-Si implementation, the thermal dependencies of the resonator are dominated by the TCF of the thick silicon (about -30 ppm/K). This supports our initial reasoning behind using GaN resonators for achieving higher IR sensitivity.

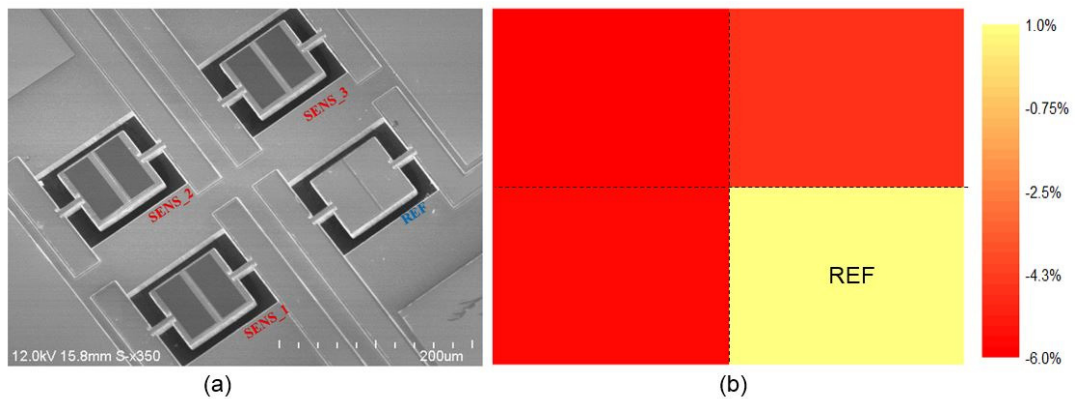


Fig. 2.11 : (a) 2×2 resonator array. Each resonator has dimensions of $80 \mu\text{m} \times 80 \mu\text{m}$. Three sense resonators are coated with 200 nm thick SiNx absorber layers. The reference resonator is uncoated. (b) Color map indicating the relative change in beat frequency for the 2×2 resonator array. The reference resonator is the baseline, while the three sense resonators show as much as a -5.5% shift in the relative beat frequency upon illumination with $102 \mu\text{W}$ incident IR power ($\sim 20.4 \mu\text{W}$ absorbed power).

A similar measurement and characterization scheme is followed for a larger format 4×4 array (Fig. 2.12(a)). In this design, there are 4 references and 12 sense resonators. The beat frequency is measured between a sense resonator and the nearest reference, providing spatially local compensation. The best sensitivity for this array was obtained from the change in the thickness mode at 1.68 GHz. The relative change in the beat frequency is mapped for the 4×4 array (Fig. 2.12 (b)).

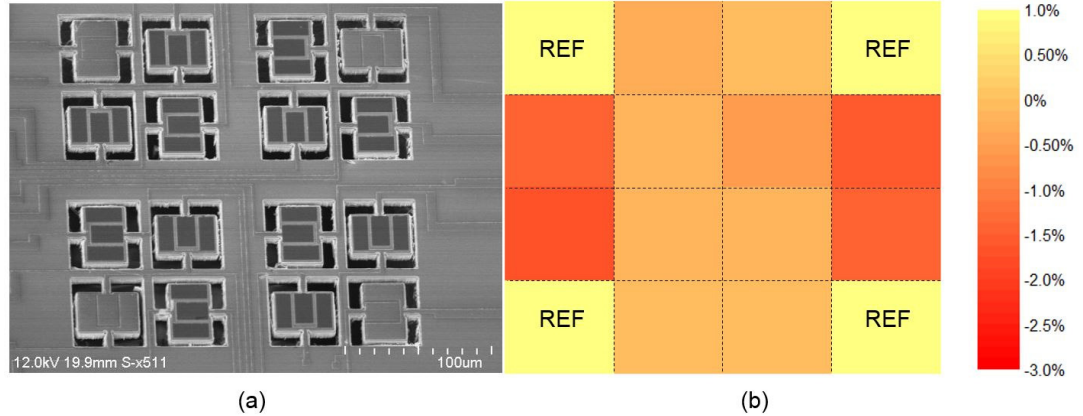


Fig. 2.12 : (a) SEM image of a fabricated 4×4 resonator array. Each resonator has dimensions of $28 \mu\text{m} \times 38 \mu\text{m}$. Twelve sense resonators are coated with 200 nm thick SiNx absorber layers. The four reference resonators (at the corners of the array) are uncoated. (b) Color map indicating the relative change in beat frequency for the 4×4 resonator array with $\sim 30 \mu\text{W}$ incident IR power. The reference resonators are the baseline, while the sense resonators show as much as a -1.6 % shift in the relative beat frequency upon illumination.

2.3.2. Response Time

The thermal time constant of the resonators is critical in determining the measurement speed of the IR imager. For 30 Hz - 100 Hz operation, and allowing overheads for processing delays and addressing dead-time, each resonator pixel should ideally have a time constant (including the readout time) on the order of 1 ms - 10 ms. Thin-film resonators are well suited for such fast responses due to their small thermal mass. Experimentally, the response time of the resonant IR detectors is characterized by measuring the rise or fall of the transmission signal level (S_{21}) with respect to switched IR illumination using a manual shutter. In order to ensure fast measurements of the thermal response, the device is stimulated using the network analyzer with a continuous wave (CW) signal with a fixed frequency f_{CW} . The choice of f_{CW} is based on preliminary frequency sweeps in order to identify the frequency

at which the slope of S_{21} is the sharpest [75]. Data are captured using a fast integration bandwidth allowing for sampling at $\sim 20 \mu\text{s}$ intervals. Fig. 2.13(a) shows the measured response for a sense resonator (from the array shown in Fig. 2.11) over a few cycles of switched IR illumination. Fig. 2.13(b) and Fig. 2.13 (c) show magnified regions of the response to illustrate the rise time and fall time for the detector. Two distinct time constants can be extracted: for the heating/cooling of the device, and the heating/cooling of the surrounding regions of the substrate and measurement chamber [13]. The time constants of the device and the substrate can be estimated from curve fitting of the data using a double exponential fit to be approximately $556 \mu\text{s}$, and 1000 s , respectively. The measured time constant is in the same order as the calculated value for this particular design ($270 \mu\text{s}$) [63]; however, a better measurement setup should be used to get a more accurate estimate of the time response and close the gap between measurement and calculations.

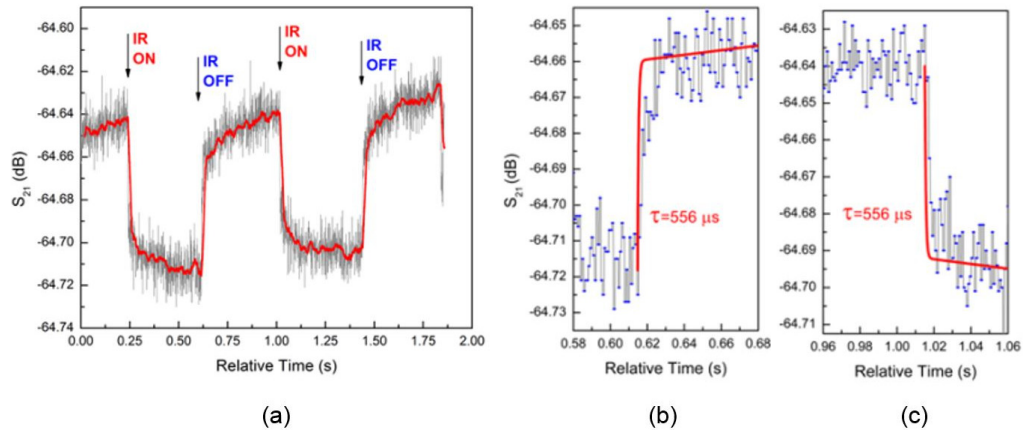


Fig. 2.13 : (a) S_{21} amplitude of the sense resonator under switched near-IR illumination. Measurements are acquired at high speeds to measure the resonator response. Magnified ranges showing cooling and heating time constants based on measured data and curve fitting using double exponential functions to extract the thermal time constants. The slow time constant is due to the non-ideal substrate and surroundings, while the fast time constant ($556 \mu\text{s}$) is a function of the thermal properties of the sensors. The calculated time constant for this device is $270 \mu\text{s}$ [63].

2.4. IR Detector Arrays using Other Materials

While GaN has been used successfully so far for its IR sensitive properties, it is not the ideal material in terms of fabrication. It has to be grown epitaxially on certain specific substrates; and till industrial market volume for GaN grown on (111) Si increase, cost per wafer shall remain high. Most significantly for the IR detector design, the GaN films and their seed or buffer layers of AlN/AlGaN are good thermal conductors, and thus G_{tether} cannot be reduced beyond a point. Neither can GaN be grown on an easily-machined substrate that has low thermal conductivity (apart from (111) Si common substrates for epitaxial GaN are SiC and sapphire).

The concept of using arrays of resonators for IR detection can be extended to materials other than GaN. As these materials may not possess the same pyroelectric-electrostrictive properties as GaN, the resonators will be less sensitive to IR radiation than GaN by a factor of 10-100, based on their thermal properties. The advantages of using other materials and composite structures lie in the simpler fabrication and more flexibility in optimizing the thermal design of the resonators to achieve lower G_{tether} . In the course of this work, we used AlN, AlN-on-Si, and PZT on SiO₂ to design and successfully implement small format IR detector arrays. While the devices were all designed by the author, some devices were fabricated by collaborators. The PZT devices were fabricated at Army Research Labs (ARL), while the AlN-on-Si devices were fabricated using a commercial foundry process in collaboration with Invensense Inc.

2.4.1. AlN

The first successful substitute for GaN was AlN, a material with similar properties, but one that can be sputter deposited at moderate temperatures onto most substrates. A significant advantage of this is that AlN can be deposited onto a metal, removing the necessity of through-wafer DRIE release and sputtering. Stress can be controlled well by tuning the deposition parameters. The resonators can be released from the front using dry gas-phase XeF₂ etching. This drastically improves yield of the resonators. Even with the non-conventional crab-leg tethers, it is seen that the Q is still > 1000 . Arrays of resonant detectors were fabricated using low-stress, high-quality AlN deposited in-house in the Lurie Nanofabrication facility (LNF) (Fig. 2.14). These devices were used as platforms for demonstrating narrowband plasmonic metamaterial based absorbers. Details are provided in Section 2.7

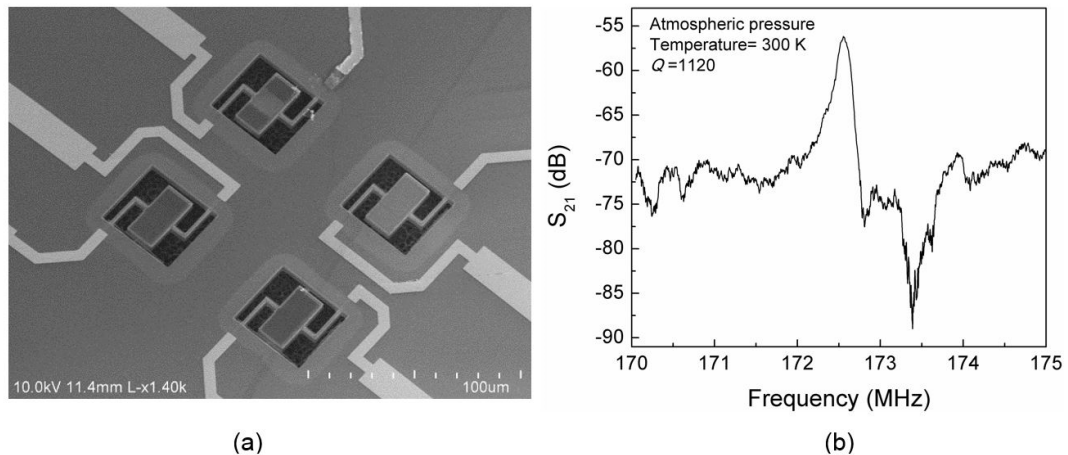


Fig. 2.14 : (a) Array of AlN-based designs, with single-bend crableg designs. The devices are mechanically released using XeF₂. This particular batch was also used as a platform for integrating spectrally selective plasmonic IR absorbers, details of which are provided in Section 2.7 (b) The AlN arrays were successfully fabricated and characterized, and found to have good performance as resonators and IR detectors.

2.4.2. AlN-on-Si

In an ongoing collaboration with Invensense Inc., the concept of resonant IR detectors was adapted to develop AlN-on-Si resonant IR detectors integrated with a CMOS readout IC using a commercial foundry MEMS-CMOS process. Due to the limits imposed by the foundry MEMS process, the size of the resonators on the first validation run was on the order of 200 μm . This offset the fact that the thick AlN and Si layers present on the tethers reduced thermal isolation. We used meander tethers to reduce G_{tether} and aim for the 10 mK NETD goal. The first fabrication run was successful, with both the MEMS chip and the MEMS-CMOS bonded chip yielding measured results with high performance that were responsive to IR radiation (Fig. 2.15). This collaboration yielded the first successful AlN device for Invensense Inc., as well as the first set of resonant IR detectors fabricated using commercial foundry MEMS processes. Future designs aim at optimizing the resonator and array designs, and introducing signal processing and switching on the CMOS readout IC.

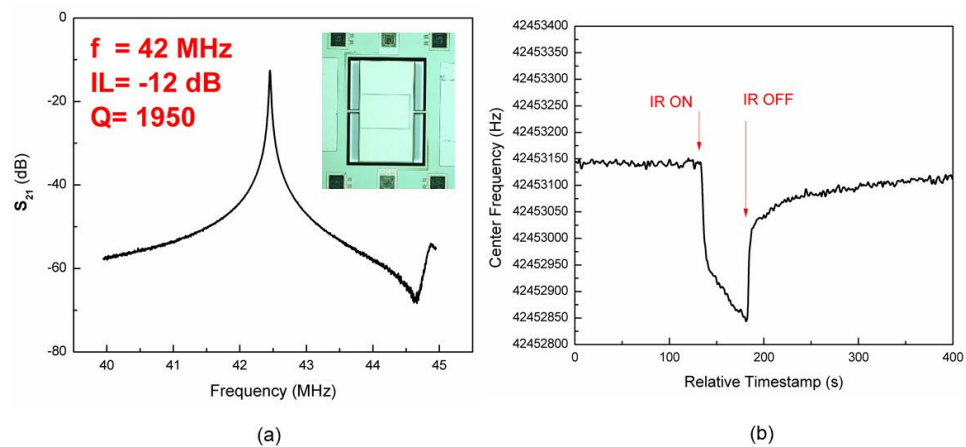


Fig. 2.15 : (a) Measured response of an AlN-on-Si resonator fabricated using a commercial foundry MEMS process. The mechanical performance of the resonator is one of the best achieved so far, with a measured frequency (42 MHz) close to the design value (44 MHz), low IL (-12 dB) and high Q (1950). Inset shows a microscope image of the device. The MEMS dies have been bonded at the wafer level to

CMOS ROICs for routing and pinout. (b) The IR response of the device when illuminated by $\sim 96 \mu\text{W}$ of power. The response time was separately calculated to be on the order of 4 ms.

4.4.3. PZT-on-SiO₂

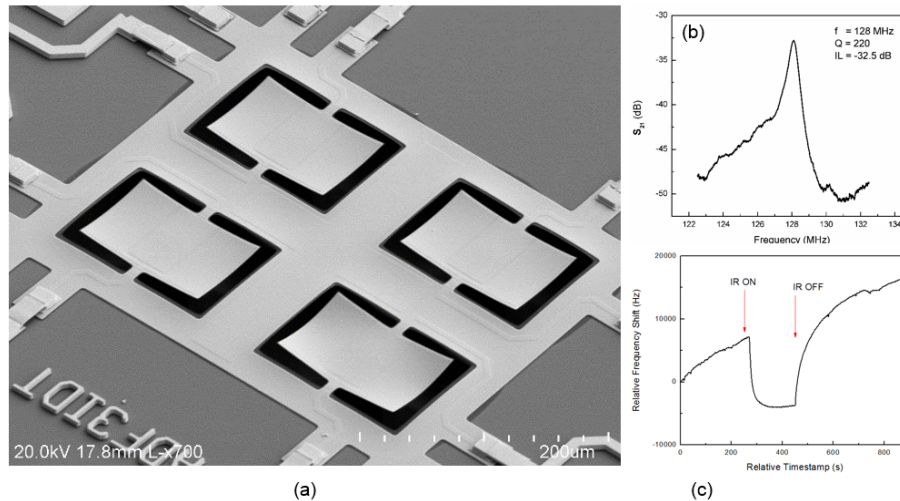


Fig. 2.16 : (a) An SEM image of the PZT-on-SiO₂ IR detector arrays developed in collaboration with ARL. The tethers only have low thermal conductivity materials such as PZT, SiO₂, and thin Pt. (b) While the resonators were found to be working, there is a lot of room for improvement in terms of performance and stability. (c) IR response of the one of these device, coated with PECVD SiN_x, when exposed to $\sim 70 \mu\text{W}$ of absorbed power. The drift of the resonator frequency needs to be addressed. This is part of ongoing and future work.

Some of the best thermal isolation can be achieved by using the PZT-on-SiO₂ process developed by ARL. The tether stack comprises of PZT, Pt, and SiO₂ all of which have low thermal conductivity. Designs were fabricated at ARL and measured at UM. While the results of the first batch were promising, there are some unresolved process issues related to stress, contacts, poling and frequency drift of the resonators that need to be addressed before high resonator and IR detector performance can be achieved.

2.5. Expected Performance for Various Material Combinations

2.5.1. Dynamic Range

The dynamic range of the detector can be considered as the ratio of the maximum temperature change that can be sensed while maintaining a linear response to the minimum distinguishable temperature change. The minimum distinguishable temperature is given by the NETD, while the maximum linear sensing range can be estimated by examining the linearity of the two basic processes: conversion of radiation to a temperature rise in the detector, and the frequency shift in the device. Many resonator materials are known to have non-linear TCF behavior but based on the measured TCF of GaN and AlN based resonators presented in this work, we can assume a linear range between at least -50 °C to +100 °C. The conversion of radiation to a temperature rise is given by Eqn. 2.2 and Eqn 2.16 - Eqn. 2.20. Including the effect of radiation, and for slowly changing IR signals, we can rewrite Eqn. 2.2 as:

$$\Delta T \approx \frac{\eta(\lambda)\phi(\lambda)}{G_{tether} + G_{rad}(T + \Delta T)} . \quad \text{Eqn. 2.26}$$

As the absorbed temperature rises, the amount of heat re-radiated increases since $G_{rad} \propto (T + \Delta T)^3$. When G_{rad} starts becoming non-negligible, the conversion becomes non-linear. The actual magnitude depends on all the factors involved in the above equation, and most specifically on G_{tether} . The lower the G_{tether} , the easier it is to achieve a non-linear response. As discussed before, with changing G_{tether} , NETD changes, and we can write the dynamic range (DR) as the ratio between the

highest temperature change that can be sensed linearly to the lowest temperature that can be sensed.

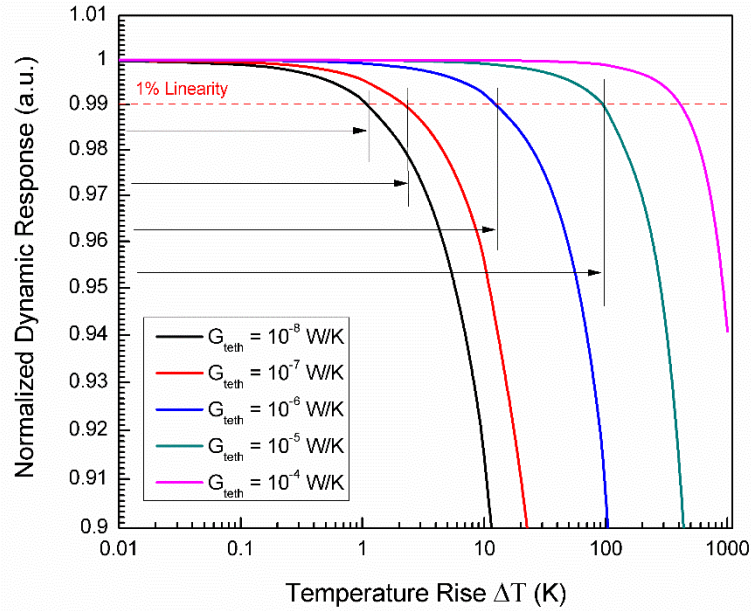


Fig. 2.17 : Normalized calculated linear response range and the input dynamic range for a resonant IR detector with a surface area of $80 \mu\text{m} \times 80 \mu\text{m}$, and an absorber efficiency of 100%. Input dynamic range is defined as the range of temperatures that the device can detect with a response that is 1% linear or better. Increasing the thermal conductance of the tethers improves the maximum linear sensing temperature, at the expense of NETD. The dynamic range is limited by the linearity of the radiative heating process and the linearity of the thermal dependence of frequency.

The input dynamic range is the range of temperature that the $80 \mu\text{m} \times 80 \mu\text{m}$ device can sense linearly and is in the range of 30 dB to 70 dB with G_{tether} in the range of 10^{-8} W/K to 10^{-4} W/K. Practical measurements in the future are necessary to validate this model. It is expected that in practice, higher values of NETD, other non-linearities from convection losses, and non-linearities in the signal processing circuitry will restrict the dynamic range slightly below this theoretical estimate. It is also possible to achieve a significantly higher dynamic range either by allowing a

non-linear response and linearizing the output, or by using high dynamic range algorithms in the output signal processing.

2.5.2. Temperature Coefficients of Offset & Sensitivity

The static or nominal offset of the frequency of the resonators will be decided by processing variability within the array. Specifically, for the differential readout, the offset between the sense and reference resonators will be crucial and will need to be minimized. The temperature coefficients of offset and sensitivity will depend on the difference between the thermal dependencies of the sense and reference resonators. Ideally, the TCF should be identical. However, in reality, there will be small difference between the TCF values, especially at elevated ambient temperatures. This difference is expected to be small ($< 1\text{ppm/K}$), and caused primarily due to the small difference in the structure of the sense and reference resonators. Further extensive characterization is necessary to characterize the temperature coefficient of offset and temperature coefficient of sensitivity. In practice it may be necessary to use pre-deployment calibration to equalize the offset values across the array at various operating temperatures.

2.5.3. Packaging of Imaging Cores

One of the major steps in a practical implementation of an array of resonant IR detectors is the impact on performance due to packaging. The array needs to be packaged suitably to prevent damage to the devices, while at the same time, ensuring that the devices can be illuminated with IR radiation. For the frequency range of

operation used for the prototype devices (in the several 10s of megahertz), vacuum packaging is not needed. The success of the AlN-on-Si devices using a wafer level packaging scheme (with Invensense) implies that it is possible to package the arrays. Further the arrays will need IR imaging optics such as a transmission window (such as Ge). These packaging processes will change the thermal and stress profiles of the devices. The use of a differential sensing scheme can mitigate most of the change in performance due to this stress, but more characterization is needed to verify this.

2.5.4. Expected Performance for Various Material Combinations

The predicted NETD of GaN-based resonators in this work have shown promising results with as low as 50 mK values expected. To further reduce the NETD, an optimized design is necessary (Fig. 2.18). It is possible to reduce the thermal conductance of the tethers by using low thermal conductivity materials such as SiO₂ as the structural elements of the tethers. Further, replacing gold traces and top electrodes with low thermal conductivity materials would also improve the thermal isolation and reduce NETD. The properties of various materials used in these designs are detailed in Table 2.II. Lastly, improving the absorber efficiency to >99% would reduce the NETD up to 5× when compared to devices with silicon nitride absorbers.

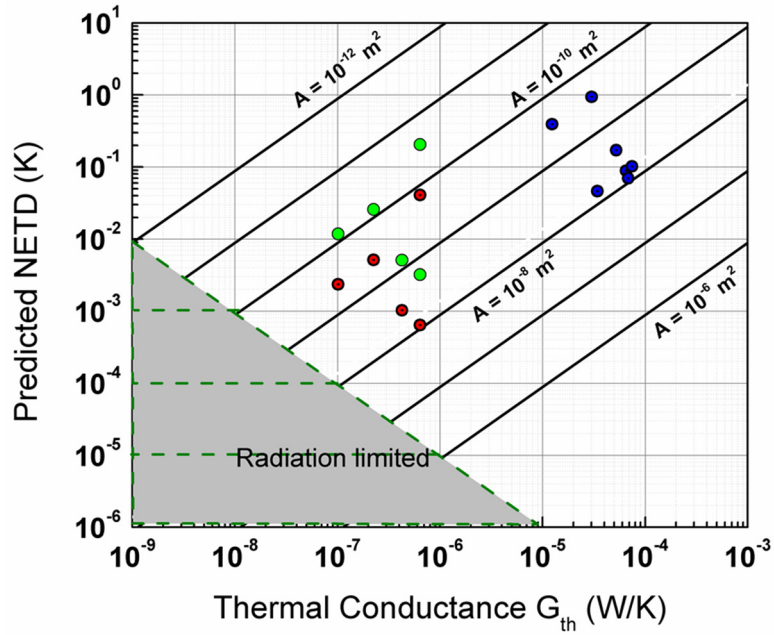


Fig. 2.18: Predicted NETD of fabricated GaN resonant IR detectors (blue circles), with predicted performance improvements using optimized tether materials and designs (green circles) and with absorber efficiency >99% (red circles). The use of composite tethers and high efficiency absorbers can allow low NETD (5 mK – 10 mK) with small area ($\sim 100 \mu\text{m}^2$).

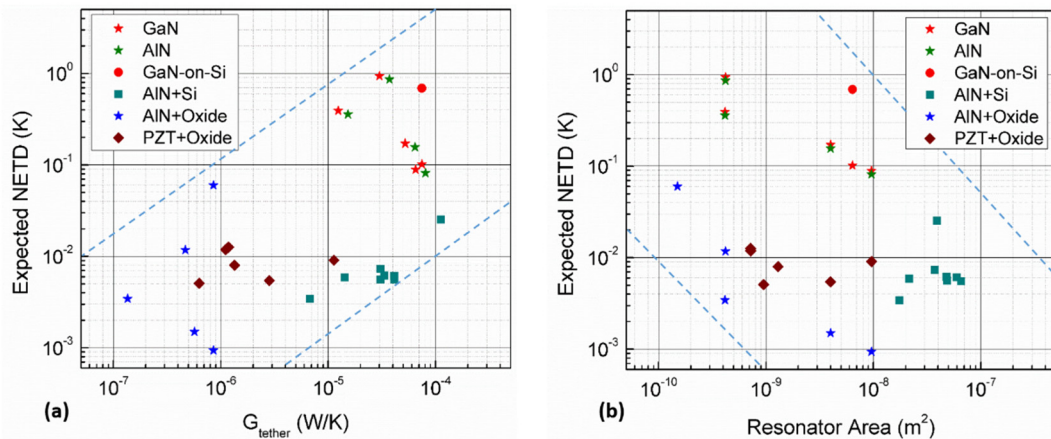


Fig. 2.19 : The expected NETD values as a function of the (a) tether conductance and (b) resonator area for different material combinations and designs that were part of this work. With resonators made from single, high thermal conductivity materials such as GaN or AlN, it is possible to achieve NETD lower than 100 mK, as seen in the measured results. The AlN-on-Si devices have low NETD but are larger in size due to the limitations of the foundry process used to fabricate them. It can be seen that achieving low NETD with both small area and low G_{tether} is possible with composite material stacks.

Table 2.II
Thermal Properties of Materials

	<i>Thermal Conductivity (W/m-K)</i>	<i>Mass Density (Kg/m³)</i>	<i>Specific Heat capacity (J/kg-K)</i>
GaN	130	6150	490
AlN	160	3260	740
PZT	1.2	7800	420
Si	130	2330	700
SiO₂	1.4	2200	1000
Au	318	19300	129
Ti	22	4506	522
TiN	30	3257	136
Pt	71.6	21450	130

We have demonstrated that it is possible to use a number of materials and combinations of materials as the primary transduction element. We can calculate the expected thermal temporal NETD for all the designs used in this work (Fig. 2.19) as a function of G_{tether} and A assuming ideal absorption. This shows us that it is possible to reach low NETD values of 10 mK and below, even with resonator surface areas on the order of $10 \mu\text{m} \times 10 \mu\text{m}$. NETD values between 10 mK and 100 mK have been achieved for many different material combinations, and in the form of detector arrays making this method feasible and scalable for large scale implementation. The last important parameter that is the focus of this work is the absorber efficiency, which is discussed in detail in Sections 2.6 and 2.7.

2.6. Broadband CNT-ND Nanocomposite Absorbers

2.6.1. Motivation: Thin, Broadband IR Absorbers

To improve the efficiency of IR detectors, we require that incident IR radiation is efficiently converted to heat. The standard solution in such cases is the use of a low heat capacity of material on the detector surface which has a high absorbance for a broad spectrum of IR wavelengths. Common methods of achieving this goal involve the use of metal alloys, metal blacks, carbon blacks, and carbon nanotubes. Metal alloys such as porous nickel-alumina have been used [78], with thickness as low as 200 nm, but with limited absorbance (~60%) and a limited spectral range. Along with this, we have a fundamental limitation of using a porous metal. The porous structure is not stable and is highly liable to oxidation. A porous structure entails a low density film, and aging effects tends to increase the density of the film. Various metal blacks have been used as IR absorbers. The most common are gold-black, silver-black and platinum-black [79], with a maximum absorbance of 50%. Unconventional materials such as bismuth-black [80] have demonstrated an absorbance of 80% with a film thickness of 11 μm . The drawback of metal blacks, as with metal alloys, is the film durability. Temperature and aging effects will tend to shrink the films: the density will increase and the films will tend towards the limiting case of the packed continuous film which will not be porous and will be highly reflective. Carbon or graphite blacks have been used by as IR coatings [81, 82]. These films demonstrate

absorbance of up to 85% in the LWIR range, with film thickness on the order of 27 μm .

Another more recent method utilizes vertically aligned arrays of CNTs as broadband visible/IR absorbers [44, 83, 84]. The principle of absorption here is based on trapping light in the sparse and tall CNT arrays. The sparsity enables very close matching of the refractive index to that of free space/air. The height of the arrays (tens to hundreds of microns) allows for multiple internal reflections and the eventual absorption of all incident radiation over a large spectral range. While the measured absorption of these arrays is excellent ($\sim 99\%$) [44], the drawback of this approach is their large mass and thermal loading on the detector.

Ideally, the broadband absorber coating should have a high absorbance over the spectral band of interest, should be thin and light to minimize mass loading on the resonator, and should not load the thermal capacitance of the resonator significantly.

2.6.2. Fabrication of CNT/DND/Polymer Nanocomposite

Previous sections stressed the importance of achieving high absorption efficiency. Conventional solutions use simple materials such as silicon nitride that are reasonably good absorbers in certain parts of the IR spectrum. However, in order to achieve significantly higher absorbance ($\sim 99\%$) over a broad spectrum in the IR, we look to non-conventional absorbers. Broad-spectrum absorbers are the best solution for detection weak signals that are spectrally spread over a range of wavelengths. Such an absorber can be very useful for IR detectors used to detect any unknown activity.

Another advantage of broad-spectrum absorbers is to use them for solar-thermal energy harvesting and in astronomy.

A recent implementation of broad-spectrum IR absorber coating utilizes vertically aligned arrays of CNTs as broadband visible/IR absorbers [44, 83, 84]. The principle of absorption here is based on trapping light in the sparse and tall CNT arrays. The sparsity enables very close matching of the refractive index to that of free space/air. The height of the arrays (tens to hundreds of microns) allows for multiple internal reflections and the eventual absorption of all incident radiation over a large spectral range. While the measured absorption of these arrays is excellent [44], the drawback of this approach is their large mass and thermal loading on the detector. In addition, the high temperatures and catalytic surfaces required for vertical CNT arrays, the precise sub-micron lithography required for SPR absorbers, and the etch chemistry control required for porous metal and metal-black films make these methods prohibitive for economical, large-scale fabrication. In a separate approach, researchers have fabricated horizontally dispersed CNT mats for infrared absorption using vacuum filtration [85-88] or airbrushing [89]. Neither method gives the desired combination of very thin films that are mechanically stable and can be further patterned or processed. Hence we develop a new thin-film nanocomposite that is mechanically stable and highly absorbing for IR radiation. In the procedure described in detail elsewhere [90, 91] and summarized below, CNT powder is commercially purchased at low cost and mixed with a polymer (*i.e.* poly-(methylmethacrylate) (PMMA)) [92] in order to provide the eventual film with the required mechanical and

thermal stability, and amenability to post-processing. In the spun layers of CNT/PMMA, the orientation of the CNTs is generally horizontal and follows no particular order, other than the strong tendency to agglomerate into bundles due to surface forces [21, 92, 93] (Fig. 2.20 (a) and (b)). The agglomeration of CNTs in the polymer can be prevented by mixing surfactants to separate the CNT bundles. In this work, electrically charged DNDs are used as effective surfactants, counteracting the CNT agglomeration by electrostatic repulsion [93]. Unlike liquid surfactants, the DNDs are not volatile and remain in the film after spinning and baking (Fig. 2.20 (c) and (d)). The DNDs used in this work have an average diameter of 30 nm, a ζ -potential of +45 mV (Fig. 2.20 (e)). Ultrasonication aids with dispersing CNTs in the polymer by shearing the CNTs, but is largely ineffective without the DNDs. Further addition of dimethylsulfoxide (DMSO) as a liquid surfactant helped with achieving lower viscosity and thus thinner films. For films having 0.6 w/v % DND and 0.2 w/v % CNT in DMSO, we were able to achieve excellent dispersion of the CNT films with surface roughness in the range of 50 to 100 nm [90], over a substrate size of 25 mm \times 25 mm (Fig. 2.200 (c) and (d)). This is in stark contrast to the large (\sim 10 μ m thick) agglomerates encountered prior to the addition of the DNDs and thus the addition of DNDs proved crucial to this process. With a low spin speed ($<$ 500 rpm), we were able to get consistent, visibly black films on a glass substrate, with a thickness on the order of 300 nm per layer. Following the spinning process, the films were baked on a hotplate at 110 $^{\circ}$ C to evaporate the DMSO solvent and cure the polymer. This bake step represents the maximum temperature used in this entire

process. Multiple layers of the film can be sequentially deposited to increase the film thickness if needed. The films discussed in further sections have multiple layers resulting in measured thicknesses of 1600 nm and 2000 nm (5 and 7 layers, respectively). The final CNT/PMMA/DND layer is mechanically and thermally stable and can be spin-coated on a substrate and patterned using standard photolithography and plasma etching. The spun-on absorber retains its properties up to temperatures of 300 °C or laser damage of up to 28 mJ/cm² [46].

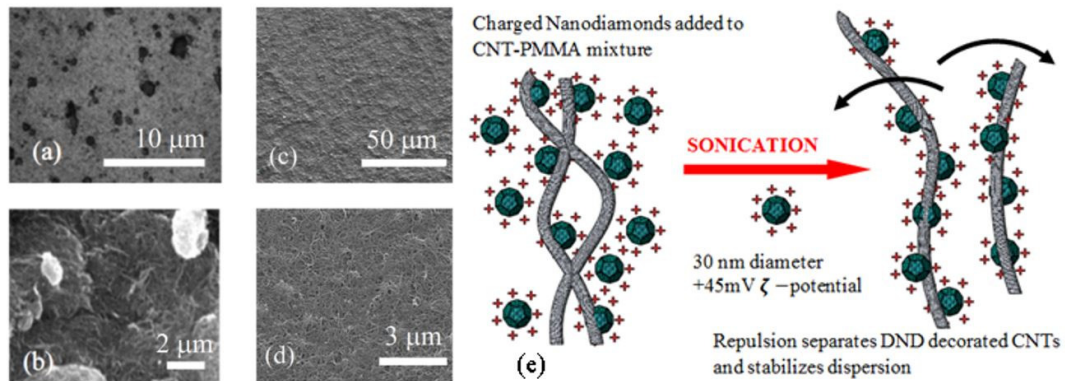


Fig. 2.20 : (a), (b) Large agglomerates seen in the CNT/polymer films without the charged DND particles. (c) A SEM image of a thin film of CNT/DND in the PMMA matrix, showing that CNTs are stably enmeshed in the film with the addition of charged DNDs. (d) Magnified image of the same layer as (c), showing the grid like structure of the film. (e) Dispersion mechanism of CNT bundles by charged DND clusters via de-bundling and dispersion in a polymer/solvent mixture [93]. The dispersion remains stable and the CNTs remain separated even when the volatile liquid solvent evaporates and the polymer/CNT is baked into a solid film.

2.6.3. Measured IR Absorption

To characterize the IR absorption properties of the CNT/DND based polymer, normal incidence reflection $R_{exp}(\lambda)$ and transmission $T_{exp}(\lambda)$ measurements are acquired on glass slides coated with the thin films using a Perkin Elmer Spectrum GX in the spectral range of 4000 cm⁻¹ to 14000 cm⁻¹ with a spectral resolution of 4 cm⁻¹. Transmission measurements are normalized to an identical uncoated glass substrate,

while reflection measurements are normalized to an uncoated glass substrate placed on a gold coated standard (Fig. 2.21) [94, 95]. Absorption for the film ($A_{exp}(\lambda)$) is calculated as $A_{exp}(\lambda) = 1 - R_{exp}(\lambda) - T_{exp}(\lambda)$. Measured results for the two samples demonstrate a high broadband absorption (Fig. 2.22(a)). The effect of pure PMMA is considered; as shown in (Fig. 2.22 (b)). PMMA does not contribute significantly to the absorption.

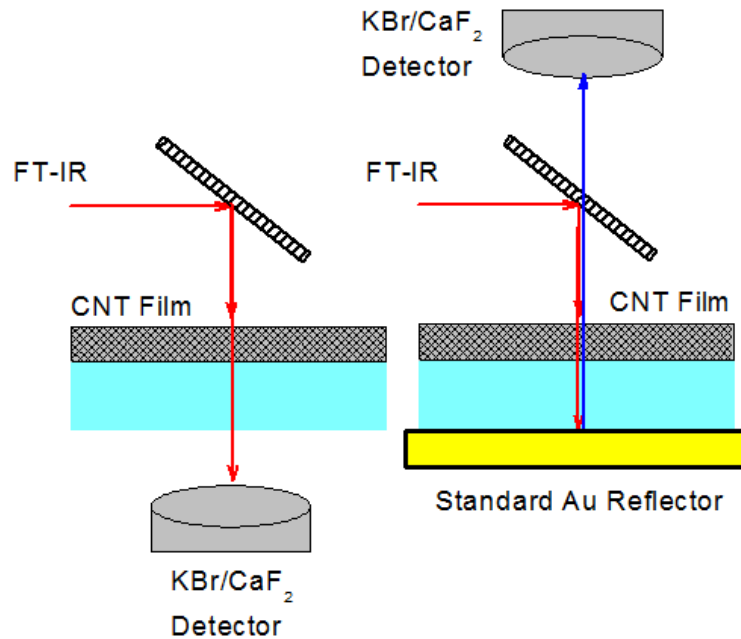


Fig. 2.21: A schematic of the normal incidence transmission and reflection test setup. The measurements are normalized using uncoated glass substrates for transmission and a standard gold reference for reflection.

Optical properties of ordered arrays of nanotubes can be analytically modeled [96]. However, because of the random dispersion of CNT/DNDs in the polymer, accurate modeling of the optical properties are challenging for the presented films. Instead, the optical constants are extracted (Fig. 2.23) from the measured results using an effective media approximation [46]. Physically, the absorption in the film has significant contributions from scattering due to the many scattering centers

provided by the well-dispersed CNTs with a diameter much smaller than the wavelength, as well as the intrinsic absorption provided by the CNTs. The small DND particles are not expected to contribute significantly to the optical absorption. These well-dispersed and dense films have at least an order of magnitude higher extinction coefficient k than vertically aligned CNT forests of the same thickness [84]. Increasing the density and improving the dispersion homogeneity of the CNTs in the matrix can further increase scattering and improve the effective extinction coefficient of the films.

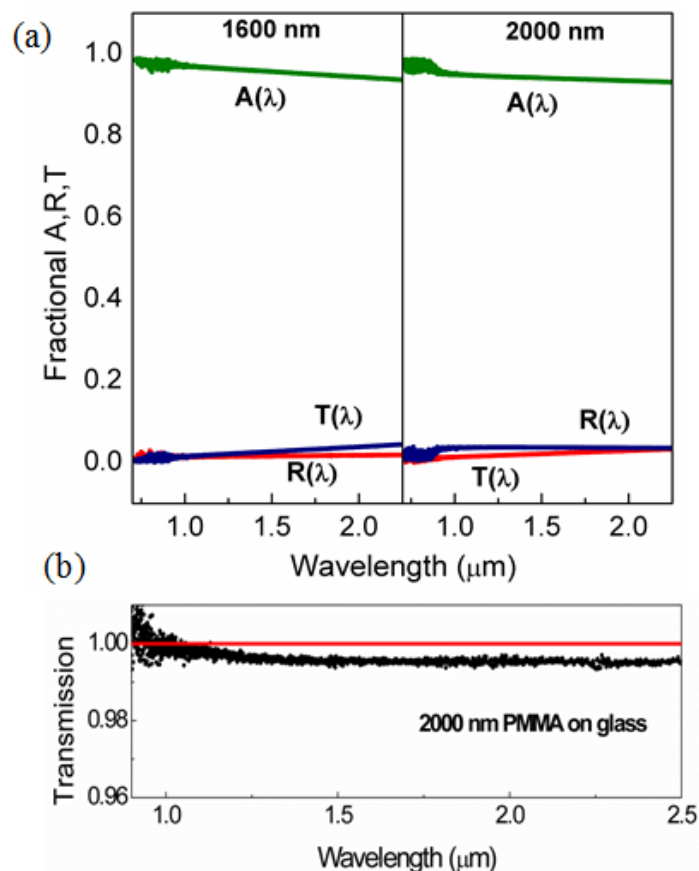


Fig. 2.22 : (a) The reflection, transmission, and the absorption of the 1600 nm and 2000 nm films. The average absorbance for both films is $\sim 95\%$ across the entire spectral region. (b) Transmission measurement for a 2000 nm thick layer of PMMA on a glass substrate, indicating that the PMMA itself does not contribute significantly to the IR absorption.

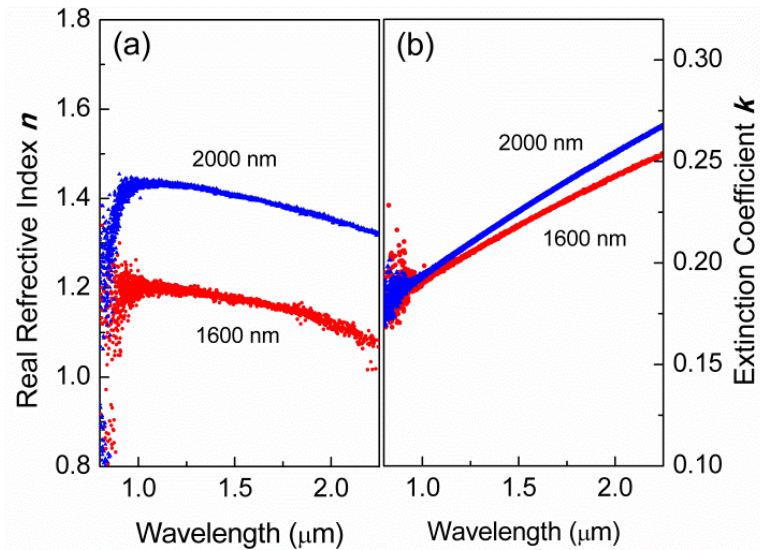


Fig. 2.23 : (a) Extracted effective n for the measured films. (b) Extracted effective k for these films is more than $10\times$ higher than that for aligned CNT forests, resulting in increased absorption in a significantly lower thickness.

The CNT-DND films can be patterned lithographically and etched in an oxygen plasma. This makes integration with resonant IR detectors (or any other system) easily possible. The films have been tested at high temperatures and with a high power laser to assess the ageing characteristics and thermal degradation [46]. It is seen that the CNT-DND films are mechanically and thermally robust and have high damage thresholds.

2.7. Narrowband Spectrally-Selective Plasmonic Metamaterial Absorbers

2.7.1. Motivation

The logical complement to broadband IR absorbers is the development of narrow-spectrum, selective absorbers that can be designed for specific wavelengths for multi-

spectral imaging, spectroscopy, or decoy rejection. The use of narrowband (or spectrally selective) IR absorber coatings can enable thermal detectors to achieve the type of narrowband response normally only possible with photonic detectors or specifically designed quarter-wavelength absorber cavities. Narrowband IR detectors can be used for multi-spectral and hyperspectral imaging, where IR information from multiple spectral bands is combined to give a more meaningful image [97].

2.7.2. Theory and Design

Narrow band, spectrally selective absorbers can be implemented using metal-insulator-metal (MIM) subwavelength plasmonic structures that utilize surface plasmon resonance (SPR) for selective absorption of electromagnetic radiation [98-100]. SPR-based devices have been shown to provide high spectral selectivity [98], strong light absorption [99], simplicity of design and fabrication [101], and compact form-factor [102]. The physical mechanism that enables the selective optical absorption in the MIM may be modeled with a Fabry-Perot cavity model [99] governed by the following relation:

$$\lambda_r = 2n_{eff}w + \frac{\phi}{\pi} \lambda_0. \quad \text{Eqn. 2.27}$$

Here,

λ_r is the SPR resonance wavelength,

n_{eff} is the effective index of the guided surface plasmon-polariton (SPP) mode,

w is the strip width,

λ_0 is the vacuum wavelength, and

ϕ is the phase shift incurred upon reflection from the strip terminations.

2.7.3. Fabrication and Characterization

The appropriate wavelength and the peak absorption may be chosen by choosing the right materials and dimensions using known analytical models for metallic slits and FEA simulations (Fig. 2.24(a)). We choose to design for the 10 μm LWIR wavelength. The structure uses the resonator top electrode as the bottom metal in the MIM stack and 200 nm thick SiO_2 as the insulator. The top plasmonic grating consists of 35 nm thick Ti/Au strips with designed width of 750 nm and gap of 100 nm. The top metal grating was defined by electron beam lithography. The plasmonic absorber is characterized using a PerkinElmer spectrometer fitted with a polarizer and show up to 46% absorption at the expected wavelength of 10.15 μm , which is lower than the simulated value of 80% possibly due to deviation of material properties from those used in simulations. While this absorber design is polarization sensitive (Fig. 2.24(b)), similar polarization-insensitive structures can be readily integrated with the presented resonant detectors.

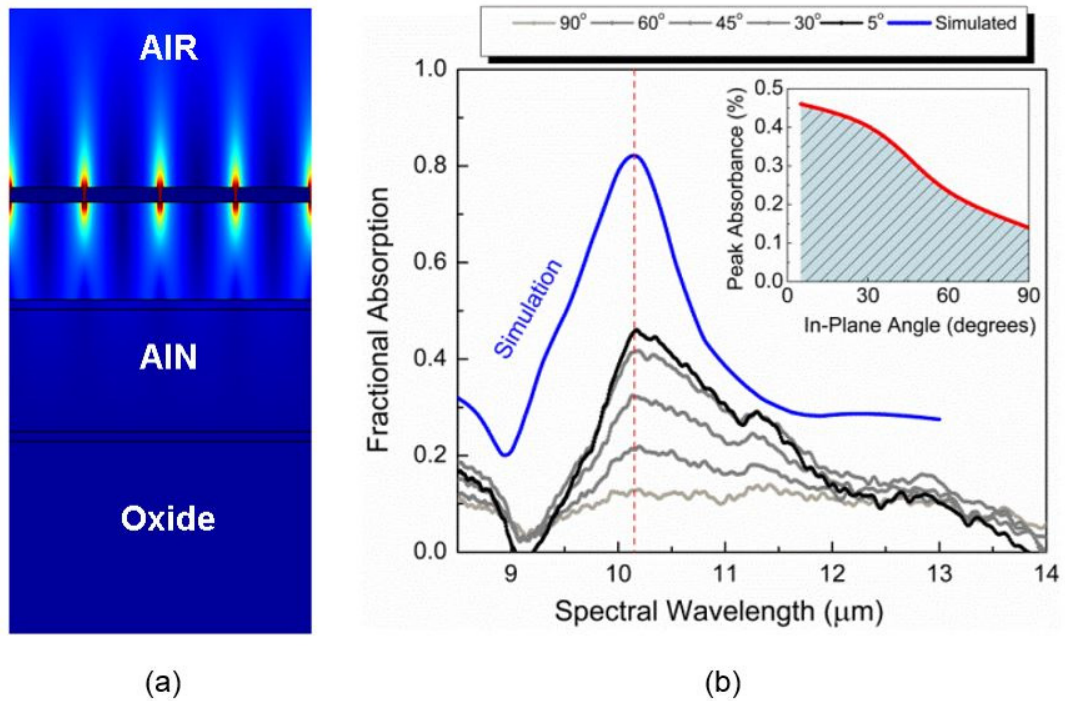


Fig. 2.24 : (a) Simulated EM field confinement for the MIM structure used as the selective plasmonic absorber. The design is for a maximum absorption in the LWIR spectrum, at a wavelength of 10.15 μm . (b) Measured data acquired using a spectrometer, compares favorably with simulation with respect to wavelength, but the absorption magnitude has room for improvement. Inset shows the polarization angle dependence of the grating absorbers.

This is the first demonstration of resonant infrared detectors with integrated nanostructured subwavelength plasmonic gratings designed to selectively absorb long wavelength infrared (LWIR) radiation (Fig. 2.25). The resonant detectors are also the smallest in size demonstrated so far ($30 \mu\text{m} \times 14 \mu\text{m}$). The absorbers are optimized for a spectral wavelength of 10.15 μm and experimentally demonstrate an absorbance of 46% with a Full Width at Half Maximum (FWHM) of 1.7 μm . It can be seen that even for such a small detector, non-ideal thermal sources such as human hands or heated solder tips cause perceptible shifts in the operating frequency (Fig. 2.25(d)).

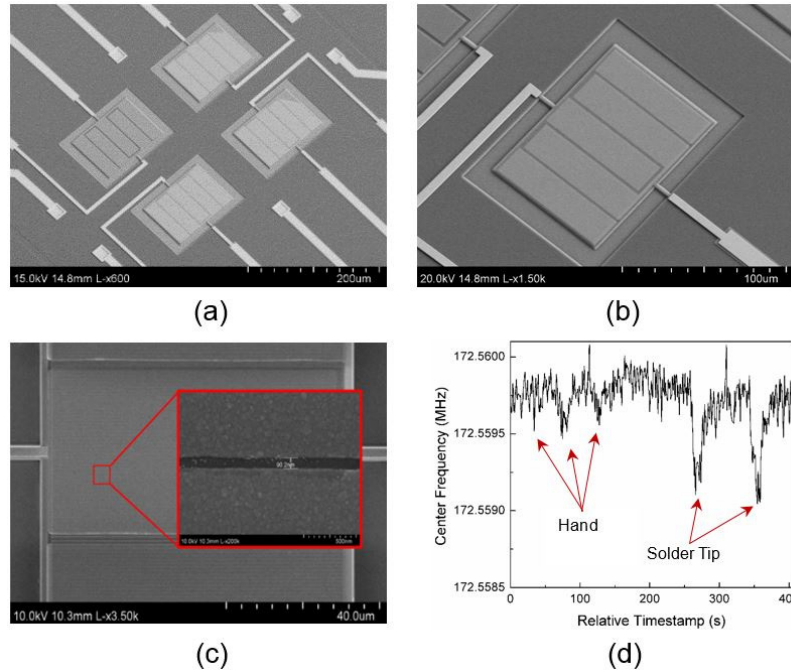


Fig. 2.25 : (a) A SEM image of an array of resonant IR detectors with three sense resonators covered with the MIM plasmonic structures and one uncoated reference. (b) & (c) Magnified SEM images showing the well-defined plasmonic grating with 750 nm wide strips and fabricated gap of 90 nm (design value was 100 nm). (d) Frequency response of a $30 \mu\text{m} \times 14 \mu\text{m}$ AlN+plasmonic resonant detector to human hands ($\sim 30 \text{ }^\circ\text{C}$) briefly held 10 cm above the detector, and a heated solder tip at ($\sim 260 \text{ }^\circ\text{C}$). Both thermal sources change the resonant IR detector response. This is the first measured result for LWIR plasmonic absorbers integrated with resonant detectors.

In summary, it is seen that both broadband and narrowband IR absorber coatings have been successfully implemented and characterized. These films have a high absorbance per unit thickness, have a low mass, and do not thermally load the small resonators. Tests on the CNT layers have shown that they have low ageing and damaging thresholds and work well at elevated temperatures.

Chapter 3 Characterization of GaN Resonators

3.1. Need for Electromechanical Characterization of GaN

Over the recent few years, GaN has become one of the most popular semiconductor materials in use [103-105]. While the current cost of GaN substrates is high, based on the economics of scale, high-volume production of GaN wafers is expected to reduce the wafer cost to the same level as GaAs substrates [103]. In addition, epitaxial growth of high quality GaN on low-cost substrates, such as Si, is becoming more mature. This would make GaN one of the cheapest semiconductors, second only to Si. While a significant amount of research has been devoted to GaN-based optoelectronics, RF & high-power electronics, little attention has been given to the use of GaN for nano and microelectromechanical systems (N/MEMS) applications. Unlike Si, GaN is a piezoelectric semiconductor and one can envision using the piezoelectric properties of GaN alone to manufacture multitude of devices for diverse applications. In this work, we focus on the piezoelectric and high-frequency electromechanical properties of GaN in order to implement high-performance piezoelectric electromechanical resonators using GaN. A more comprehensive review of the state-of-the-art for the electromechanical properties of GaN is found in [66].

3.2. Epitaxial GaN films

3.2.1. Epitaxial Growth

GaN thin films are grown on (111) silicon substrates using either molecular beam epitaxy (MBE) or metallo-organic chemical vapor deposition (MOCVD). GaN-on-Si wafers used in this work have been purchased from SOITEC [8] and Nitronex Corp [71]. GaN-on-Si wafers provided by SOITEC were MBE grown. Details of the SOITEC MBE stack are unavailable. The Nitronex unintentionally doped (UID) GaN films were epitaxially grown on 100 mm silicon substrates, using a custom-built cold-wall rotating disc MOCVD reactor. The growth temperature was 1020 °C. The full epitaxial stack consists of an AlN nucleation layer, followed by two AlGaN layers, which complete the transition layer (Fig. 3.1).

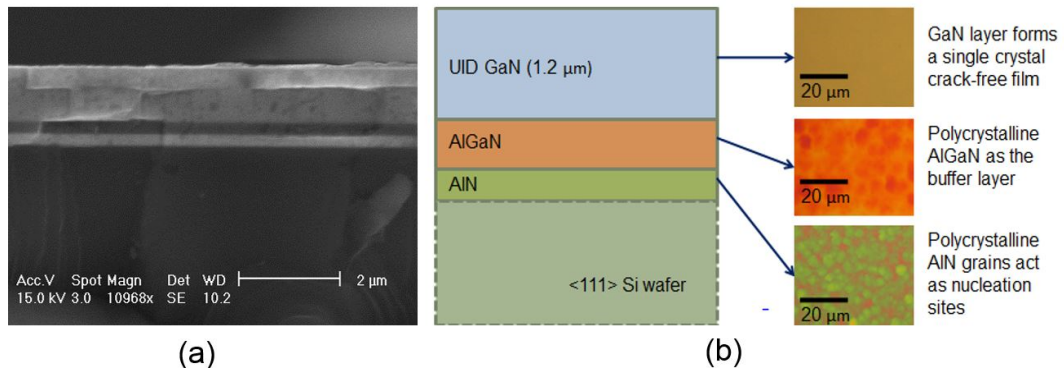


Fig. 3.1: (a) Cross-section SEM images of a cleaved GaN film grown on a Si (111) substrate. A transition or buffer layer of AlN and $\text{Al}_x\text{Ga}_{1-x}\text{N}$ is necessary in order to reduce the lattice mismatch between the Si and GaN crystals. This buffer layer is seen in the SEM image. (b) Schematic of the GaN wafer along with optical images of each layer after etching down using dry etching. The transition from the polycrystalline AlN nucleation layer to the single crystal GaN can be clearly seen.

A thicker GaN film was subsequently grown on top of the transition layer. The transition layer is required to alleviate the problem of film stress caused by the

lattice mismatch between the Si substrate and the GaN epitaxial layer. Cross-section SEM images of the GaN layer confirm the film structure and thickness (Fig. 3.1).

3.2.2. Crystal Quality

GaN in its wurtzite form has a crystal structure with lattice parameters of $a = 3.189 \text{ \AA}$ and $c = 5.185 \text{ \AA}$. A figure of merit that is commonly used to characterize the intrinsic crystalline quality of an epitaxially grown thin film is the Full Width at Half Maximum (FWHM) acquired using X-Ray Diffraction (XRD) analysis. A narrow FWHM denotes high long range crystalline order and good internal alignment of the crystal (Fig. 3.2). Measured values are well within the reported range for (0002) GaN (*i.e.*, 0.18° to 0.6°) [106].

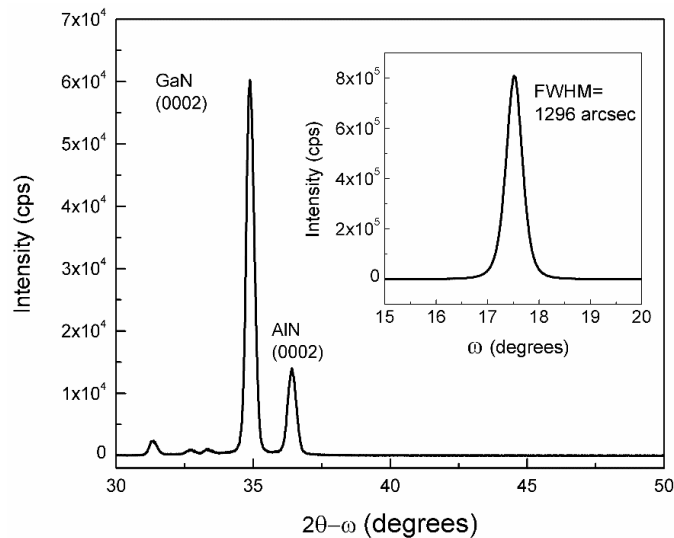


Fig. 3.2: A representative result showing XRD spectroscopy on a GaN thin film grown on a Si (111) substrate using MOCVD. Inset: Rocking curve of the (0002) GaN plane exhibits a very clear peak and a FWHM of 1296 arcsec.

3.2.3. Dry Etching of GaN

Currently, plasma-based chemical dry etching is the most commonly used patterning technique for group III-nitrides. The mechanisms and variations have been reviewed in detail by Pearton *et al.* [107]. In particular, high-density electron cyclotron resonance (ECR) and inductively coupled plasma (ICP) etch processes have yielded smooth, highly anisotropic, etch characteristics. Etch rates that can exceed 1.0 $\mu\text{m}/\text{min}$ can be achieved. Halogen-based plasma chemistries (Cl-, I- and Br-based plasmas) yield high-quality etch characteristics. The choice of the reactive source gas (Cl_2 , BCl_3 , ICl , IBr , *etc.*) and secondary gases (H_2 , N_2 , Ar) changes the concentration of reactive neutrals and ions in the plasma, which directly correlates with the etch rate. The process parameters used for anisotropic etching of GaN in this work [63, 71, 91, 108-112] are shown in Table 3.I. This process results in smooth, vertical sidewalls. As expected, increasing gas flows within a range increases the isotropicity of the etching process. The process flow for fabricating GaN resonators was discussed in Chapter 2.

Table 3.I
Process Parameters for ICP Etching of GaN

Parameter	Unit	Value
Chamber Pressure	mTorr	5 -10
Cl_2 Flow rate	sccm	24-36
BCl_3 Flow rate	sccm	6-10
Ar Flow rate	sccm	5-8
He Pressure (wafer backside cooling)	Torr	8
ICP Power	W	500
RF Bias Power	W	50-100
Etch Rate (anisotropic)	nm/min	~200

3.3. Electromechanical Properties of GaN

3.3.1. Elastic and Hardness Moduli

The mass density of GaN has been quoted in the literature as 6095 kg/m³ [113, 114] or 6150 kg/m³ [104]. Due to its hexagonal nature, the elastic properties of wurtzite GaN are symmetric along the in-plane vectors. The elastic moduli of w-GaN have been calculated by Wright using ab-initio density field calculations [115] and verified using Brillouin scattering by Yamaguchi *et al.* [116] and Polian *et al.* [113].

The full stiffness matrix for GaN is given by:

$$C_{ij} = \begin{pmatrix} 390 \pm 25 & 145 \pm 20 & 106 \pm 20 & 0 & 0 & 0 \\ 145 \pm 20 & 390 \pm 15 & 106 \pm 20 & 0 & 0 & 0 \\ 106 \pm 20 & 106 \pm 20 & 398 \pm 20 & 0 & 0 & 0 \\ 0 & 0 & 0 & 105 \pm 10 & 0 & 0 \\ 0 & 0 & 0 & 0 & 105 \pm 10 & 0 \\ 0 & 0 & 0 & 0 & 0 & 122.5 \pm 20 \end{pmatrix} \text{ GPa}$$

The elastic compliance and constants for the binary compounds as well as the rule to obtain the values for alloys are summarized by Ambacher *et al.* [104]. Knoop hardness of GaN was reported to be 14.21 GPa [104] and agrees well with experimental data obtained for GaN-on-Si samples in this work (Table 3.II). The microhardness of single crystal GaN thin films is reported to be 10.2–19 GPa [104, 117]. Here, nanoindentation experiments leading to the mechanical properties of GaN films have been obtained by nanoindenter and a Berkovich tip. The nanoindentation measurements were performed using the continuous stiffness measurement (CSM) method, where a small oscillation is superimposed to the primary loading signal [118].

Nanoindentation tests carried out in the course of this work indicate that the hardness for different types of substrates and fabrication methods consistently lies in the range of 20-26 GPa. GaN Young's moduli reported in Table 3.II are higher when the material is directly grown on the bulk c-Sapphire or (111) Si substrate. It is significantly lower when the thickness of GaN grown on Si is less than 3 μm , indicating probable influence of the crystal quality on the Young's modulus.

Table 3.II
Mechanical Stiffness and Hardness Moduli for GaN

Substrate	Fabrication Technique / GaN thickness	Hardness (GPa)	Young's modulus (GPa)	Indenter tip	Ref.
Bulk	-	12 ± 2	287	Vickers	[119]
Bulk	-	18-20	295 ± 3	Berkovich	[120]
c-Sapphire	MOCVD / 1.3 - 2.4 μm	53.6	290	Berkovich	[121]
c-Sapphire	MOCVD / 1.8 - 4 μm	15.5 ± 0.9	210 ± 23	Spherical	[122]
c-Sapphire	MOCVD / 2 μm	19 ± 1	286 ± 25	Berkovich	[123]
buffer/(111) Si	MBE / 2 μm	22.7 ± 3	266 ± 43	Berkovich	This work
c-Sapphire	MOCVD / 1 μm	25.5 ± 0.6	405 ± 7	Berkovich	This work
buffer/SOI	MOCVD / 1.5 μm	23 ± 2.3	288 ± 21	Berkovich	This work

3.3.2. Acoustic Properties

As a hexagonal piezoelectric material, GaN can be used to implement acoustic transducers. While conventional acoustic transducers use very strong bulk ferroelectrics for actuation on the macro-scale (for applications such as sonar and ultrasound), there is a growing trend for using materials such as thin-film PZT and AlN in micro-acoustic implementations, such as piezoelectric micro-machined

ultrasonic transducers (pMUTs) [124, 125]. GaN can be a very attractive option for high output power, high-frequency capable acoustic transducers, with the added advantage of co-fabrication and integration with the necessary drive and control electronics. The slowness curves for GaN (inverse of acoustic velocity) as a function of propagation vector for both in-plane and out-of-plane modes can be calculated based on the stiffness matrix (Fig. 3.3).

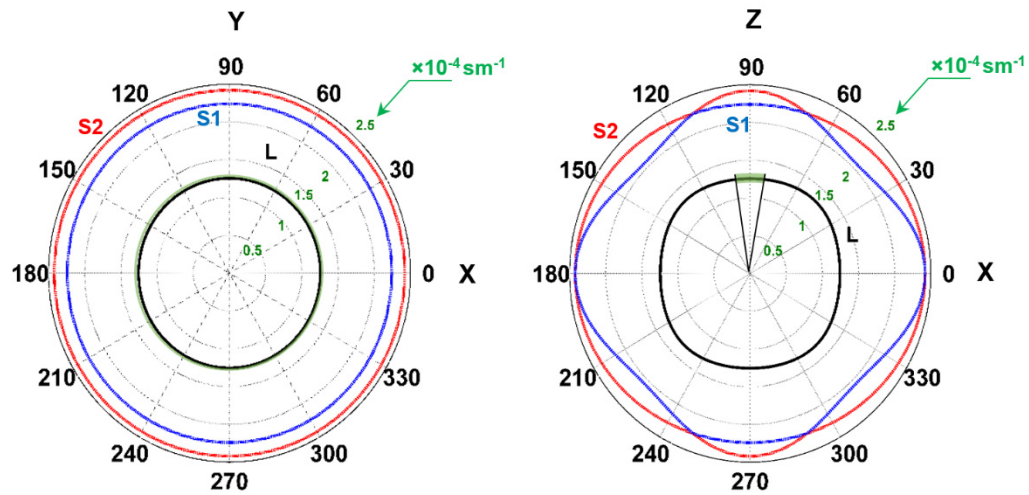


Fig. 3.3: Calculated slowness curves for GaN for in-plane and out-of-plane acoustic wave propagation. The green shaded regions indicate the slowness values extracted from the frequency of resonators in this work and reported in [64, 91, 108, 111, 126-128]. The measured velocities match well with theoretical estimates.

For a majority of resonant devices described in this work, the mode of operation depends on longitudinal waves trapped in the mechanical resonant cavity. The values for extracted acoustic velocity from these resonant devices match the expected longitudinal velocities in plane (7960 m/s) and along the c-axis (8044 m/s). Extracted longitudinal velocities for a number of GaN resonators from this work [64, 91, 108, 111, 126-128] lie in the range of 7200 m/s to 7800 m/s. Slight deviations from the exact theoretical velocity values could be attributed to the effect of a small tilt of the

c-axis of the manufactured thin films, and the loading due to metal electrodes and buffer layer on the real devices. The mass density is assumed to be 6150 kg/m^3 for all calculations. The longitudinal velocities of GaN (both in-plane and out-of-plane) are very similar to that of crystalline Si. In the popular thin-film piezoelectric-on-Si (TPoS) configurations [129-132], the use of GaN as the transduction layer on Si has the potential to reduce acoustic loss as the acoustic velocities in both materials are very similar.

Acoustic waves travelling through GaN, like any other elastic material, are attenuated via a number of intrinsic scattering processes. A comprehensive knowledge of the loss mechanisms is crucial to designing highly sensitive and energy efficient electromechanical devices. The study of these loss mechanisms is a part of this work and have been discussed in detail in [24] and Chapter 4.

3.4. Performance Metrics for GaN Resonant Devices

3.4.1. Quality Factor and $f \times Q$ Limits

The Q of an acoustic resonator is directly related to the total energy lost, which is quantified by the attenuation coefficient. The highest Q for a GaN resonator measured in this work was 12185 at a frequency of 120 MHz (Fig. 3.4).

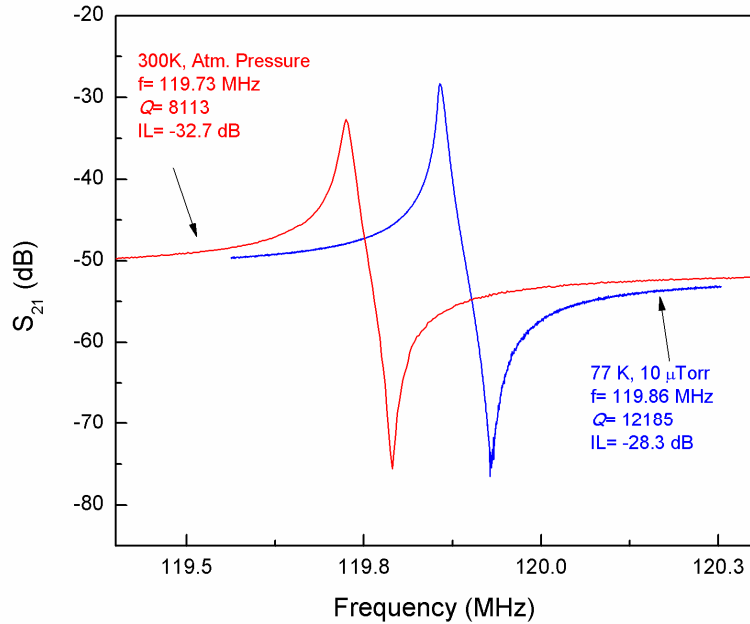


Fig. 3.4: The best Q measured in our lab was on a $40 \mu\text{m} \times 80 \mu\text{m}$ length-extensional mode GaN resonator. The RF transmission (S_{21} curve) at room temperature and ambient pressure is shown in red, showing a Q of 8113. The Q improves to 12185 at 77 K and 10 μTorr . IL also improves at the lower temperature and pressure, while frequency increases.

One of the most important metrics for mechanical resonators is the product of frequency and Q , which is inversely proportional to the loss in the device. The measured values of the resonator $f \times Q$ are a good indicator of how close the resonator is to the limiting values. Fig. 3.5 shows the $f \times Q$ limits of GaN due to different loss mechanisms and compares that to the measured data (red dots) from GaN resonators presented in the previous sections. A more detailed discussion of loss mechanisms is presented in Chapter 4.

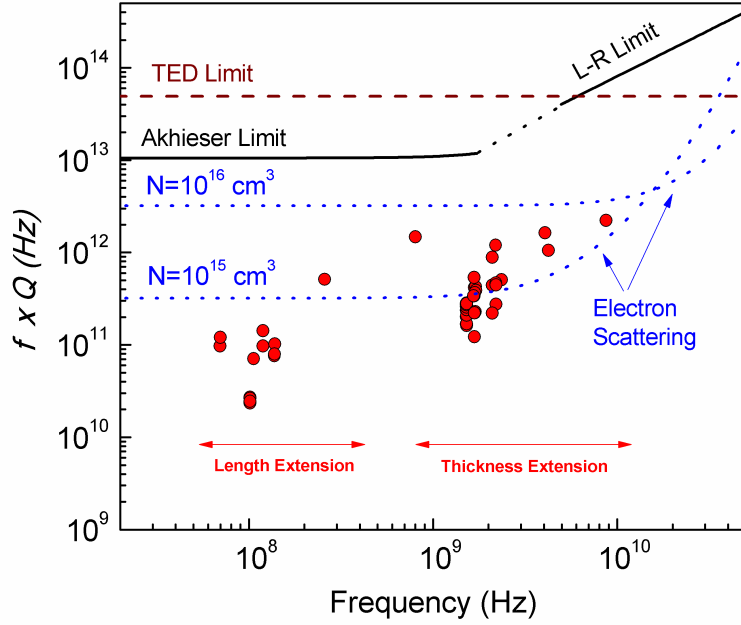


Fig. 3.5: Calculated values of the $f \times Q$ limits for the dominant intrinsic dissipation mechanisms in GaN. Measured results from this work are shown in red dots. The measured values compare favorably with work by other researchers [126, 127, 133-135].

3.4.2. Coupling Efficiency and the $k_{eff}^2 \times Q$ Metric

The piezoelectric coupling coefficient k_t^2 is a material property that determines the efficiency of converting electrical energy into mechanical energy and vice-versa [136]. For the various electromechanical axes of GaN, the values of k_t^2 range from 1.3% to ~2% [137, 138]. The effective coupling coefficient k_{eff}^2 is extracted from the mechanical response of the resonators and includes the effects of metal electrode loading, non-ideal electrode area coverage, and anisotropic effects [137]. Measured values of k_{eff}^2 in prior literature (Fig. 3.6(a)) are seen to be close to the calculated maximum values for both the thickness modes and in-plane modes.

$$k_t^2 = \frac{e_{ij}e_{kl}}{\epsilon c_{ijkl}} \quad \text{Eqn. 3.1}$$

Practically, for a mechanical resonator k_t^2 can be estimated as [136]

$$k_t^2 \approx \frac{f_s - f_p}{f_s}, \quad \text{Eqn. 3.2}$$

where f_s and f_p denote the series and parallel frequency of the resonator. Theoretical investigations into the piezoelectric coupling coefficient of un-doped or high-resistivity GaN have consistently yielded values close to $\sim 1.9\%$ for the thickness mode [139].

Another related metric that is used often for characterizing the applicability of a piezoelectric material for use in RF electromechanical filters is the $k_{eff}^2 \times Q$ product. Practically, a higher resonator k_{eff}^2 increases the separation between the series and parallel resonances. For coupled-resonator filter topologies, this higher separation implies a wider bandwidth. A higher Q (for each individual resonator) imparts a sharper roll-off for the filter. Thus, a high $k_{eff}^2 \times Q$ product is desirable for wide-band RF filters [137]. In this regard, measured GaN resonators have demonstrated similar numbers (Fig. 3.6(b)) in comparison with Quartz, Diamond, TPoS and Si-based internal dielectric transduction. However, it is significantly lower than stronger piezoelectric materials such as LiNbO₃ [140], or highly optimized devices such as the AlN FBAR [141].

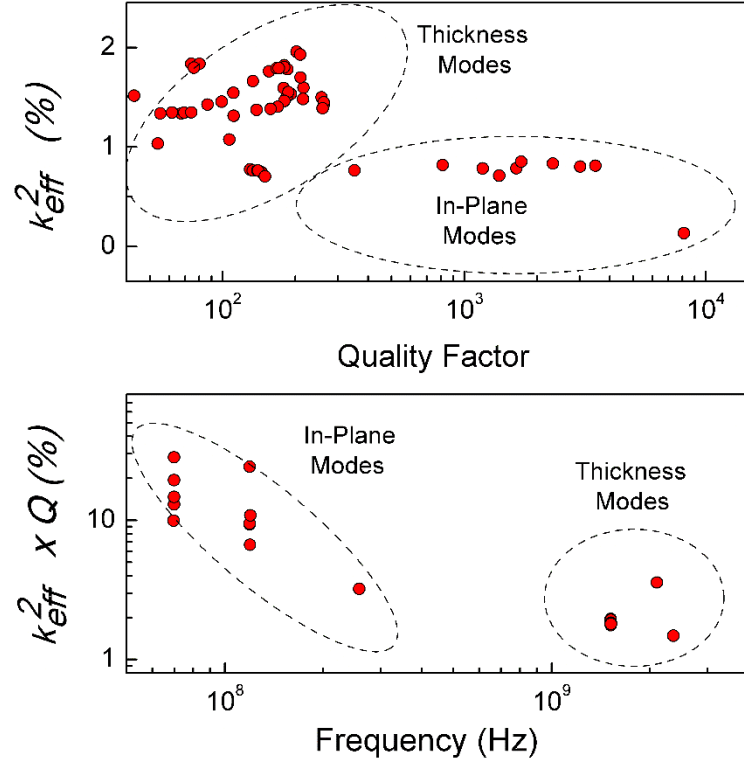


Fig. 3.6: Measured values of (a) k_{eff}^2 as a function of Q and (b) $k_{eff}^2 \times Q$ as a function of frequency. Data are consistent with published work by other researchers [64, 126, 127, 142].

3.4.3. Temperature Coefficient of Frequency

One of the important metrics for resonator performance is the TCF, which describes the relative shift in the resonator frequency with temperature change. As mentioned earlier, in most materials, the dominant mechanism is the change in the elastic modulus (TCE) of the material with respect to temperature. For the GaN resonators in this work, the TCF values for length-extensional modes range from -14 ppm/K to -18 ppm/K [64, 71, 77, 108]. TCF values ranging from -23 ppm/K to -25 ppm/K are reported for thickness-extensional modes. The TCF of the resonator is mode dependent and also is influenced by other materials in the resonating stack.

Representative plots of the TCF for two fabricated length-extensional resonators are shown in Fig. 3.7.

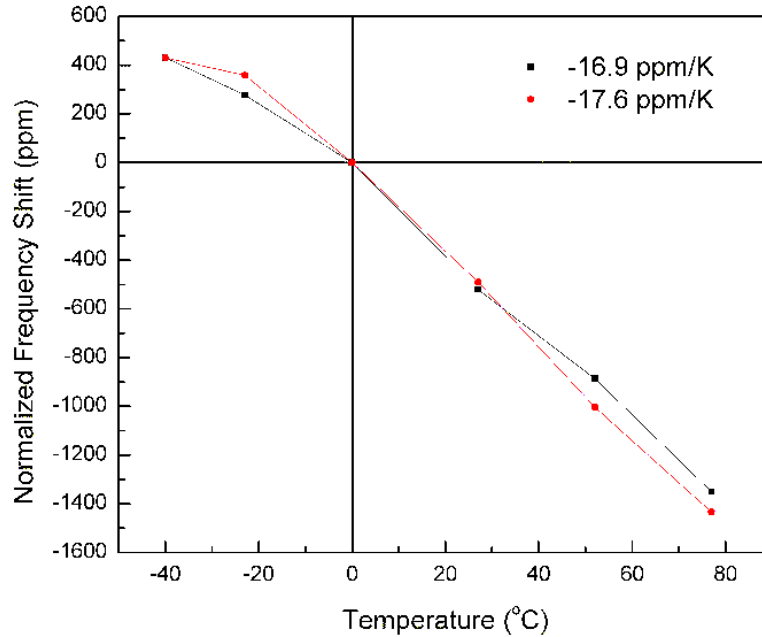


Fig. 3.7: The change in the frequency of two length-extensional GaN resonators as a function of temperature, showing a negative TCF with experimentally measured values of ~ -17 ppm/K.

3.4.4. Power Handling and IIP_3

The ability to handle high power levels has always been one of the most attractive features of GaN-based electronics. This has spurred the growth of a large power-electronics industry. Electromechanical devices, especially resonators, also have limiting values of input power that can be handled without distortion of the output due to the onset of electrical and mechanical non-linearity. In piezoelectric resonators, intrinsic mechanical non-linearity is primarily due to the non-linearity in the elastic coefficients of the material (especially for the suspension tethers) [129]. The non-linearity of the resonator is also limited by those of the supporting tethers. A popular

method for characterizing the non-linearity and distortion of mechanical resonators associated with high input power levels is the third order intercept point (IIP₃).

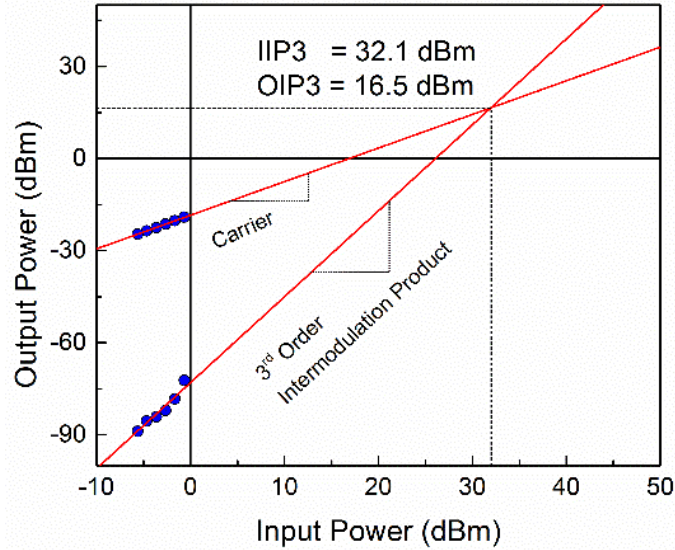


Fig. 3.8: Measured IIP₃ for a GaN mechanical resonator. The data are measured on a 2.1 GHz with a frequency separation of 5 KHz. The measured GaN bulk acoustic wave resonator shows Q of ~500.

For GaN length-extensional mode resonators with thin tethers, distortion is seen at +5 dBm or greater, while no distortion is seen for clamped membrane type thickness-mode resonators at input powers up to +20 dBm [64]. Extrapolated IIP₃ (Fig. 3.8) demonstrate values in excess of +32 dBm without requiring the use of thick Si structural layers in the device, a method that is used in the AlN-on-Si TPOS configuration [129]. These values are comparable with similar devices made using AlN [143].

Chapter 4 Phonon-Electron Interactions in Piezoelectric-Semiconductor BAW Resonators

The analytical and experimental work discussed in this chapter presents for the first time, a comprehensive investigation of phonon-electron interactions in BAW resonators made from piezoelectric semiconductor materials [24]. We show that these interactions constitute a significant energy loss mechanism and can set practical loss limits lower than anharmonic phonon scattering limits or thermoelastic damping limits. Secondly, we theoretically and experimentally demonstrate that phonon-electron interactions, under appropriate conditions, can result in a significant acoustic gain manifested as an improved Q .

The dynamics of acoustic waves (or phonons) trapped in resonant cavities comprised of solid elastic materials have been studied extensively [144]. At an appropriate frequency that satisfies the resonance criteria, mechanical energy is confined in the form of standing waves in such an elastic cavity. This principle forms the basis of BAW resonators [137, 144, 145]. While ideal standing wave BAW resonators are lossless, the energy confinement in practical materials is not ideal due to attenuation occurring via a number of phonon-scattering processes. This

attenuation limits the Q of such a BAW resonator. Analytical expressions for maximum Q limits for a variety of intrinsic scattering processes, such as anharmonic phonon-phonon loss and TED, are well known and experimentally validated for commonly used acoustic materials [25-28, 30, 31, 146]. An often neglected scattering process is the phonon-electron interaction [32-37, 147], which is significant in materials that have both moderate-to-high doping concentrations and a mechanism facilitating strong electromechanical interactions. Piezoelectric semiconductor materials such as ZnO, GaN, and CdS fulfill both criteria and as we will show in this chapter, the phonon-electron scattering can be the dominant loss mechanism in such materials. Similar to well-known lattice loss mechanisms such as the phonon-phonon loss, the phonon-electron scattering is dependent on the bulk material properties and is not design dependent. We show that phonon-electron interactions can lead to acoustic gain of standing waves in piezoelectric semiconductor BAW resonators and present, for the first time, a comprehensive model that explains the resulting enhanced mechanical Q of these resonators under the acoustoelectric effect [38, 39]. We evaluate the effect of phonon-electron interactions in piezoelectric semiconductor BAW resonators in context with other important acoustic loss mechanisms (such as anharmonic phonon loss and TED loss) by comparing the limiting figure of merit, the $f \times Q$ product, for each interaction mechanism. We compare theoretical estimates with measured results obtained using GaN BAW resonators as test vehicles. Measured data acquired on multiple BAW resonators with resonance frequencies ranging from 37 MHz to 8.7 GHz and fabricated using multiple wafers of single-

crystal wurtzite GaN are consistent with theoretical trends. We further explore the dependence of attenuation/amplification on factors such as charge carrier concentration, mobility, and resonance frequency. We show that it is practically possible to design piezoelectric semiconductor BAW resonators with (i) minimum phonon-electron scattering loss under normal operation, (ii) reduced total energy loss via acoustoelectric interaction, and (iii) acoustoelectric gain that can overcome all other losses, effectively creating a highly frequency-selective acoustoelectric resonant amplifier.

4.1. Theory of Acoustoelectric Amplification in Resonators

4.1.1. Standing Waves in Resonators

Acoustic waves travelling in a piezoelectric material cause local perturbations in the electric field in the material, as described by the basic piezoelectric constitutive equation $\mathbf{T} = c\mathbf{S} - e\mathbf{E}$. Here, \mathbf{T} , \mathbf{S} and \mathbf{E} are the local stress, strain, and electric field, while c and e are the stiffness coefficient and the piezoelectric coefficient, respectively. In a piezoelectric semiconductor material, the locally perturbed electric field causes the electrons to accumulate in the minima of the potentials of the waves, but as the wave progresses the electrons tend to lag behind [35]. This places more charge density in the electric field whose direction is that of wave propagation. This means that the average power transferred from acoustic phonons to electrons is positive, causing attenuation of the acoustic wave [33, 35, 36]. A large body of work [33-39] on phonon-electron interactions proved analytically and experimentally that

travelling acoustic waves in piezoelectric semiconductor materials suffer attenuation due to electron-scattering. The electrons gain energy and momentum, get accelerated in the direction of the acoustic wave, and appear as a net DC current in the material (Weinreich DC current [33]). It was observed that if electrons are accelerated by applying an external electric field across the material with velocities higher than the phonon velocity, energy can be transferred from the electrons to the phonons, effectively increasing the energy of the acoustic wave [35, 38, 39, 41]. This is referred to as acoustoelectric amplification and has been used to develop high-gain travelling-wave acoustic amplifiers [37].

We extend the existing analysis on acoustic amplification in travelling waves [33-39] to standing waves in BAW resonators, for the first time, and demonstrate that it is possible to generate acoustic gain in standing waves in piezoelectric semiconductor BAW resonators under the right conditions. We begin the analysis by solving for standing wave loss in a BAW resonator. Considering a real, elastic material of a finite thickness L , an acoustic wave travelling through this material will reflect back from the boundaries and remain confined in the material if the resonance condition $n\lambda = 2L$ is satisfied, where λ is the wavelength of the n^{th} vibration mode. This forms a cavity resonance and is the basic operational principle of BAW resonators [137, 144, 145]. The cavity resonance is a standing wave which is described as the superposition of two travelling waves with equal amplitudes and frequencies but opposite wave vectors [137]. Assuming plane acoustic waves, we can denote the standing wave in the BAW resonator as the superposition of the two waves (Fig. 4.1a).

$$u_{tot} = \mathbf{Re}[u_0 e^{i(\widetilde{k}_1 z + \omega t)} + u_0 e^{i(\widetilde{k}_2 z + \omega t)}] \quad \text{Eqn. 4.1}$$

$$\text{or} \quad u_{tot} = u_0 \cos(\widetilde{k}_1 z + \omega t) + u_0 \cos(\widetilde{k}_2 z + \omega t) \quad \text{Eqn. 4.2}$$

For ideal elastic materials, $\widetilde{k}_1 = k$ and $\widetilde{k}_2 = -k$ which gives

$$u_{tot} = 2u_0 \cos(\omega t) \cos(kz), \quad \text{Eqn. 4.3}$$

which is the equation for an ideal lossless standing wave in a resonant cavity. For a real, lossy material, the wave vectors are denoted by $\widetilde{k}_1 = k + i\alpha_1$ and $\widetilde{k}_2 = -k + i\alpha_2$ where the imaginary components are the loss coefficients per unit distance travelled. The loss α is composed of all distributed sources of acoustic loss in the bulk of the material, namely, losses due to phonon-phonon interaction (α^{pp}), thermoelastic damping (α^{TED}), and phonon-electron interaction (α^{pe}). At this point, we assume that the boundary reflection is perfectly lossless; reflection losses ($\alpha^{reflection}$) will be considered separately later. The superposition relation can be written as

$$u_{tot} = \mathbf{Re}[u_0 e^{-\alpha_1 z} \cdot e^{i(kz + \omega t)} + u_0 e^{-\alpha_2 z} \cdot e^{i(-kz + \omega t)}] \quad \text{Eqn. 4.4}$$

$$\text{or} \quad u_{tot} = u_0 e^{-\alpha_1 z} \cdot \cos(kz + \omega t) + u_0 e^{-\alpha_2 z} \cdot \cos(-kz + \omega t). \quad \text{Eqn. 4.5}$$

The above relation can be further simplified as

$$u_{tot} = A_1 \cos(\omega t) \cos(kz) - B_1 \sin(\omega t) \sin(kz), \quad \text{Eqn. 4.6}$$

$$\begin{aligned}
\text{where} \quad & A_1 = u_0[e^{-\alpha_1 z} + e^{-\alpha_2 z}] \\
& \text{Eqn. 4.7} \\
\& \quad & B_1 = u_0[e^{-\alpha_1 z} - e^{-\alpha_2 z}].
\end{aligned}$$

These equations predicts a pseudo-standing wave, which may have non-zero amplitude at the nodes if $B_1 \neq 0$. Most lossy resonant cavities are symmetric, *i.e.*, the attenuation in each direction is equal in magnitude, as it is a result of the fundamental, non-directional loss mechanisms of the material. That is $\alpha_1 = \alpha_2 \equiv \alpha$. Consequently, $B_1 = 0$ and $A_1 = 2u_0[e^{-\alpha z}]$. This recovers the expression for a real, damped resonant cavity, which is the most commonly encountered practical situation (Fig. 4.1(b)):

$$u_{tot} = 2u_0[e^{-\alpha z}]\cos(\omega t)\cos(kz). \quad \text{Eqn. 4.8}$$

The possible responses for such a standing-wave BAW resonator depend on the nature of α . Fig. 4.1((b) and Fig. 4.1((c) depict possible scenarios of damped, undamped (ideal) and amplified BAW resonators ($\alpha > 0$, $\alpha = 0$, and $\alpha < 0$ respectively). The possibility of an amplified response with an additional external stimulus is a unique attribute of piezoelectric semiconductor materials and is detailed in further discussion. In the case of a non-symmetric interaction mechanism, where the attenuation is direction-dependent (*i.e.*, $\alpha_1 \neq \alpha_2$), Eqn. 4.6 must be considered in its entirety. We can simplify the amplitude coefficients (Eqn. 4.7) by expanding them in a Taylor series and neglecting higher powers of αz , to get

$$A_1 \approx u_0[2 - (\alpha_1 + \alpha_2)z] \quad \text{Eqn. 4.9}$$

$$\& \quad B_1 \approx u_0(\alpha_1 - \alpha_2)z.$$

For practical values of attenuation $A_1 \gg B_1$ and thus we can neglect the term $B_1 \sin(\omega t) \sin(kz)$. This assumption is valid as long as $\alpha_1 z \ll 1$ & $\alpha_2 z \ll 1$ and we can consider the lossy standing wave to be

$$u_{tot} \approx A_1 \cos(\omega t) \cos(kz), \quad \text{Eqn. 4.10}$$

$$\text{where} \quad A_1 \approx 2u_0[1 - (\alpha_{SW})z]. \quad \text{Eqn. 4.11}$$

The assumption $\alpha_1 z \ll 1$ & $\alpha_2 z \ll 1$ is valid for any BAW resonator made with a high-quality thin-film elastic material. As an example, for a high-quality GaN film and in the absence of an external electric field, the value of α_1^{pe} and α_2^{pe} is $\sim 2500 \text{ m}^{-1}$ at 1.5 GHz, or an energy loss of 0.25% per micrometer of the GaN film. We define net roundtrip attenuation per unit length for the standing wave BAW resonator as,

$$\alpha_{SW} \equiv \frac{\alpha_1 + \alpha_2}{2}. \quad \text{Eqn. 4.12}$$

Other distributed losses in the material of the BAW resonator (the phonon-phonon and TED losses) are symmetric, *i.e.*, $\alpha_1 = \alpha_2$. Again, this directly implies $B_1 = 0$, resulting in a lossy standing wave. For phonon-electron interaction in piezoelectric semiconductor materials, upon application of a DC electric field, there is a net drift of electrons in one direction. Based on the directional nature of the interaction between coherent phonons and electrons, the uni-directional drift of the electrons breaks the symmetry of attenuation, and thus $\alpha_1^{pe} \neq \alpha_2^{pe}$. Using Eqn. 4.12 and the

equations for attenuation coefficients in travelling waves from the theory put forward by Hutson and White [39, 41], we can write effective attenuation due to phonon-electron interaction for the standing wave as

$$\alpha_{Piezo}^{pe} = \frac{K^2 \omega_c}{4s} \left\{ \frac{1-\eta}{(1-\eta)^2 + b^2} + \frac{1+\eta}{(1+\eta)^2 + b^2} \right\}, \quad \text{Eqn. 4.13}$$

where

$$b = \left(\frac{\omega_c}{\omega} + \frac{\omega}{\omega_D} \right), \quad \text{Eqn. 4.14}$$

$$\eta = \left| \frac{v_e}{s} \right| = \left| \frac{\mu E_D}{s} \right|, \quad \text{Eqn. 4.15}$$

$$\omega_c = \frac{\sigma}{\epsilon} = \frac{q_e \mu N}{\epsilon}, \quad \& \quad \omega_D = \frac{s^2 q_e}{\mu k_B T}. \quad \text{Eqn. 4.16}$$

A complete derivation of the attenuation coefficient for travelling waves is provided in Appendix A. In the above relations, K is the piezoelectric coupling coefficient, μ is the electron mobility, N is the effective free electron concentration, E_D is the applied DC electric field, v_e is the electron drift velocity, s is the acoustic velocity, η is the velocity ratio, ω_c is the carrier relaxation frequency, and ω_D is the carrier diffusion frequency. The electrical conductivity, permittivity, electronic charge, absolute temperature and Boltzmann's constant are denoted by the usual symbols σ, ϵ, q_e, T , and k_B , respectively. Eqn. 4.13 agrees with observations of Maines and Paige [148]. Note that without applied bias, $\eta = 0$, and Eqn. 4.13 reduces to the symmetric situation denoting the nominal loss due to phonon-electron interaction with piezoelectric coupling

$$\alpha_1 = \alpha_2 = \alpha_{piezo}^{pe} \Big|_{\eta=0} = \frac{K^2}{2S} \frac{\omega_c}{1 + b^2}. \quad \text{Eqn. 4.17}$$

Eqn. 4.13 can be physically interpreted to be the combination of the phonon-electron interaction for the travelling-wave components parallel and anti-parallel to the direction of carrier drift. Based on the theory of acoustoelectric amplification in travelling waves [35-39, 41], when the carrier drift velocity exceeds the acoustic velocity, the parallel wave component is amplified by transfer of energy from electrons to phonons, while the anti-parallel wave component is attenuated by electron-scattering. When an adequate electric field is applied to the BAW resonator and the parallel gain exceeds anti-parallel loss, α_{piezo}^{pe} can become negative, denoting net gain over the roundtrip. This is the theoretical basis for achieving a net acoustic gain in a standing wave piezoelectric semiconductor BAW resonator. Unlike the travelling wave model [39, 41], α_{piezo}^{pe} is symmetric with respect to the direction of applied electric field. Further, the acoustoelectric amplification in BAW resonators can be practically observed only for those modes that fulfill the resonance condition $n\lambda = 2L$. This imparts frequency selectivity to the standing wave model in BAW resonators that is unique to it and differentiates it from the travelling wave model.

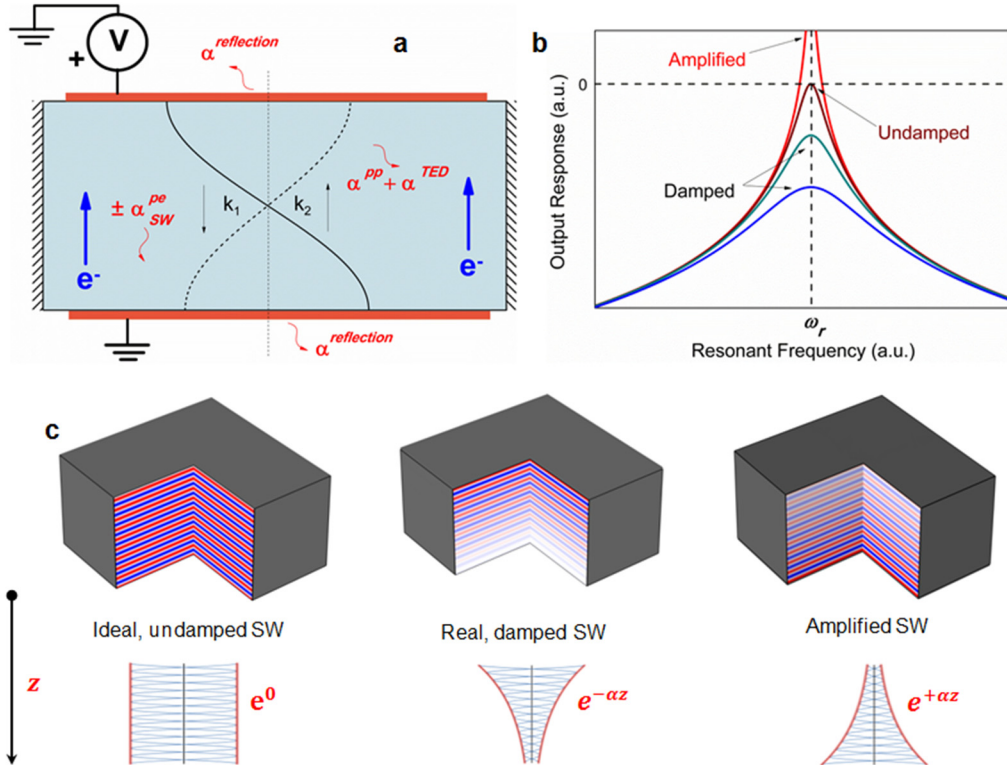


Fig. 4.1 : (a) Schematic cross-section of a piezoelectric semiconductor BAW resonator, depicting the fundamental thickness mode of vibration. The schematic indicates the various intrinsic loss mechanisms (phonon-phonon scattering, TED and phonon-electron scattering) in addition to the reflection losses. In the absence of other external losses, such as air damping, the total energy loss per cycle is dominated by these loss mechanisms. For a piezoelectric semiconductor material, under the right conditions, the phonon-electron scattering losses can be inverted to achieve acoustoelectric gain. (b) A representative set of output responses for BAW resonators, denoting damped, undamped, and amplified responses ($\alpha > 0$, $\alpha = 0$, and $\alpha < 0$ respectively). (c) The same responses can be visualized by the strain distribution of BAW resonator cross-sections under ideal, damped and amplified conditions ($\alpha > 0$, $\alpha = 0$, and $\alpha < 0$ respectively). The cross-section images show higher order standing wave BAW resonance modes, and visually exaggerated damping/amplification envelopes for clarity of concept. The color map shows areas of positive (red) and negative (blue) strain.

4.1.2. Frequency Dependence of Gain and Loss

The curves for α_{piezo}^{pe} as a function of frequency and η can be obtained using Eqn. 4.13 for wurtzite GaN (Fig. 4.2(a)). Here, an effective carrier concentration of 10^{15} cm^{-3} , a carrier mobility of $200 \text{ cm}^2/\text{V-s}$, an acoustic velocity of 8000 m/s , and a coupling coefficient of 2% are assumed. Other relevant material properties are given in Table 4.I.

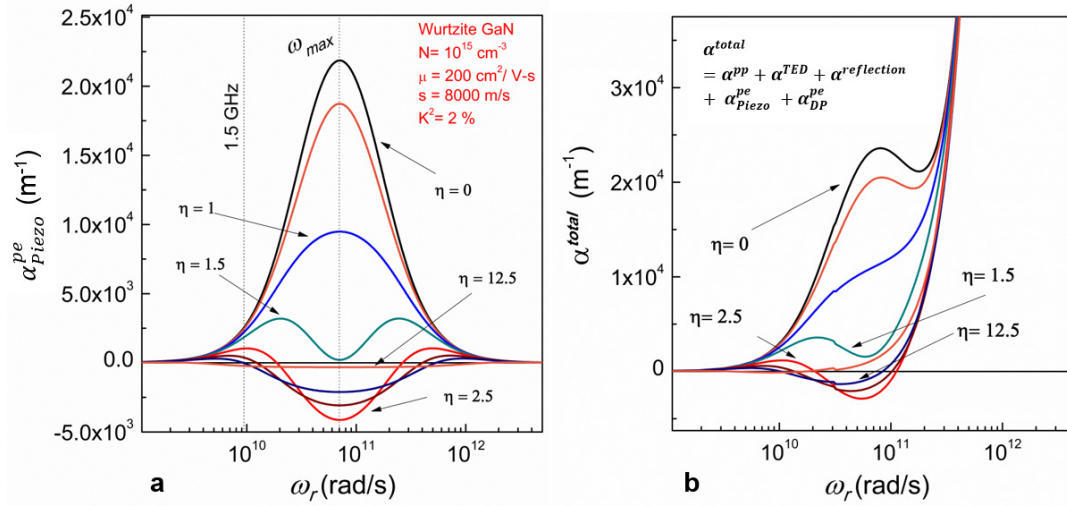


Fig. 4.2 : (a) The phonon-electron loss/gain in a representative GaN material system with respect to resonant frequency and the velocity ratio η . Increasing the applied electric field (and thus η) reduces the phonon-electron loss across all frequencies. Here, $\eta = 0, 1, 2, \dots$ correspond to electric field values $E_D = 0$ kV/m, 400 kV/m, 800 kV/m ... as per Eqn. 4.15. Within a certain range of η , the phonon-electron loss is negative, indicating acoustic gain. (b) The total loss in the system is clearly affected by phonon-phonon loss and thermoelastic damping, but still includes regions where loss is negative predicting the possibility of acoustoelectric amplification in the resonator that can theoretically overcome all other intrinsic losses in the material. Note that this is the frequency dependence loss for the piezoelectric semiconductor material, not the resonator. The mechanics of the BAW resonator itself imposes further frequency selectivity, allowing only those modes that conform to the resonance condition $n\lambda = 2L$.

Table 4.I
Material Properties used for Calculating Loss Components in GaN

Material Property	Symbol	Values	Units	Ref.
Mass Density	ρ	6150	kg/m ³	[138]
Specific Heat	C_s	490	J/kg-K	[138]
Phonon Relaxation Time	τ	2.02×10^{-12}	s	-
Thermal Conductivity	κ	130	W/m-K	[138]
Coefficient of linear Expansion	β	5.6×10^{-6}	K ⁻¹	[138]
Acoustic Velocity	s	8000	m/s	[138]
Grüneisen Parameter	γ	1.18	-	[149]
Deformation Potential Constant	Ξ	12	eV	[150, 151]
Intervalley Relaxation Time	τ_R	1.2×10^{-12}	s	[152]

In addition to the frequency selectivity imposed by the mechanical resonance condition and the resonator dimensions, the phonon-electron interaction itself has

strong frequency dependence (Fig. 4.2(a)). The maximum interaction of phonons and electrons is observed at the geometric mean of ω_c and ω_D ($\omega_{max} = \sqrt{\omega_c \cdot \omega_D}$). At ω_{max} , and without DC bias, the nominal α_{piezo}^{pe} is at its peak value corresponding to the maximum acoustic loss due to electron-scattering. However, the acoustic gain is also maximum at ω_{max} when a sufficiently large E_D is applied to the GaN film. With increasing η , the acoustic loss decreases. Above a threshold velocity ratio (η_{th}), α_{piezo}^{pe} becomes negative, indicating a crossover into the gain regime. The highest gain is seen for ω_{max} ; but it is also possible to achieve acoustic gain at lower frequencies. This is a significant finding as it relaxes the design frequency range for resonators. The frequency of highest gain, ω_{max} tends to be high (~ 10 GHz or higher for most piezoelectric semiconductor materials). This result indicates that it is possible to boost the Q electrically with resonators operating in the VHF/UHF ranges. In fact, given the high nominal values of loss at ω_{max} , it may be practically more useful to choose a frequency at which the original loss is small and yet obtain a relatively large improvement in Q with increasing E_D . Alternately, it is possible to design for lower values of ω_{max} by careful selection of N in the material, within reason ($\omega_{max} \propto \sqrt{N}$). This enables higher amplification ratios at lower frequencies. The dependence of the interaction on material properties is detailed in the proceeding sections.

4.1.3. Other Loss Mechanisms in Piezoelectric Semiconductor BAW

Resonators

The anharmonic phonon-phonon loss due to inelastic interaction of the acoustic wave with the lattice phonons can be expressed as [26]:

$$\begin{array}{l} \text{for } \omega\tau < 1 \\ \text{Akhieser Regime} \end{array} \quad \alpha^{pp} = \frac{C_v T \gamma^2 \tau}{2\rho s^3} \left(\frac{\omega^2}{1 + \omega^2 \tau^2} \right) \quad \text{Eqn. 4.18}$$

And

$$\begin{array}{l} \text{for } \omega\tau > 1 \\ \text{Landau-Rumer Regime} \end{array} \quad \alpha^{pp} = \frac{\pi^5 \gamma^2 K_b^4 T^4}{30\rho s^6 h^3} \omega \quad \text{Eqn. 4.19}$$

The two regimes for phonon-phonon loss depend on whether one can consider the lattice to be interacting with phonon ensembles or individual phonons and are distinguished by the relation between the frequency and the phonon relaxation time τ . The phonon relaxation time can be calculated [26] from the equation:

$$\tau = \frac{3\kappa}{C_v s^2} \quad \text{Eqn. 4.20}$$

TED loss is due to the volume changes during vibrational motion that cause loss of energy as a result of the heat flow in the material. For longitudinal ‘bar’ resonators, operating at VHF/UHF frequencies with adiabatic vibration, the TED loss can be approximated to be [26]:

$$\alpha^{TED} = \frac{\kappa T \beta^2 \rho}{18 C_v^2 s} \omega^2 \quad \text{Eqn. 4.21}$$

Note that different values will apply for TED loss in flexural resonators and for purely shear mode resonators with isochoric vibration, there is ideally no TED loss. The reflection loss or interface loss is defined as the energy lost by the resonator through its tethers or through the air-interface surrounding it, as a consequence of non-ideal boundary conditions. This is not strictly a distributed bulk material loss; however, we model it as such for the purposes of fitting. Analytical solutions are difficult to achieve except for the simplest of situations, and so we use ξ and r as the fractions of energy lost and retained, respectively, per cycle of operation. $\xi + r = 1$. For the perfect resonant cavity of length L , $n\lambda = 2L$, $r = 1$, which implies perfect reflection and no loss at the material interface. For a real resonator, the presented model uses ξ as an independent parameter, ranging from 0.0001 to 0.01 to achieve a reasonable fit between the measured and modeled Q_m . The reflection loss coefficient is defined as [148]:

$$\alpha^{reflection} = -\frac{1}{L} \ln\{r(\omega)\} \quad \text{Eqn. 4.22}$$

Phonon-electron interactions due to deformation potential (DP) coupling occur in all semiconductors [35] due to the perturbations of the conduction band due to lattice strain caused by phonons. The loss can be expressed as

$$\alpha_{DP}^{pe} = \frac{N\Xi^2}{9s^4 k_B T \rho} \frac{\omega^2 \tau_R (1 - \eta)}{1 + (1 - \eta)^2 \omega^2 \tau_R^2} \quad \text{Eqn. 4.23}$$

where Ξ is the deformation potential constant, and τ_R is the relaxation time for intervalley transitions. In general, DP coupling is significantly smaller than

piezoelectric coupling for low to moderate doped piezoelectric semiconductor materials. DP coupling is the dominant phonon-electron interaction mechanism for non-piezoelectric semiconductors and semi-metals. A comparison for the calculated values of piezoelectric and DP coupling [150, 151] for GaN confirms the dominance of piezoelectric coupling. The values for the various loss components in GaN are calculated using material properties from existing literature [138, 149-152].

4.1.4. Influence on Total Intrinsic Q

For practical piezoelectric semiconductor BAW resonators, α_{Piezo}^{pe} needs to be seen in context with all other loss mechanisms. The total loss can be written as the sum of all contributing intrinsic and extrinsic loss mechanisms. Note that α_{Piezo}^{pe} can be positive (attenuation) or negative (gain), but for other loss mechanisms $\alpha > 0$.

$$\alpha^{total} = \alpha^{pp} + \alpha^{TED} + \alpha^{reflection} + \alpha_{DP}^{pe} + \alpha_{Piezo}^{pe} \quad \text{Eqn. 4.24}$$

The mechanical Q of the resonator is defined as the ratio of the energy conserved to the energy dissipated per cycle of operation [26, 137, 144] and is given by

$$Q_i^{total} = \frac{\omega}{2s\alpha^{total}} \quad \text{Eqn. 4.25}$$

We neglect other extrinsic factors, such as air damping that can be eliminated by good resonator design or by operation in vacuum. The phonon-phonon loss and the TED loss have been explored in detail [30, 153] and are generally considered to be the ultimate limiting factors for the Q of mechanical resonators with low-doped or dielectric materials [30, 31, 146]. The reflection losses include all interfacial losses

from the body of the resonator to the surrounding media, inclusive of the loss through the supporting tethers. An important distinction between the travelling-wave amplifier and the amplified resonator arises from the selectivity afforded by $\alpha^{reflection}$. The reflection loss is low at resonance, and extremely high at other wavelengths that do not fulfill the resonance condition mentioned earlier. The loss due to deformation-potential coupling (α_{DP}^{pe}) is another phonon-electron interaction mechanism that is present in all semiconductors but only becomes significant at high or degenerate doping. The total phonon-electron loss/gain for wurtzite GaN as a function of frequency and η is shown in Fig. 4.2(b). It is seen that total loss is still lowered with increased E_D , and it is theoretically possible for the phonon-electron gain to overcome other loss mechanisms ($\alpha^{total} < 0$) under the right conditions.

4.1.5. Limiting Values of $f \times Q$ product

Fig. 4.3 compares the limits set by the phonon-electron interaction due to piezoelectric coupling with other limiting values for GaN (Fig. 4.3(a)). As discussed, the electromechanical interactions can be of two types: piezoelectric coupling or deformation-potential coupling. Loss due to piezoelectric interaction is given by Eqn. 4.13 and the loss due to deformation-potential coupling is given by Eqn. 4.24. Fig. 4.3(b) describes the non-monotonic dependence of the $f \times Q$ limit for phonon-electron interactions as a function of N for a particular frequency (here, 1.5 GHz). It is seen that in the moderately doped GaN, the phonon-electron loss is more significant (higher) than losses due to other mechanisms. By the same logic,

significant acoustoelectric gain is only possible for moderately doped GaN. In lightly doped piezoelectric semiconductor materials, the interaction between acoustic wave and charge carriers is limited due to the low density of charge carriers, leading to low phonon-electron loss and consequently a high limiting value of $f \times Q_{Piezo}^{pe}$. This tends towards the dielectric model, where phonon-electron losses are insignificant. As N increases to a highly-doped level, the piezoelectric interaction is screened, leading to lower phonon-electron loss due to piezoelectric coupling and again a high limiting value of $f \times Q_{Piezo}^{pe}$. At extremely high doping levels, the material behaves similar to a metal, where acoustic loss occurs due to interaction of phonons and the free-electron gas, described by a different model [26]. For the range of doping from unintentionally doped [154, 155] to highly doped bulk GaN ($10^{15} \text{ cm}^{-3} < N < 10^{19} \text{ cm}^{-3}$) the $f \times Q$ limits for both phonon-electron interaction mechanisms are depicted in Fig. 4.3(c) and Fig. 4.3(d). The limiting value set by the piezoelectric coupling portion of the phonon-electron loss is most relevant for low to moderately doped piezoelectric semiconductor resonators. In this range, limits set by the phonon-electron interaction are lower than other intrinsic loss mechanisms and are thus the dominant limiting factors. In contrast, for highly doped or degenerately doped semiconductors ($N > \sim 10^{18} \text{ cm}^{-3}$), α_{DP}^{pe} becomes the significant factor. For non-piezoelectric semiconductors, deformation-potential coupling is the only form of phonon-electron interaction.

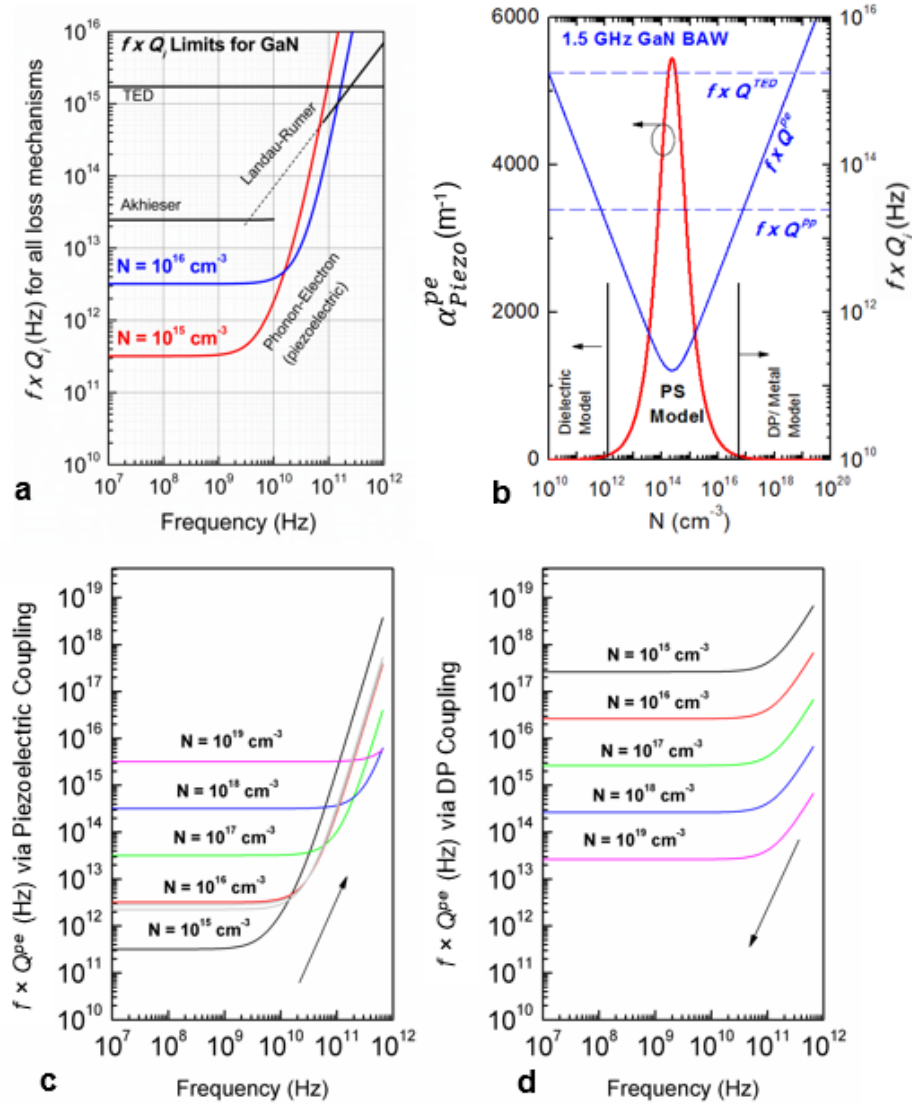


Fig. 4.3 : (a) The $f \times Q$ limits for the various intrinsic loss mechanisms in piezoelectric semiconductor GaN ($f = \omega/2\pi$). For low to moderately doped piezoelectric semiconductor GaN, the phonon-electron mechanism is the significant limiting factor, lower than the anharmonic phonon-scattering and TED. (b) For a representative frequency, (here, 1.5 GHz), the piezoelectrically coupled model for phonon-electron interaction is significant only for a range of values of moderate doping. Beyond this range, other interactions dominate. The $f \times Q$ limit due to phonon-electron interaction is highly dependent on the effective electron concentration. Two important mechanisms of phonon-electron interaction are (c) piezoelectric and (d) deformation-potential (DP) coupling. At low to moderate doping, the piezoelectric interaction dominates, and the two loss mechanisms achieve parity only at a concentration of $\sim 1 \times 10^{18} \text{ cm}^{-3}$ for GaN.

4.2. Experimental Findings

4.2.1. Fabrication

The BAW resonators are fabricated from wurtzite UID GaN grown by MOCVD (Wafers A, C, and D, acquired from Nitronex Corp. NC, USA), or by MBE (Wafer B, acquired from SOITEC, Bernin, France). Neither type of GaN film has the GaN/AlGaN strained interface that is used to achieve the high sheet conductivity known as the 2D electron gas (2DEG). Both types of films are thus bulk GaN, with unintentional (low) n-type doping and low mobility. The fabrication process is described in Chapter 2.

4.2.2. Measurement Procedures and Controls

The RF scattering parameters of the resonators were measured using an Agilent N5241A or an Agilent E5061 network analyzer, Cascade ACP RF probes in the Ground-Signal-Ground (GSG) configuration, with 50Ω terminations. Short-open-load-through (SOLT) calibration was performed to remove the effect of the cables and probe parasitics. DC bias is applied to the RF electrodes using bias tees. The two-port devices are fully symmetric with respect to choice of port for RF or DC stimulus.

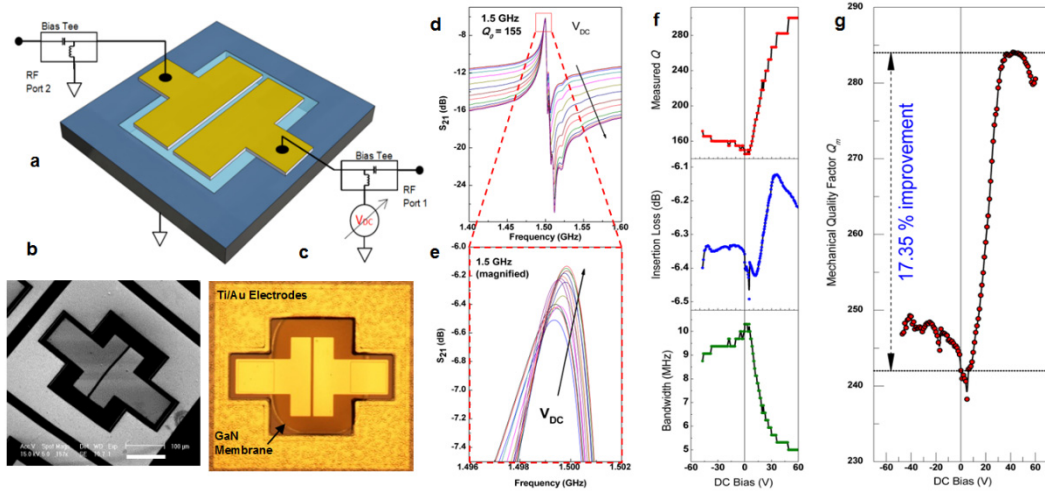


Fig. 4.4 : (a) A schematic of a two-port thin film BAW resonator made from epitaxially grown GaN. The resonator is normally driven using only an RF stimulus, but a DC bias applied across the resonant cavity causes a change in the performance. The resonator is seen in (b) a SEM and (c) a microscope image that shows the edge of the released GaN membrane. Scale bar corresponds to 100 μm . (d-e) RF transmission measurements (S_{21}) of the resonator with indicating both nominal operation and the evolution of BAW resonator performance improvement with an increasing DC bias. (f) This improvement can be quantified by the improved IL, decreased bandwidth, and consequently increased Q . (g) The extracted mechanical Q , Q_m , which is free of all parasitic effects. Q_m shows significant improvement with applied DC, demonstrating that there is a fundamental reduction in internal loss and consequently an improvement in the energy confinement in the BAW resonator.

The measurements are performed with the devices in a cryogenic-capable, temperature controlled vacuum probe station (Lakeshore TTPX). Temperature of the sample stage and surrounding chamber walls is synchronously monitored and maintained at 300 K (except for the thermal testing) and monitored to within ± 10 mK. Devices are measured at vacuum levels under 20 μTorr . Upper limits of RF input and DC excitation are maintained below the onset of resonator non-linearity or mechanical breakdown of the devices.

Fig. 4.4(a) - Fig. 4.4(c) show a schematic and images for a BAW resonator operating in the fundamental thickness extensional mode. Normal RF performance is measured using a network analyzer, and increasing DC bias is applied between the

two ports using bias tees. The DC bias causes a marked change in the performance of the device (Fig. 4.4(d)-Fig. 4.4(e)). This change in performance can be quantified by the simultaneous improvement of the Q , lowering of the IL, and narrowing of the resonance bandwidth (Fig. 4.4(f)). At the same time, the off-resonance transmission decreases. The decrease in the transmission level is the result of current saturation that accompanies acoustoelectric amplification [156]. The net effect of these changes is an improvement in the resonator transfer-function or a selective amplification of the energy confined in the primary resonance mode. It is to be noted that selective improvement at resonance and decrease in the off-resonance transmission distinguishes this phenomenon from a simple shift in the transmission response that can be achieved using GaN/AlGaIn high electron mobility transistors (HEMTs) in conjunction with the resonator [142, 157]. While the electrical contacts used in this work are non-ohmic, the non-linear nature of the contacts cannot explain the selective improvement of the transmission response at resonance.

To illustrate the improvement in the purely mechanical performance of the device, electrical losses and parasitic effects are de-embedded and the mechanical (or unloaded) quality factor (Q_m) (Fig. 4.4(g)) along with the motional resistance (R_m) of the device are extracted (Section 4.2.3 and Section 4.2.4). The Q_m shows clear improvement ($\sim 17.35\%$ for this particular resonator) upon application of a DC bias, indicating that mechanical performance enhancement is significant.

4.2.3. Analytical Extraction of Q_m

The Q_m of a piezoelectric resonator can be calculated analytically by considering the lumped model of a single electroded region of the resonators and by using the relation

$$Q_m = \frac{\sqrt{km_{eff}}}{nR_m\zeta^2} = \frac{\omega m_{eff}}{nR_m\zeta^2} \quad \text{Eqn. 4.26}$$

This reduces to the relation between Q_m and motional resistance (R_m)

$$Q_m R_m = \frac{\omega m_{eff}}{n\zeta_{ij}^2} \quad \text{Eqn. 4.27}$$

This can be further simplified by using the relations

$$m_{eff} = \rho w l t / 2 \quad \text{Eqn. 4.28}$$

$$k_{33} = \frac{c_{33} w t}{l} \quad ; \quad k_{11} = \frac{c_{11} l t}{w}, \quad \text{Eqn. 4.29}$$

$$\zeta_{33} = \frac{2e_{33} w l}{t} \quad ; \quad \zeta_{31} = 2e_{31} w, \quad \text{Eqn. 4.30}$$

where ζ_{ij} is the electromechanical coupling coefficient (N/V), and n is the number of elemental resonators present in the entire device. The motional resistance (R_m) is the lumped representation of all the acoustic or mechanical losses in the system. The mass and the stiffness of the resonating element are described by the motional inductance (L_m) and motional capacitance (C_m), respectively, which are given by:

$$L_m = \frac{m_{eff}}{\zeta_{ij}^2} \quad ; \quad C_m = \frac{\zeta_{ij}^2}{\omega^2 m_{eff}} \quad \text{Eqn. 4.31}$$

The value of R_m can be extracted from the electrical impedance of the measured data, after considering the effect of electrical feedthrough and the parasitic capacitances originating in the device and contact pads.

For piezoelectric resonators, the only effective methods used for lowering R_m require optimization of the resonator geometry, electrode materials and dimensions, or the electrical/mechanical matching conditions [158]. Prior work on BAW resonators has focused on exhaustive analysis [147], low-loss designs [159], or improvement of material [160] and structural composition [77] to improve the Q . None of these improvements are dynamic in nature. It is seen in the current work that the values of R_m for the GaN resonators decrease significantly (up to 35% reduction), simply by applying a DC bias, indicating a reduction in the mechanical losses incurred. The improvement is dynamic, repeatable and reversible.

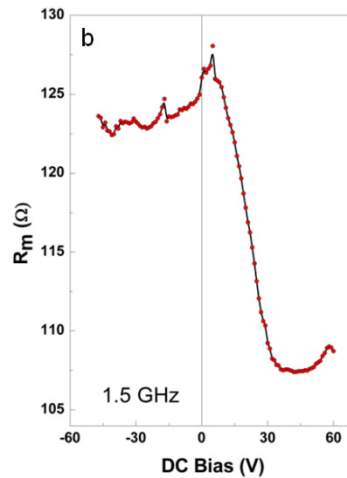


Fig. 4.5 : The values of R_m extracted from the measured data for the BAW device shown in Fig. 4.4. The values of Q_m are based on these extracted values.

4.2.4. Equivalent Electrical Model Fitting

The equivalent electrical model provides another corroborative indicator that R_m decreases with the applied electrical bias when all electrical parasitics are de-embedded. The exact values of the parasitics are calculated using the known dimensions of the GaN film and electrodes, and standard material properties of GaN [138].

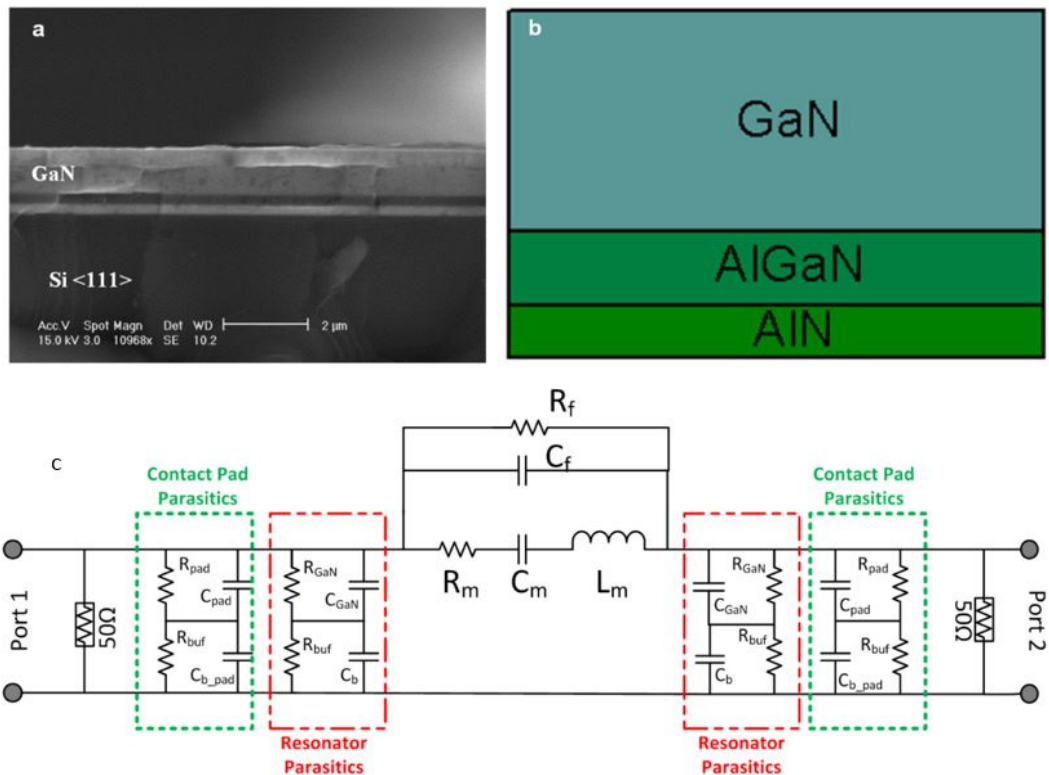


Fig. 4.6 : (a) Cross section electron micrograph of a GaN film epitaxially grown on a Si (111) wafer. (b) In order to mitigate the lattice mismatch between GaN and Si, a graded buffer layer consisting of AlN and AlGaN layers is used. (c) A modified version of the two-port Butterworth-van Dyke (BVD) model of a resonator can be used to map mechanical quantities with their equivalent motional quantities. The parasitic effect of the buffer layers associated with the body of the resonator and the contact pads has been included for a more accurate fit. The model is symmetric with respect to its ports.

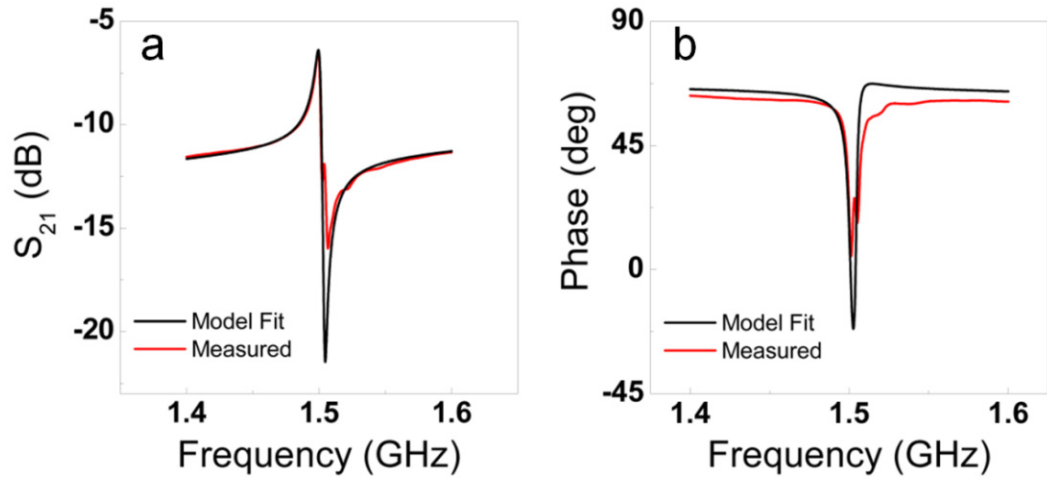


Fig. 4.7 : BVD model fit for the RF transmission magnitude and phase of the 1.5 GHz resonator shown in this work. It can be seen that the model provides an accurate match with measured RF transmission parameters. The lumped element values for the 1.5 GHz device used for this fitting are shown in Table 4.II. The transmission response of the resonator at each value of DC bias can be matched using the BVD model and corroborates the lowering of R_m . The value of R_m for this resonator at varying DC bias is shown in Fig. 4.5

Table 4.II
Dimensions and Material Properties for the 1.5 GHz resonator

Material Properties							
Resistivity	GaN	0.0446	Ω -m	Relative Permittivity	GaN	8.9	-
	AlGaN	-	Ω -m		AlGaN	8.8	-
	AlN	-	Ω -m		AlN	8.5	-
Dimensions							
Film Thickness	GaN	1800	nm	In-plane Dimensions	L	130	μ m
	AlGaN	250	nm		W	40	μ m
	AlN	250	nm		L_{pad}	80	μ m
					W_{pad}	80	μ m
Parasitic Effects							
Resonator Parasitics	$C_{pad}(GaN)$	40	fF	Pad Parasitics	$C_{pad}(GaN)$	40	fF
	$R(GaN)$	650	Ω		$R_{pad}(GaN)$	600	Ω
	C_b (AlGaN/AlN)	360	fF		C_{b_pad} (AlGaN/AlN)	300	fF
	R_{buf} (AlGaN/AlN)	$>10^{12}$ (~open)	Ω		R_{buf} (AlGaN/AlN)	$>10^{12}$ (~open)	Ω
Electrical Feedthrough							
Capacitance	C_f	374	fF	Resistance	R_f	17	k Ω
Motional Parameters							
Motional Capacitance	C_m	1.875	fF	Motional Inductance	L_m	6	μ H

4.3. Comparison of Experimental Data and Models

The analytically modeled values for Q_i^{total} are compared to the measured values for Q_m for the piezoelectric semiconductor BAW resonators. α_{piezo}^{pe} is the only parameter that is dependent on applied E_D , and follows the trends shown in Fig. 4.2. All loss mechanisms except $\alpha^{reflection}$ are calculated as discussed in Section 4.1. $\alpha^{reflection}$ is used as a fitting parameter to equate the nominal values of Q_i^{total} and measured Q_m . Representative comparisons of piezoelectric semiconductor BAW resonators from each wafer are shown in Fig. 4.8. The most critical parameters for achieving comparable trends are the resonant frequency and the effective electron concentration N . Unless otherwise noted, the values of μ and K^2 used in the calculations are $200 \text{ cm}^2/\text{V}\cdot\text{s}$ and 2 % respectively. All modeled values are for a temperature of 300 K. Resonators from the same wafer expectedly have the same values for N . For Wafers A and B respectively, the best comparison of N values are $1 \times 10^{15} \text{ cm}^{-3}$ and $7 \times 10^{15} \text{ cm}^{-3}$ respectively. For Wafer C, the amplification is low, and we use averaged data sets. The estimated value of N for Wafer C is $(8 \pm 2) \times 10^{15} \text{ cm}^{-3}$. The gain saturation in Wafer C could be a result of higher trap density in GaN, non-linear response due to joule heating from DC current, or a combination of these effects. The high initial Q_m and the low amplification are as expected for a wafer with high doping. An accurate quantitative fit between modeled values and measured results is not attempted at this point due to the large number of parameters involved in the loss component calculations, the large range of values for these parameters, and

the fact that these values are derived from different sources in literature. Measured $f \times Q$ values are consistent with modeled $f \times Q$ limits (Fig. 4.9).

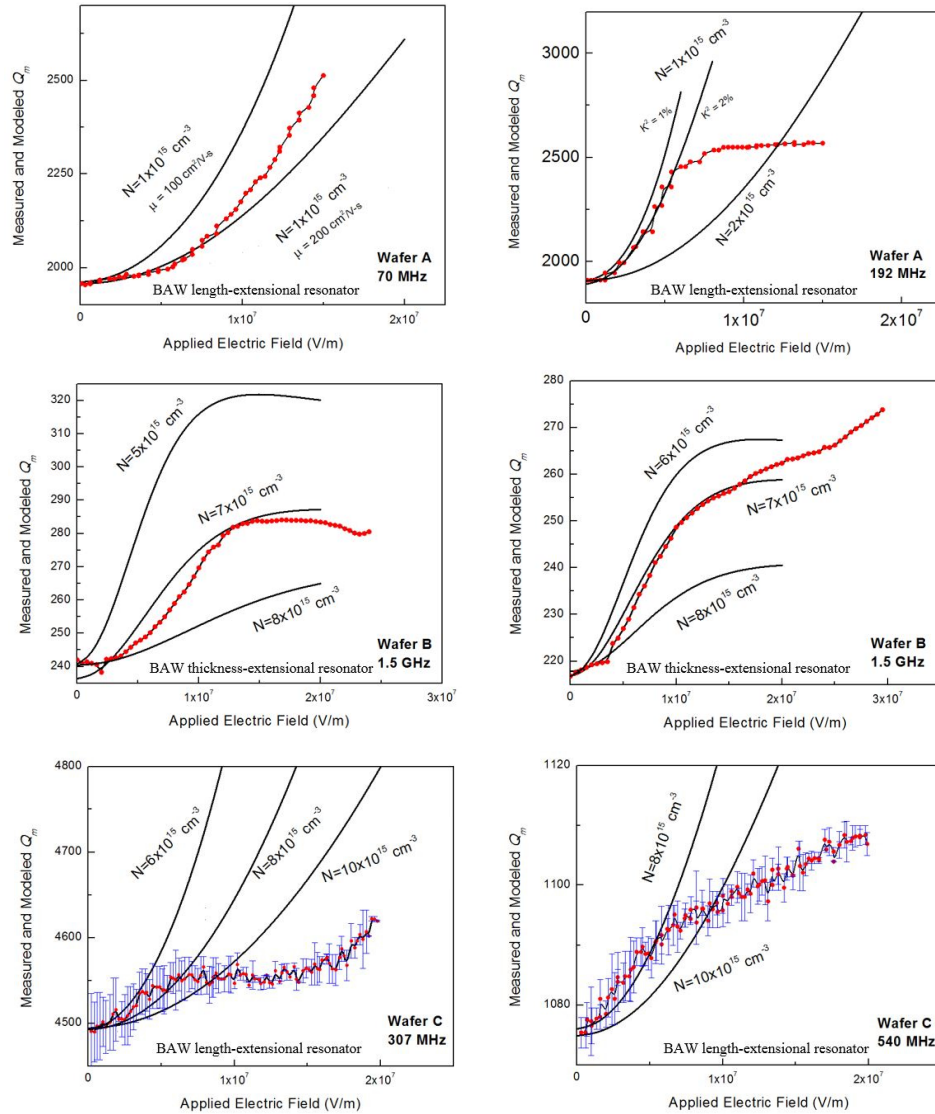


Fig. 4.8 : Qualitative comparison of the improvement in Q_m for representative resonators on multiple wafers, using the full intrinsic loss model. Approximate estimates for the effective electron concentrations of each wafer are determined using this comparison. Error bars for Wafer C denote the maximum/minimum data over multiple data sets for the same devices.

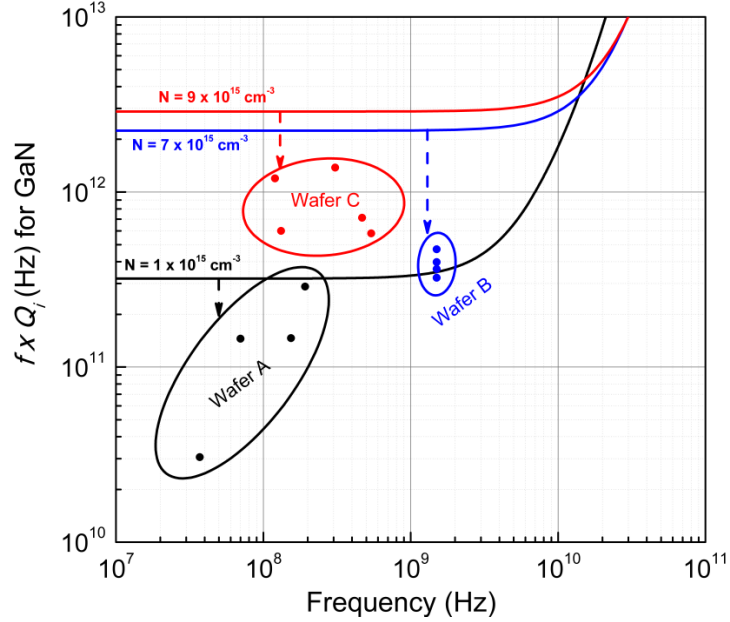


Fig. 4.9 : Measured values of $f \times Q$ for devices above, and the limiting values imposed by the phonon-electron loss. The phonon-electron limits of $f \times Q$ depend on the specific values of N for each individual wafer. The difference between the $f \times Q$ limit and the measured values is due to reflection loss and other extrinsic losses not accounted for in the model. Reflection loss can be lowered by more optimized resonator design, while other losses can be reduced by reducing the defect density of the material lattice, operating the device in a vacuum and at low temperatures.

4.4. Material Dependencies for Acoustoelectric Loss/Gain

The full model for $\alpha_{piezo}^{pe}(\omega, E_D)$ presented in Eqn. 4.13 and shown in Fig. 4.10(a) (for GaN) indicates that α_{piezo}^{pe} is critically dependent on N, μ, K^2 , and s . The electronic properties, N and μ especially, can be tailored by proper crystal growth and doping. These parameters influence the (i) original α_{piezo}^{pe} (at $E_D = 0$), (ii) onset of gain, (iii) frequency of maximum effect ω_{max} , (iv) absolute magnitude of gain/loss, and (v) range of η that results in amplification. Variation of α_{piezo}^{pe} with N and μ is shown in Fig. 4.10 (b)- Fig. 4.10 (e) at both ω_{max} (which varies with N) and at the fixed frequency of 1.5 GHz.

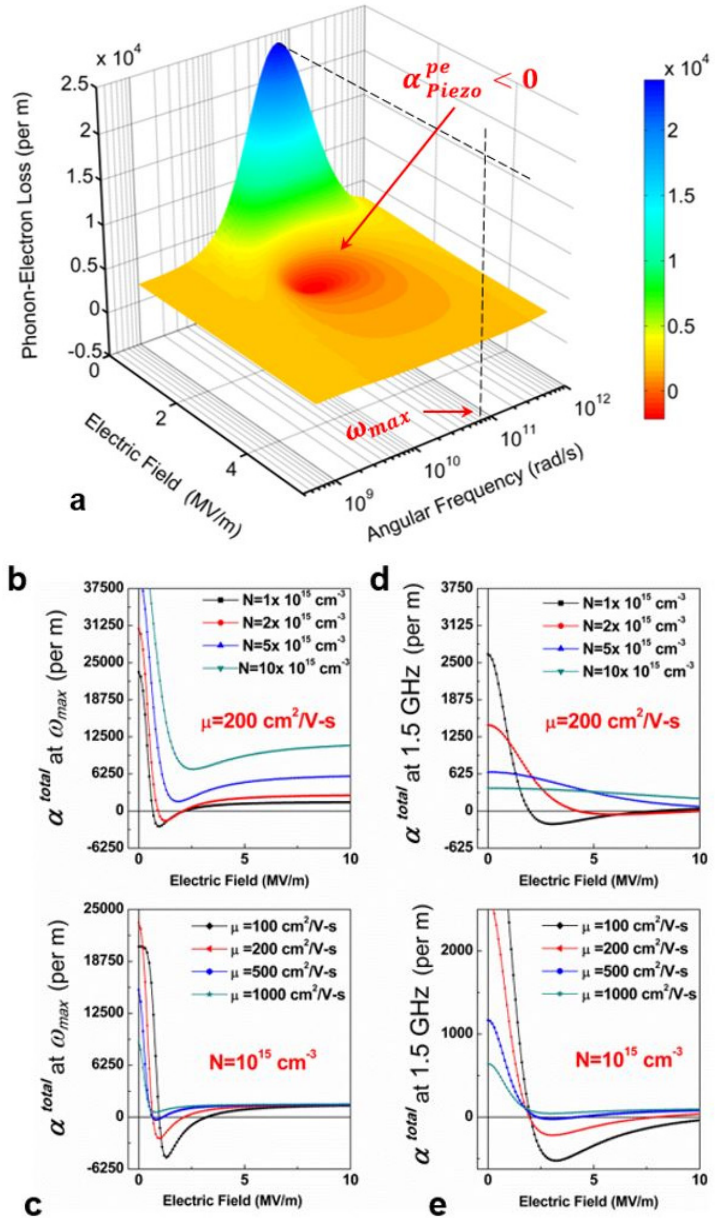


Fig. 4.10 : (a) Phonon-electron loss/gain α_{Piezo}^{pe} as a function of frequency and applied DC electric field, for the wurtzite GaN system with a fixed carrier concentration $N = 10^{15} \text{ cm}^{-3}$ and carrier mobility $\mu=200 \text{ cm}^2/\text{V-s}$. The gain region $\alpha_{Piezo}^{pe}(\omega_r, E_D) < 0$ is clearly seen. Subsequent plots (b)-(e) denote loss α_{Piezo}^{pe} as a function of E_D , at representative frequencies, ω_{max} and 1.5 GHz, with variations in N and μ . The nature of α_{Piezo}^{pe} is highly dependent on these parameters. A similar analysis can be carried out for other piezoelectric semiconductor materials, in order to identify the optimum material properties and design for low-loss or high-gain resonant piezoelectric semiconductor BAW amplifiers.

Comparing trends at 1.5 GHz, we see that higher N screens out piezoelectric interaction, progressively decreases the nominal loss, and thus requires higher applied E_D to decrease α_{Piezo}^{pe} (Fig. 4.10(d)). Maximum achievable gain is reduced with increasing N . Increased μ reduces the threshold E_D required for cross-over, but the minima of α_{Piezo}^{pe} is higher and does not necessarily cross over into the gain regime (

Fig. 4.10(e)). Nevertheless, in all cases, applying E_D to the piezoelectric semiconductor BAW resonator results in lowered α_{Piezo}^{pe} and subsequently an improved Q_i^{total} . As discussed, the threshold velocity ratio η_{th} is the critical value at which $\alpha_{Piezo}^{pe} = 0$. Above η_{th} , α_{Piezo}^{pe} is negative, leading to gain. Solving Eqn. 4.13 for $\alpha_{Piezo}^{pe} = 0$ gives us the critical condition for zero-loss (and zero gain):

$$\eta^2 = 1 + b^2, \quad \text{Eqn. 4.32}$$

which depends on the electronic properties N and μ . The limiting values for amplification are set by the carrier saturation velocity for the particular material. Fig. 4.11 depicts the possible solution space for achieving phonon-electron gain. This solution space is a function of the properties N , μ and ω , while the upper bound for amplification is set by the electron saturation velocity of the material. The parametric trends given by Fig. 4.10 and Fig. 4.11 provide important rules for choosing a piezoelectric semiconductor material and tailoring its properties to reduce nominal electron loss in piezoelectric semiconductor BAW resonators, or to develop piezoelectric semiconductor BAW resonant acoustoelectric amplifiers.

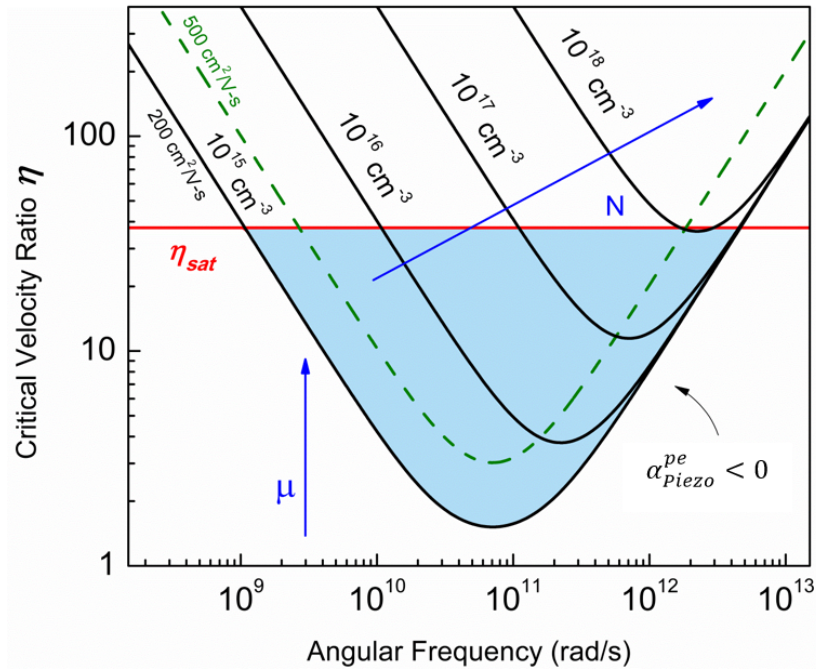


Fig. 4.11 : The critical velocity ratio η_{th} is the threshold value at which $\alpha_{piezo}^{pe} = 0$. Any further increase in the velocity ratio (achieved by applying a higher electric field) would drive the resonator into the gain regime $\alpha_{piezo}^{pe} < 0$. The possible solution space for the gain regime (shown shaded here for the wurtzite GaN system under consideration) is dependent on the electronic properties (N, μ) and the resonant frequency. The upper bound for amplification in any real material is set by the electron saturation velocity.

Using the theoretical model, including all loss mechanisms for GaN, we can qualitatively compare all measured devices and plot relative improvement in Q_m as a function of both frequency and N (Fig. 4.12(a)). For a given set of material properties, higher resonant frequencies ($\omega \rightarrow \omega_{max}$) should result in higher relative amplification of Q_i^{total} . This is verified experimentally for multiple BAW resonators with increasing frequency, fabricated concurrently on the same wafer (Fig. 4.12(b)). The 192 MHz BAW resonator seen here has the dual advantage of having the highest frequency measured on the wafer with lowest N and it expectedly exhibits the highest measured improvement of $\sim 35\%$ in Q_m . Across all four wafers, with

increasing N we also see the expected increase in the measured nominal $f \times Q$ values (Fig. 4.12(c)) and the expected decrease in relative amplification (Fig. 4.12(d)). This verifies the trends predicted in Fig. 4.2 and Fig. 4.10, and is important for the design of low-loss piezoelectric semiconductor BAW resonators, the design of highly-amplifying piezoelectric semiconductor BAW resonators, or an optimized design involving both attributes.

While higher N and μ are generally reported for GaN-based HEMT electronics, the values used here more closely represent the practical values in high-quality, UID bulk GaN [154, 155]. Bulk GaN has an electron saturation velocity greater than 10^5 m/s, comfortably higher than the acoustic velocity by more than an order of magnitude [161, 162]. Impact ionization effects are not expected till electric fields of at least 150 MV/m [163], enabling large values of η before velocity saturation or breakdown.

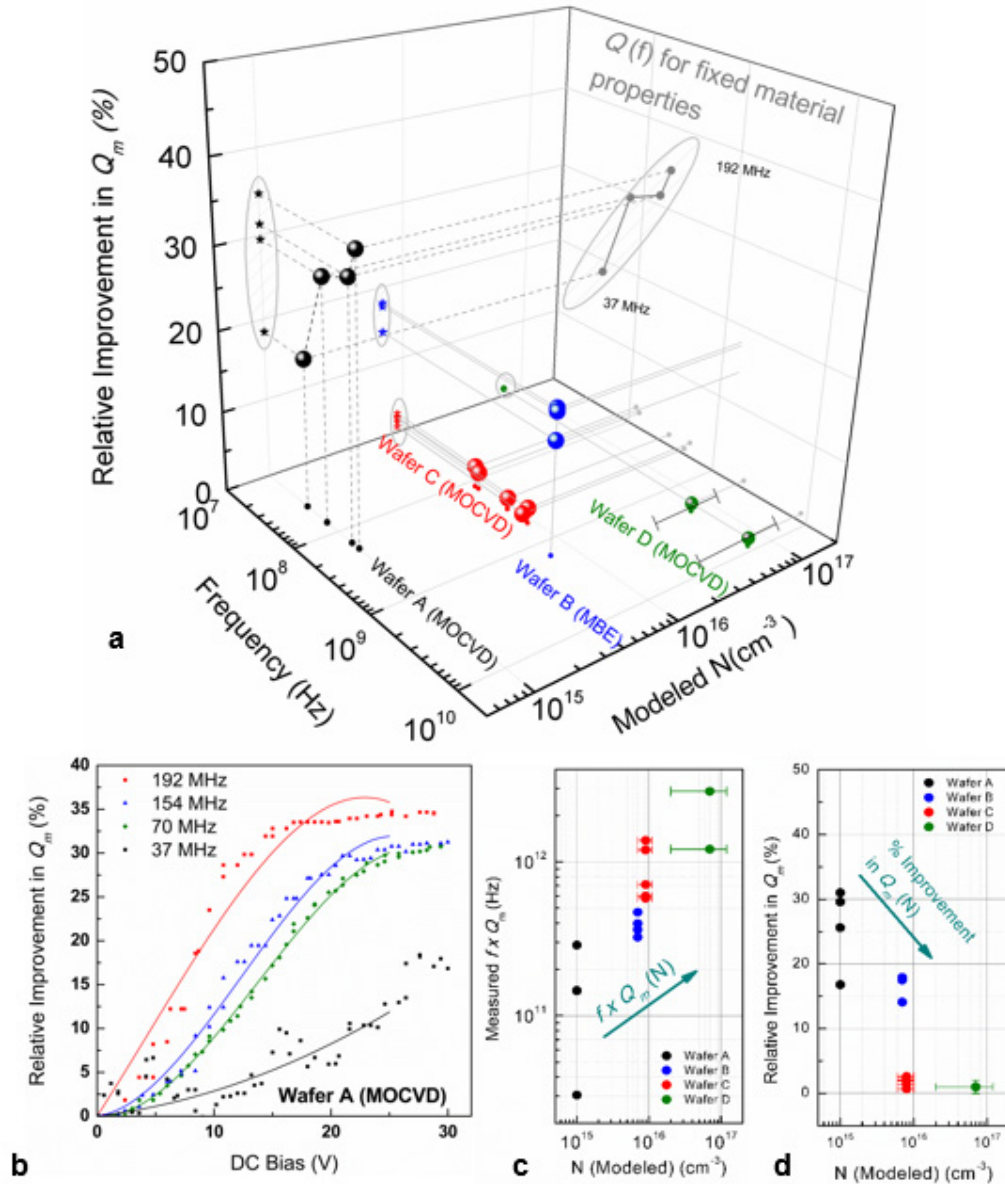


Fig. 4.12 : (a) Relative improvement in Q_m for multiple resonators as a function of frequency and modeled N for four GaN wafers. Planar projections indicate the trends with respect to frequency for a fixed set of material properties (Wafer A). (b) Relative improvement in experimentally measured and extracted Q_m for four BAW resonators concurrently fabricated on Wafer A (and thus possessing the same material properties). As predicted by the model, increasing the resonance frequency ($\omega \rightarrow \omega_{max}$) increases the relative improvement in Q_m . As expected from the model, increasing electron concentration reduces piezoelectrically coupled phonon-electron interactions due to screening, and leads to (c) a higher nominal $f \times Q$ (lower loss) but also (d) a lower relative acoustoelectric improvement in Q_m .

4.5. Experimental Controls

In order to validate the acoustoelectric amplification as the causal phenomenon for the improvement in observed performance of the resonators, it is necessary to evaluate other possible causes such as non-linear current-voltage (I-V) in GaN, temperature, and RF input power. Further, GaN is not ferroelectric [164], and poling is not expected. Any possibilities of this amplification being a charging effect due to the presence of dielectric layers is negated by the fact that electric charges could potentially change the transmission level but cannot amplify specific modes selectively. The control experiments below strongly indicate that neither contact non-linearity, drive power, nor self-heating could be responsible for the improvements in resonator Q seen in this work.

4.5.1. Effect of Contact Non-Linearity

Generally, one important consideration when making electrical connections with GaN films is the contact linearity. Ti/Au is a popular combination for use with n-GaN as the barrier height for Ti to n-GaN [165] is one of the smallest for commonly used materials, even as-deposited without annealing [166]. The Au/Ti/n-GaN top contacts are not fully linear, but are expected to show only weakly-rectifying behavior [167]. The low doping expected of the UID films further means that the current transmission through the GaN is expected to be low. The bottom contact is to the AlN/AlGaIn buffer layer, which can be considered to be a leaky dielectric. The two top electrodes can be considered to be back-to-back (weakly) rectifying contacts providing a leakage

path through GaN, and the measured current transmission characteristics Fig. 4.13 are similar to expected trends for such a configuration with Au/Ti/n-GaN [166]. It should be stressed however that contact non-linearity cannot explain the selective amplification of the mechanical resonance peak of the GaN resonator. Even the use of active GaN HEMTs co-fabricated with GaN resonators has been shown to only shift the entire transmission response of the resonator, without selective amplification of the mechanical peak [142, 157].

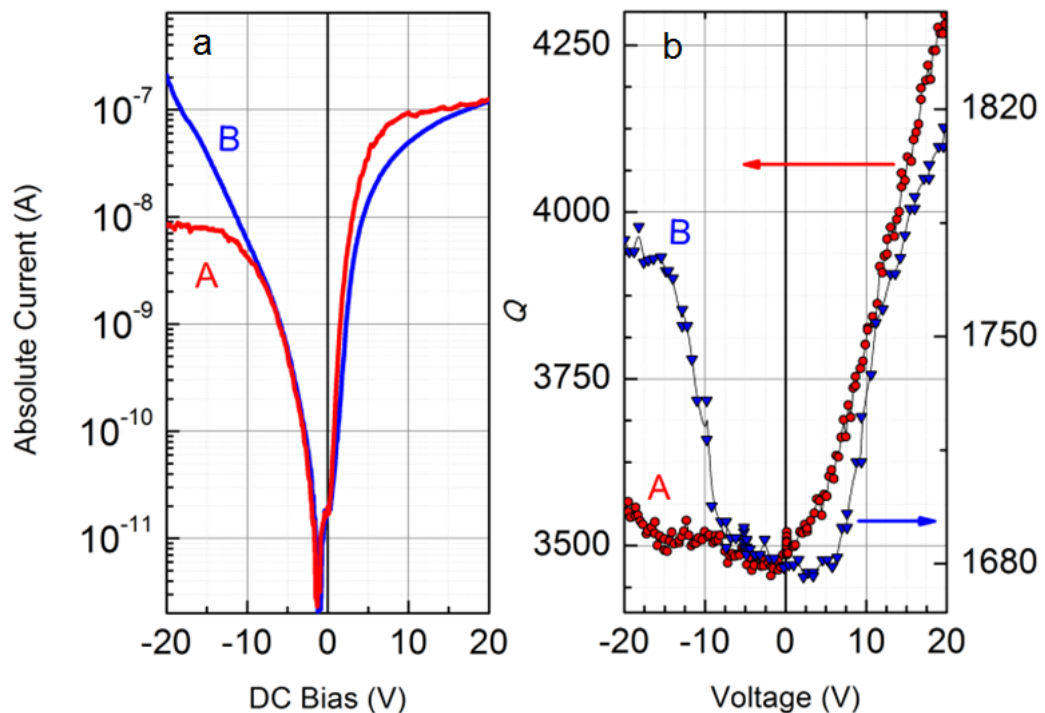


Fig. 4.13 : (a) DC I-V curves and (b) measured resonator Q for two similarly designed BAW resonators. In both cases, positive voltages result in similar trends in improvement of Q . In devices designated type A, a negative voltage results in negligible Q amplification, while in devices of type B, there is a perceptible change in the Q with a negative bias. This is well correlated with the nature of the DC current seen in both type of devices; devices that do not show large currents in the negative bias region do not show improvements in the Q . Further investigation into the n-GaN/Ti/Au contact is necessary to fully characterize and control contact resistance and consequently the Q amplification with negative DC bias.

4.5.2. Effect of RF power

It is known that mechanical resonators have a non-linear relationship between the Q and input RF power. Increasing RF power levels improves the Q till the Duffing non-linearity is achieved [168]. We explore the effect of RF power and observe only small improvements in the Q as we change input power from -20 dBm to 0 dBm (Fig. 4.14). We do not observe the onset of non-linearity within the input range of the experiment.

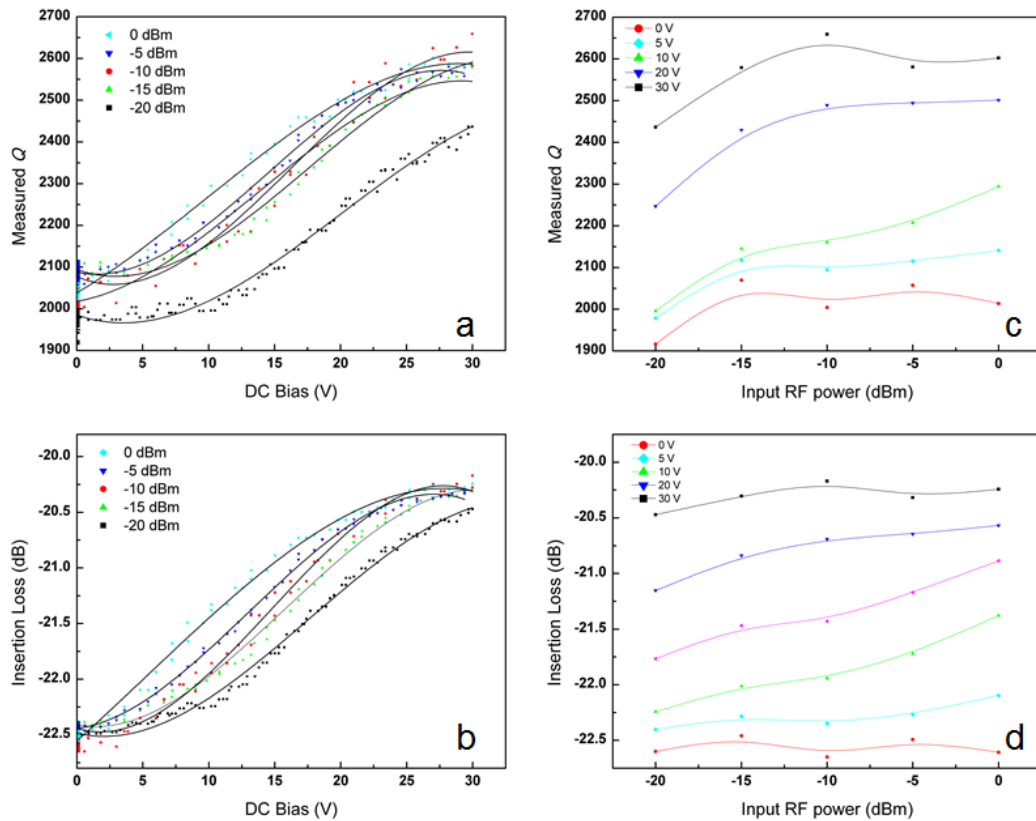


Fig. 4.14 : Change in (a) measured Q and (b) IL of the 70 MHz BAW resonator (Wafer A) with applied DC bias at different levels of RF input power. We can see that increasing the input power temperature improves the Q and IL slightly. (c) & (d) The same data plotted as a function of the RF power, at select values of DC bias. Increasing RF power improves performance slightly, but not significantly when compared to the DC bias.

Increased RF power may also increase the Q due to the same mechanism as the DC bias: an interaction with RF current and the phonons, improving the acoustic performance. This is in effect, a self-actuation mechanism due to the RMS value of the RF current interacting with the acoustic phonons [139]. This change is significantly lower than the improvement seen with DC bias (Fig. 4.14).

4.5.3. Effect of Temperature

The effect of temperature is investigated to gauge the effect of ambient temperature changes or any self-heating due to RF or DC currents. The phonon-phonon, TED, and phonon-electron loss are all expected to increase (lowering Q) at higher temperatures, and this is consistently borne out by experimental evaluation (Fig. 4.15) and previous work [64].

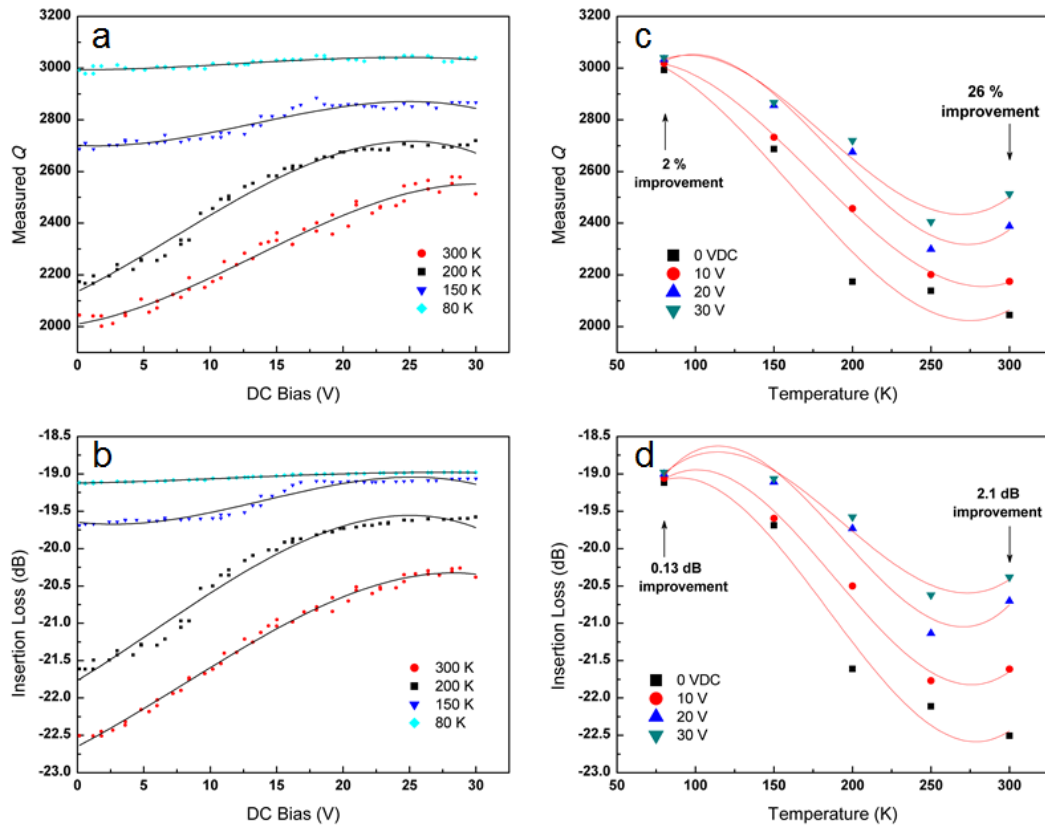


Fig. 4.15 : Change in (a) measured Q and (b) IL of a 70 MHz BAW resonator (Wafer A) with applied DC bias at various temperatures. We can see that elevated temperature reduces the Q and IL. (c) & (d) The same data plotted as a function of the temperature, at select values of DC bias. The reduction in Q improvement at low temperature needs further investigation.

4.6. Potential Materials for Acoustoelectric Amplification

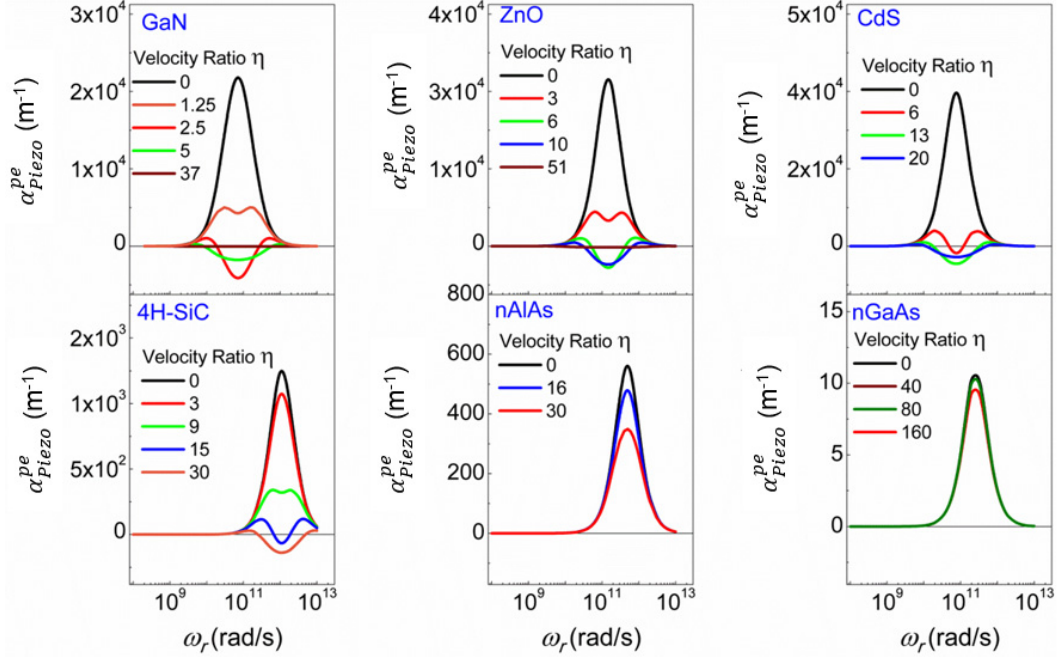


Fig. 4.16 : Potential piezoelectric semiconductor materials for achieving acoustoelectrically amplified BAW resonators. Representative plots for $\alpha_{SW}^{pe}(\omega, \eta)$ for other piezoelectric semiconductor materials that can potentially exhibit acoustoelectric amplification via piezoelectric interactions between phonons and electrons. Each material is investigated up to the limit η_{sat} set by the respective electron saturation velocity. Other loss mechanisms are not considered here. Material properties used for modeling are provided in Table 4.III. Note that the axes are scaled individually for visual clarity.

Numerical calculations are carried out for various candidate piezoelectric semiconductor BAW materials that may potentially exhibit acoustoelectric amplification via piezoelectric interactions between phonons and electrons Fig. 4.16. The representative properties used for a comparison of these materials are provided in Table 4.III. Due to their higher piezoelectric coupling and lower N values, the wurtzite materials (GaN, ZnO, CdS, and 4H-SiC) exhibit a strong phonon-electron interaction and can transition into the gain regime. The velocity ratio η required to transition into the gain regime is low enough that the electron saturation velocity ratio η_{sat} is not exceeded.

Table 4.III
Potential Candidate Materials for Acoustoelectric Amplification

		GaN	ZnO	CdS	4H-SiC	AlAs	n-GaAs
Structure	units	Wurtzite	Wurtzite	Wurtzite	Wurtzite	Cubic	Cubic
K^2	-	0.02	0.217	0.03 - 0.07	8×10^{-4}	1.01×10^{-3}	3.7×10^{-4}
Mobility	cm^2/Vs	150-440	150-200	285	400	180-294	1000 - 9000
Carrier Concentration	cm^{-3}	1×10^{15} - 1×10^{17}	6×10^{15} - 3×10^{16}	4×10^{15}	1×10^{17}	2×10^{17} - 9×10^{17}	1×10^{14} - 1×10^{19}
e_{ij}	C/m^2	0.65	0.96	0.385 - 0.626	0.2	-0.23	-0.16
ϵ_r	-	9	7.5	9.3 - 9.5	9.66	10.1	13.18
Acoustic Velocity	m/s	7960-8040	6200	4300 - 4500	13,100	2910	2470
Saturation Velocity	m/s	3×10^5	3.2×10^5	1×10^5	2.2×10^5	8.5×10^4	2×10^5
Ref.		[138, 161, 162]	[169-171]	[40, 138]	[138, 172-174]	[56, 175, 176]	[175, 176]

The cubic materials (AlAs and GaAs) exhibit a very weak reduction in phonon-electron loss due to low piezoelectric coupling and high N . The wurtzite materials are promising candidates for implementing BAW amplifiers. This model suggests that the piezoelectric mechanism for phonon-electron interaction is not sufficient for inducing acoustoelectric gain in the cubic materials. Note that α^{DP} may be a more significant interaction mechanism for the cubic semiconductors with weak piezoelectric coupling [35], but is not considered at this point. The wurtzite materials are more evenly matched in terms of acoustoelectric performance. Each material offers unique practical advantages such as high-quality epitaxially grown films (GaN), ease of deposition at low temperatures (ZnO, CdS) or low phonon-phonon loss (SiC) [31]. Prior work has shown acoustoelectric amplification in thick crystals of CdS [148] and ZnO [177] but the subsequent development of advanced processing

technology makes it possible to practically design thin submicron films of GaN, CdS, ZnO, or SiC that can increase the fundamental thickness vibration frequency to the 1-10 GHz range, where acoustoelectric amplification can be seen most clearly in standing wave BAW resonators. Similarly, better control of growth or deposition can yield better quality films with tailored electronic properties. These materials can also be used in composite acoustic resonators or superlattices or integrated with electronics, leading to practical electromechanical systems that utilize acoustoelectric amplification to compensate for intrinsic material loss.

4.7. Limits of Acoustoelectric Amplification

The theoretical maximum limits on the acoustoelectric amplification are set by the electron saturation velocity, or the dielectric breakdown field of the material. Bulk GaN has an electron saturation velocity greater than 10^5 m/s, comfortably higher than the acoustic velocity by more than an order of magnitude [161, 162]. Impact ionization effects are not expected till electric fields of at least 150 MV/m [163], enabling large values of η before velocity saturation or breakdown.

The minimum sizes of GaN-based structures where we could potentially observe acoustoelectric interactions is limited by the Debye length,

$$L_D = \sqrt{\frac{\epsilon k_B T}{q^2 N}}, \quad \text{Eqn. 4.33}$$

which is on the order of 10 nm to 100 nm for moderately doped GaN. Thus, this effect could potentially be seen in nanostructures such as GaN nanowires. However,

as the dimensions scale down, the loss will be dominated by surface and interface scattering [178, 179] (which may be orders of magnitude higher than electron loss) and it may not be possible to practically observe the phonon-electron interactions.

Based on the measured voltage-current curves (see Fig. 4.13), the DC power applied to the resonators is on the order of 4 μ W (200 nA for an applied DC voltage of 20 V). The transfer of energy from the electrical domain to the mechanical domain due to the piezoelectric interaction is defined by α_{Piezo}^{pe} , and should necessarily be a fraction of the applied DC electric power. Based on the calculations in Section Chapter 14.1.2, the conversion efficiency is on the order of 0.1% to 0.5% per μ m. The rest of the DC power is dissipated as heat in the device. Heating of the resonator due to applied electric field causes an increase in the vibration energy of an ensemble of phonon modes across a broad spectrum, causing an increase in overall phonon-scattering and thus decreasing the Q . It is expected that practical acoustoelectric amplification would be limited by the increasing phonon loss as we increase the DC bias. It is possible, though not yet verified, that the saturation of amplification seen in most resonators in this work is due to this reason. The experimental results and the limiting values seen in this work are in no way the limiting values of the acoustoelectric phenomenon. With optimized material properties and the correct resonator design, it is expected that significantly higher gain is practically possible.

4.8. Discussion

By definition, mechanical devices made from piezoelectric semiconductor materials rely on the interactions between the electronic and mechanical domains. In practical devices, these interactions are lossy and with limited conversion efficiency. This work explores the possibility of mitigating the mechanical losses and achieving the most energy efficient devices by choosing the right material properties and designs. Furthermore, we demonstrate that it is possible to utilize the reverse effect: pumping electrical energy into the system to offset the mechanical losses. This dynamic and reversible improvement in the Q of piezoelectric semiconductor BAW resonators can be distinctly observed on applying a DC electric field. Experimental work presented here has focused on GaN as it is a high-quality acoustic piezoelectric semiconductor material predicted to be optimal for demonstrating acoustoelectric amplification [139, 163]. Measured results presented here verify these predictions. Other piezoelectric semiconductor materials could also be potentially used to achieve Q -amplified BAW resonators.

An important question arising from this work is whether one can overcome all other sources of loss in a practical piezoelectric semiconductor BAW resonator and achieve frequency-selective resonant BAW amplifiers. That is, is it possible to obtain $\alpha_{Piezo}^{pe} < 0$ and at the same time $|\alpha_{Piezo}^{pe}| > (\alpha^{pp} + \alpha^{TED} + \alpha_{DP}^{pe} + \alpha^{reflection} + \dots)$ in thin film piezoelectric semiconductor BAW devices? Net acoustic gain has been experimentally measured for CdS-based acoustoelectric travelling-wave amplifiers [37, 38]. This indicates that it is possible to compensate for

all loss mechanisms and further actively amplify the acoustic travelling wave. Based on the models and properties for the relevant materials, this work demonstrated that it is theoretically possible to achieve acoustic gain and high Q values exceeding the intrinsic limits of the materials for standing waves in piezoelectric semiconductor BAW resonators. If the acoustic gain via piezoelectric coupling exceeds, in absolute value, the magnitude of all losses combined, then the resonator stores acoustic energy (by consuming DC power) and the Q is undefined using the conventional description (a ratio of energy stored and energy dissipated). To demonstrate this experimentally, further investigation is necessary into piezoelectric semiconductor BAW resonators made with high-quality thin-film materials, such as GaN, CdS, or ZnO. Ideally, the resonators should be optimized for low reflection loss, operated under controlled pressure/temperature, and stimulated with continuous wave or pulsed DC excitation. This would enable exhaustive investigation into acoustoelectric interactions in piezoelectric semiconductor materials and encourage the design of a new class of high-performance acoustoelectrically amplified resonant devices, which could be used for high-sensitivity sensors, such as the resonant IR sensors of this work.

Chapter 5 Summary and Future Work

5.1. Summary

The use of GaN resonators and filters can provide a new dimension to high-power, high-speed electronics, optoelectronics, and power electronics based on GaN. Thorough characterization of the high-frequency electromechanical properties of GaN is an essential prerequisite of such research and development. This thesis presented some of the first high-frequency micromechanical resonators fabricated using single crystal GaN. GaN resonators were found to possess high performance, and have great potential for implementation in GaN based integrated electromechanical systems.

The use of these GaN resonators as resonant IR detectors is one specific application that is addressed in this work. We presented the first monolithically integrated thin-film arrays of resonant IR detectors, made from GaN and other materials. These resonant IR detectors are capable of achieving a small footprint, high sensitivity, and extremely low noise levels, as evidenced by the designed NETD of 10 mK. We present comprehensive analysis of the design rules and optimization principles needed to fabricate these arrays, in an effort to achieve performance comparable to commercial uncooled IR detectors. As part of this effort, two novel IR

absorber coating materials were developed: a CNT-based polymer nanocomposite and a metamaterial grating that selectively absorbs a particular infrared wavelength.

In order to investigate the seemingly anomalous and unprecedented amplification of Q in GaN resonators, we investigated phonon-electron interactions in GaN bulk acoustic wave resonators. We show that while these interactions generally constitute a significant acoustic energy loss mechanism in GaN, under appropriate conditions, these interactions are reversible and can lead to acoustic gain in the material at the expense of electrical energy. A comprehensive model for the interactions of phonons and electrons in resonators made from piezoelectric semiconductor materials such as GaN, ZnO, CdS, SiC, GaAs, *etc.* was derived. This model is a classical treatment of the interactions and describes both the acoustoelectric gain and loss in bulk devices. This model, along with the experimental results that validate it, is a first step towards the implementation of high-gain, narrowband mechanical amplifiers or high-sensitivity IR detectors based on acoustoelectric amplification.

5.2. Future Research Directions

This work yielded some important insights into GaN resonators and resonant IR detectors, both in terms of theoretical understanding and practical design principles. The following sections discuss some of the potential future directions for this research.

5.2.1. Resonant IR Detector Arrays

This work accomplished the first prototype resonant IR detectors and small format arrays, using GaN or other materials. A number of steps are necessary before

these prototypes can be translated into commercially viable FPAs. Some of these steps are part of the ongoing research in the Resonant MEMS group.

The next set of AlN and AlN-on-SiO₂ arrays shall have up to 256 pixels in a 900 $\mu\text{m} \times 900 \mu\text{m}$ area (Fig. 5.1), with bilayer routing in order to optimize the pixel packing density. The bilayer routing is achieved by using doped polysilicon traces under the AlN layer for routing. The individual resonator pixels are designed with a 10 $\mu\text{m} \times 15 \mu\text{m}$ area to achieve low footprint, and yet maintain an NETD of under 10 mK and a time response of under 3 ms.

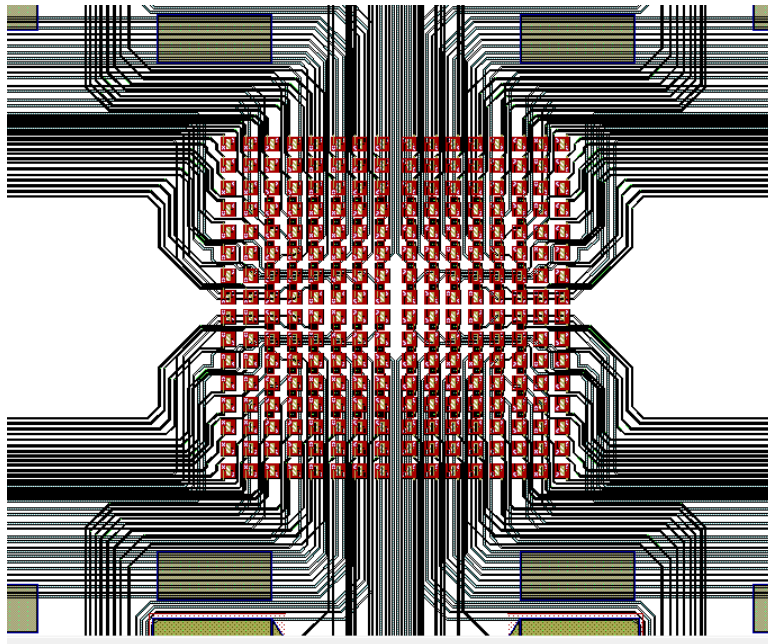


Fig. 5.1: A medium format array with 256 pixels. The total area of the FPA is 900 $\mu\text{m} \times 900 \mu\text{m}$. High packing density can be achieved in this format by using polysilicon traces. The polysilicon layers will be under the AlN layers, separated by thick isolating oxide layers. The resonators will be released using a dry gas-phase XeF₂ etch.

The routing and placement of the resonator pixels is a significant challenge as the pixel footprint decreases, packing density of the array increases, and total array size

increases. In future implementations, a more efficient way to manage routing complexity is to use a separate readout IC chip, bonded to the resonator array.

5.2.2. AlN-on-SiO₂ with SiO₂ Tethers

As discussed previously GaN cannot be grown on low thermal conductivity substrates that can be easily machined, and thus the structure will have a relatively high thermal conductivity (~ 130 W/m-K). This leads to high thermal conductance through the tethers, on the order of 10^{-5} W/K or 10^{-4} W/K for GaN and GaN-on-SOI designs. To be competitive with commercial IR designs, with device area on the order of $20\ \mu\text{m} \times 20\ \mu\text{m}$, the thermal conductance needs to be on the order of 10^{-7} to 10^{-6} W/K. Towards this goal, we explore a novel fabrication technique involving a composite resonator stack. The main structural element of the resonator plate and the tethers is SiO₂, which has a thermal conductivity of 1.1 W/m-K (100 \times lower than the GaN-based counterparts). An AlN layer deposited on the resonator plate (but etched away from the tethers) is responsible for resonator actuation. Electrical connection is made using thin (20 nm) Ti traces, as Ti has a low thermal conductivity of 22 W/m-K. Thus, the tethers are made of only Ti and oxide (Fig. 5.2) and thus give us thermal conductance values between 5×10^{-8} W/K and 5×10^{-7} W/K for various designs, and can drive down expected NETD values down to 5 mK, even for detector areas of as low as $20\ \mu\text{m} \times 20\ \mu\text{m}$. The resonators are dry-released using XeF₂ (Fig. 5.3). The bottom electrode was Ti during initial runs but changed to TiN (thermal conductivity of 30

W/m-K) as the Ti surface was found to oxidize and thus degrade electrically during processing.

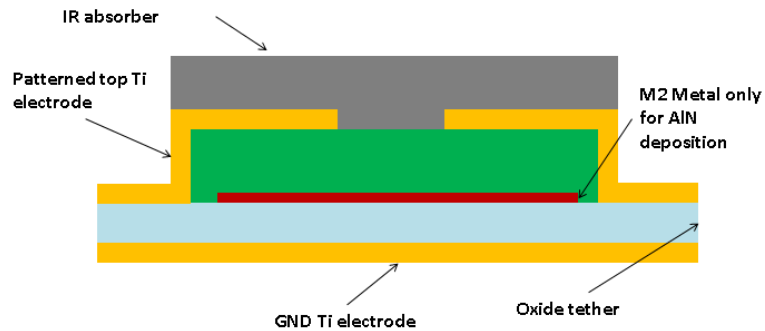


Fig. 5.2 : Schematic showing the device cross-section for a composite material thin-film resonator for low NETD IR detection. The structural layer is 300 nm SiO_2 , with 250 nm AlN on the resonator plate for actuation, and up to 200 nm of SiN_x for IR absorption. The tethers are comprised of low thermal conductance Ti- SiO_2 -Ti. Molybdenum or platinum is used as a seed layer for improving AlN crystal quality, but is not present on the tethers, and does not contribute to thermal conduction.

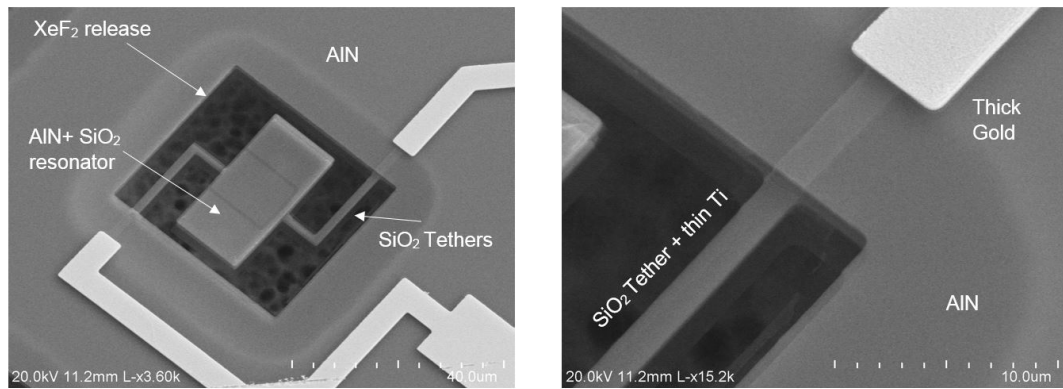


Fig. 5.3 : (a) An SEM image of a fabricated AlN-on- SiO_2 resonant IR detector. (b) The tethers are made solely of SiO_2 and thin Ti in order to reduce the thermal conductance of the tethers.

The process yield of the various structures is excellent, with almost all the devices surviving mechanically. This can be attributed to the low stress of the AlN and SiO_2 films, and the small pixel sizes. However, none of the resonators were found to be working. Probable causes are the quality of AlN grown on oxide or the electrical

quality of the thin films used as electrodes. Ongoing and future work aims at investigating and addressing these issues.

5.2.3. Readout Circuits

In conjunction with collaborators, the next batch of AlN-on-Si resonators in a wafer-level bonded MEMS-CMOS die shall have CMOS-based amplifiers to use the resonators in a feedback oscillator loop. This can be implemented by having one amplifier per resonator or one amplifier in total, with switching circuitry.

Another method of implementing a readout circuit for resonant IR detectors is in an open loop configuration. In the proposed method, the readout is excited with a frequency close to the desired resonance mode for a short time. Then, the excitation is switched off and the resonator produces an exponentially-damped sinusoidal signal (ring-down signal). From this ring-down signal, resonant frequency and even Q can be extracted by counting the number of signal periods before it dies out. This is another research presently pursued in the Resonant MEMS group.

In certain harsh environments, it is possible that CMOS circuitry will not be useful. One of the advantages of GaN is the possibility of integrating GaN resonators with GaN HEMT electronics, on the same substrate. This has been demonstrated by others in the Resonant MEMS group. GaN resonant IR detectors can be coupled with GaN HEMTs to form free-running oscillators in the Pierce configuration.

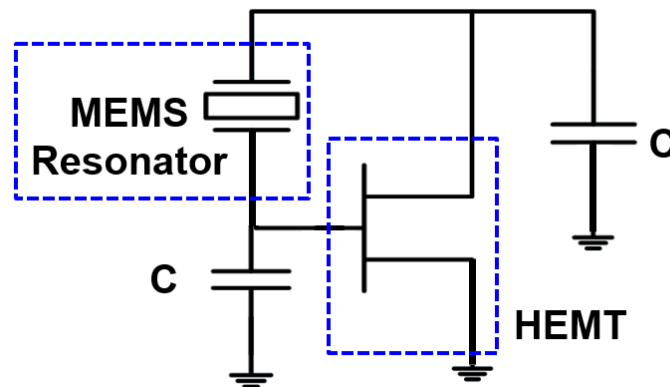


Fig. 5.4 : Schematic showing a Pierce oscillator constructed using a GaN MEMS resonator and a GaN HEMT transistor. The two GaN elements can be co-fabricated on the same substrate, as demonstrated by Ansari *et al* [128].

The power required to drive the resonant IR detectors to get high performance is on the order of 10 μ W to 100 μ W, depending on the size, material and frequency of the device. The use of a differential pair will obviously double the power consumption. For array implementation it is not feasible to continually keep all resonators in the operation state at all times. An electronic switching/scanning readout can be used that addresses each resonator pixel (or groups of pixels) sequentially [15]. Given the fast response times achieved by these detectors, it is possible to scan a number of pixels and still maintain the 30 Hz – 100 Hz video frame rate requirements. This, and the use of efficient, low-power readout circuitry, will maintain system power consumption at or under \sim 10 mW.

5.2.4. Characterization using a Blackbody Source

Industrial standards for testing the practical temporal and spatial NETD call for measuring the response of an FPA to a calibrated large area black-body radiation

source. The arrays and the readout circuitry shall be tested using an LES-100-04E large-area blackbody source (Electro-Optical Technologies, Santa Barbara, CA), recently acquired by the Resonant MEMS group. The blackbody source has a NIST-traceable calibration, an emissivity of 99% up to 100 °C, and setpoint accuracy of 10 mK.

To the best of our knowledge, there are no exhaustive, repeatable and statistically significant experimental results that systematically isolate and investigate the various loss mechanisms and operational regimes at high frequencies. This is the most important future research goal for the project. Such knowledge will be vital in understanding the physical mechanisms involved and in the design of the next generation of high-frequency, low-loss resonators.

5.2.5. Quality Factor Improvement and its Effect on IR Sensitivity

One of the important operational parameters of a resonator is its Q . For resonant sensors, the Q of the resonator is one of the most important parameters setting the limit of resolution and the limit of detection. The minimum detectable change in the frequency of a resonator is an inverse function of Q [67].

$$\Delta f_{min} = \sqrt{\frac{f_0 k_B B T}{2\pi k Q \langle z^2 \rangle}} \quad \text{Eqn. 5.1}$$

where B is the measurement bandwidth, k is the stiffness of the material, k_B is the Boltzmann constant and $\langle z^2 \rangle$ is the time averaged square of the displacement

amplitude. As discussed in previous chapters, improving the Q of the resonant IR detectors will improve the NETD performance and sensing resolution.

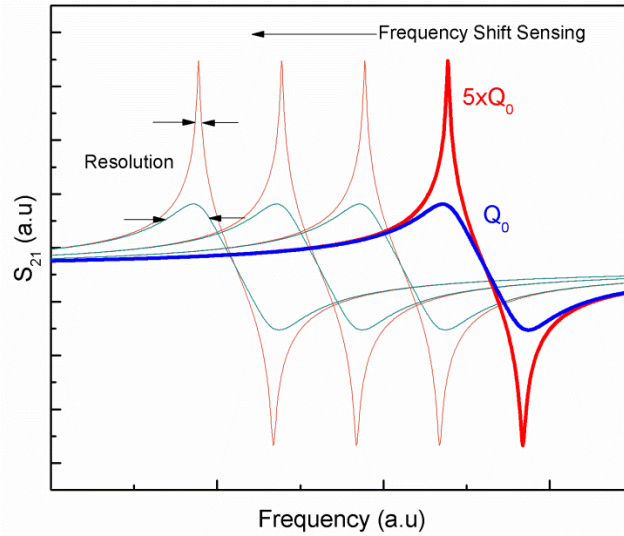


Fig. 5.5 : A schematic showing the importance of the Q in frequency-shifting resonant sensors. At a given frequency, the sensing resolution (by convention compared at the -3dB bandwidth) improves by a factor of \sqrt{Q} . All other factors kept constant, the insertion loss also improves, making it easier to interface the sensor with electronics.

5.2.6. Loss Mechanisms in Resonators

The research into the phonon-electron loss in resonators and the acoustoelectric effect leads to a bigger question: understanding, separating and reducing the intrinsic loss mechanisms in resonators operating at high frequencies ($> 1\text{ GHz}$). While some experimental results by various researchers have demonstrated promising results, a more systematic study is needed to isolate and separate specific loss mechanisms at high frequencies. For phonon loss, the transition between the Akhieser regime and the Landau-Rumer is not conclusively established and is a critical factor in determining the performance of these high-frequency devices. As shown in Chapter 4, the electron loss can be very significant at frequencies $> 1\text{ GHz}$. Very few data exist for electron-

loss other than the work presented here, and acoustoelectric amplification as a practical application is in its infancy. An analysis of resonators fabricated using different substrates with well characterized electronic properties can provide good experimental verification of the acoustoelectric gain/loss in high-frequency resonators. The use of multiple methods of characterization including optical, interferometric, stroboscopic measurements shall be used to complement electrical measurements in order to eliminate losses that occur during electrical actuation of the resonators.

Appendix A- Derivation of Phonon-Electron Interactions for Travelling Waves in Piezoelectric Semiconductors

The classical small-signal treatment of the interactions of acoustic travelling waves and electrons in a piezoelectric semiconductor material was first fully described in a series of papers by A.R. Hutson and D.L. White [39-41, 180, 181] in the early 1960's. Hutson and White, among others, analytically and experimentally demonstrated that this interaction is reversible for travelling waves. We seek to prove the same for standing waves. Since we seek to extend their work to understand such interactions in standing wave elastic cavities (mechanical resonators) [24], we first present a full derivation of the interaction coefficient (commonly known as the acoustic attenuation coefficient) for travelling waves in piezoelectric semiconductors.

The piezoelectric constitutive equations of state are:

$$T = cS - eE \tag{Eqn. A 1}$$

$$D = eS + \epsilon E \tag{Eqn. A 2}$$

The one-dimensional elastic wave equation is given by:

$$\rho \left(\frac{\partial^2 u}{\partial t^2} \right) = \frac{\partial T}{\partial x} \tag{Eqn. A 3}$$

$$\rho \frac{\partial^2 u}{\partial t^2} = c \frac{\partial S}{\partial x} - e \frac{\partial E}{\partial x} = c \frac{\partial^2 u}{\partial x^2} - e \frac{\partial E}{\partial x} \quad \text{Eqn. A 4}$$

To expand the above terms we use Gauss' divergence theorem and the equation of charge/current continuity in a semiconductor material.

$$\frac{\partial D}{\partial x} = Q \quad \text{Eqn. A 5}$$

$$\frac{\partial J}{\partial x} = - \frac{\partial Q}{\partial t} \quad \text{Eqn. A 6}$$

$$Q = -qn_s \quad \text{Eqn. A 7}$$

Here q is the magnitude of electronic charge and n_s is the number of electrons to produce the required space charge.

The current in the n-type semiconductor is given by:

$$J = q\mu n_c E + qD_n \left(\frac{\partial n_c}{\partial x} \right) \quad \text{Eqn. A 8}$$

The first term above is the drift current due to the applied electric fields, and the second term is the diffusion current due to a concentration gradient. $D_n = \frac{\mu k_B T}{q}$ is the Einstein coefficient for diffusion of electrons in a semiconductor. n_c is the number of conduction electrons. The number of electrons in the conduction band are written as:

$$n_c = n_0 + f n_s \quad \text{Eqn. A 9}$$

n_0 is the equilibrium number of electrons in the absence of the acoustic wave, and $f \in [0,1]$ is a fraction of the space charge that is available for conduction. This correction is due to the presence of trapping that may produce space charge, without participating due to conduction electrons. From the above set of equations, we proceed to eliminate J, n_s, n_c in the following manner.

$$J = q\mu n_c E + qD_n \left(\frac{\partial n_c}{\partial x} \right) \quad \text{Eqn. A 10}$$

$$J = q\mu n_0 E + q\mu f n_s E + qD_n \left(\left(\frac{\partial n_0}{\partial x} \right) + \frac{\partial (f n_s)}{\partial x} \right) \quad \text{Eqn. A 11}$$

$$J = q\mu n_0 E + q\mu f E \left(\frac{-1}{q} \frac{\partial D}{\partial x} \right) + qD_n f \frac{\partial n_s}{\partial x} \quad \text{Eqn. A 12}$$

$$J = \left[qn_0 - f \frac{\partial D}{\partial x} \right] \mu E - D_n f \frac{\partial^3 D}{\partial x^3} \quad \text{Eqn. A 13}$$

Use the spatial derivative of J to get:

$$\frac{\partial J}{\partial x} = \mu \frac{\partial}{\partial x} \left\{ \left[qn_0 - f \frac{\partial D}{\partial x} \right] E \right\} - D_n f \left(\frac{\partial^3 D}{\partial x^3} \right) \quad \text{Eqn. A 14}$$

$$\Rightarrow - \frac{\partial^2 D}{\partial x \partial t} = \mu \frac{\partial}{\partial x} \left\{ \left[qn_0 - f \frac{\partial D}{\partial x} \right] E \right\} - D_n f \frac{\partial^3 D}{\partial x^3} \quad \text{Eqn. A 15}$$

The next step is to eliminate D and write a relation in terms of the electric field applied, and the material displacement. Now, assuming plane acoustic waves in the material, we can write the displacement (of every particle) as:

$$u(x, t) = ue^{i(kx-\omega t)} \quad \text{Eqn. A 16}$$

Where the propagation constant k is a complex quantity comprised of the real propagation and the attenuation, given by:

$$k = \omega/s + i\alpha \quad \text{Eqn. A 17}$$

For practical, high-quality materials that support plane elastic wave propagation, $\alpha \ll \omega/s$. The small signal electric field is given by:

$$E = E_0 + E_1 e^{i(kx-\omega t)} \quad \text{Eqn. A 18}$$

The DC field E_0 is due to external applied voltage, while the sinusoidal component is due to the ultrasonic wave propagating through the piezoelectric medium.

For the convenience of the derivation, we can write down and simplify some of the derivatives (with respect to time and space) for the physical quantities in question.

$$\left. \begin{aligned} \frac{\partial E}{\partial x} &= (E - E_0)(ik) \\ \frac{\partial^2 E}{\partial x^2} &= (E - E_0)(ik)^2 \\ \frac{\partial^3 E}{\partial x^3} &= (E - E_0)(ik)^3 \\ \frac{\partial E}{\partial t} &= (E - E_0)(-i\omega) \end{aligned} \right\} \quad \text{Eqn. A 19}$$

$$\left. \begin{aligned}
\frac{\partial u}{\partial x} &= u(ik) \\
\frac{\partial^2 u}{\partial x^2} &= u(ik)^2 \\
\frac{\partial^3 u}{\partial x^3} &= u(ik)^3 \\
\frac{\partial u}{\partial t} &= u(-i\omega)
\end{aligned} \right\} \text{Eqn. A 20}$$

Now, we expand Eqn. A 15:

$$-\frac{\partial^2 D}{\partial x \partial t} = \mu q n_0 \left(\frac{\partial E}{\partial x} \right) - \mu f \left[E \left(\frac{\partial^2 D}{\partial x^2} \right) + \frac{\partial D}{\partial x} \cdot \frac{\partial E}{\partial x} \right] - D_n f \left(\frac{\partial^3 D}{\partial x^3} \right) \quad \text{Eqn. A 21}$$

$$-\frac{\partial^2 D}{\partial x \partial t} = q \mu n_0 (E - E_0)(ik) - \mu f E \{ e u(ik)^3 + \epsilon (ik)^2 (E - E_0) \} - D_n f \{ e u(ik)^4 + \epsilon (ik)^3 (E - E_0) \} \quad \text{Eqn. A 22}$$

$$-\frac{\partial^2 D}{\partial x \partial t} = q \mu n_0 (E - E_0)(ik) - \mu f E e u(ik)^3 - \mu f E \epsilon (ik)^2 (E - E_0) - D_n f \{ e u(ik)^4 + \epsilon (ik)^3 (E - E_0) \} \quad \text{Eqn. A 23}$$

Reorganizing the terms, we get:

$$-\frac{\partial^2 D}{\partial x \partial t} = (E - E_0)(ik) \{ q \mu n_0 - \mu f E \epsilon (ik)^2 - D_n f \epsilon (ik)^2 \} - (ik) \{ \mu f E e u(ik)^2 + D_n f e u(ik)^3 \} \quad \text{Eqn. A 24}$$

To eliminate \mathbf{D} , we start with the piezoelectric equation of state (Eqn. A 2), and try to compare its derivatives to Eqn. A 15. We use Eqn. A 19 and Eqn. A 20 and simplify the expressions.

$$D = eS + \epsilon E$$

Eqn. A 25

$$\frac{\partial D}{\partial x} = e \frac{\partial^2 u}{\partial x^2} + \epsilon \frac{\partial E}{\partial x}$$

Eqn. A 26

$$\Rightarrow \frac{\partial D}{\partial x} = eu(ik)^2 + \epsilon(E - E_0)(ik)$$

$$\frac{\partial^2 D}{\partial x^2} = eu(ik)^3 + \epsilon(ik) \frac{\partial E}{\partial x}$$

Eqn. A 27

$$\Rightarrow \frac{\partial^2 D}{\partial x^2} = eu(ik)^3 + \epsilon(ik)^2(E - E_0)$$

$$\frac{\partial^3 D}{\partial x^3} = eu(ik)^4 + \epsilon(ik)^3(E - E_0)$$

Eqn. A 28

$$\frac{\partial^2 D}{\partial x \partial t} = eu(ik)^2(-i\omega) + \epsilon(ik)(-i\omega)(E - E_0)$$

Eqn. A 29

$$\Rightarrow -\frac{\partial^2 D}{\partial x \partial T} = (ik)(i\omega)[eu(ik) + \epsilon(E - E_0)]$$

Eqn. A 30

Comparing Eqn. A 24 and Eqn. A 30, and reorganizing terms, we get:

$$\begin{aligned} (E - E_0)\{q\mu n_0 - \mu f E \epsilon(ik) - \epsilon(i\omega) - D_n f \epsilon(ik)^2\} \\ = eu(ik)(i\omega) + \mu f E eu(ik)^2 + D_n f eu(ik)^3 \end{aligned}$$

Eqn. A 31

Defining $q\mu n_0 \equiv \sigma$, the conductivity of the material, and rearranging terms,

$$\begin{aligned}
(E - E_0)[- \epsilon(i\omega)] & \left\{ 1 + \frac{\mu f E \epsilon(ik)}{\epsilon(i\omega)} + \frac{i\sigma}{\epsilon\omega} + iD_n f \omega \left(\frac{k}{\omega}\right)^2 \right\} \\
& = (-euk\omega) \left\{ 1 + \mu f E \left(\frac{k}{\omega}\right) + iD_n f \omega \left(\frac{k}{\omega}\right)^2 \right\}
\end{aligned} \tag{Eqn. A 32}$$

$$(E - E_0) = \frac{(-euk\omega)}{-\epsilon(i\omega)} \frac{\left\{ 1 + \mu f E \left(\frac{k}{\omega}\right) + iD_n f \omega \left(\frac{k}{\omega}\right)^2 \right\}}{\left\{ 1 + \mu f E \left(\frac{k}{\omega}\right) + \frac{i\sigma}{\epsilon\omega} + iD_n f \omega \left(\frac{k}{\omega}\right)^2 \right\}} \tag{Eqn. A 33}$$

$$E = E_0 + \left\{ \frac{-(ieuk)}{\epsilon} \right\} \Psi \tag{Eqn. A 34}$$

Where,

$$\Psi = \frac{\left\{ 1 + \mu f E \left(\frac{k}{\omega}\right) + iD_n f \omega \left(\frac{k}{\omega}\right)^2 \right\}}{\left\{ 1 + \mu f E \left(\frac{k}{\omega}\right) + \frac{i\sigma}{\epsilon\omega} + iD_n f \omega \left(\frac{k}{\omega}\right)^2 \right\}} \tag{Eqn. A 35}$$

Ψ is independent of both time and space, and is purely a function of material properties and operating conditions.

$$\frac{\partial E}{\partial x} = 0 + \left\{ \frac{-(iek)}{\epsilon} \right\} \Psi \frac{\partial u}{\partial x} \tag{Eqn. A 36}$$

Using this in the 1-D elastic wave equation (Eqn. A 4), we get:

$$\rho \frac{\partial^2 u}{\partial t^2} = c \frac{\partial^2 u}{\partial x^2} - e \left\{ \frac{-(iek)}{\epsilon} \right\} \Psi \frac{\partial u}{\partial x} \tag{Eqn. A 37}$$

$$\rho u (-i\omega)^2 = cu(ik)^2 + \frac{e^2}{\epsilon} (ik)^2 u \Psi \tag{Eqn. A 38}$$

$$\rho\omega^2 = c \left(\mathbf{1} + \frac{\mathbf{e}^2}{c\epsilon} \Psi \right) k^2 \quad \text{Eqn. A 39}$$

Which is of the standard form of the elastic wave equation, $\rho\omega^2 = c'k^2$, and the effective stiffness is given by

$$c' = c \left(\mathbf{1} + \frac{\mathbf{e}^2}{c\epsilon} \Psi \right) \quad \text{Eqn. A 40}$$

This is the piezoelectrically stiffened expression for material stiffness. The presence of Ψ makes c' a complex quantity, which can be split up into real component (perfectly elastic stiffness coefficient) and the imaginary component (inelastic loss coefficient). Ψ can be further simplified by making the following simplifications, based on the definitions of plasma frequency ω_c and the diffusion frequency ω_D ,

$$\left. \begin{aligned} \omega_c &= \frac{\sigma}{\epsilon} \\ \omega_D &= \frac{s^2}{D_n} \end{aligned} \right\} \quad \text{Eqn. A 41}$$

And for an electric field oriented in the direction of wave propagation, we define the ratio of drift velocity to acoustic velocity as

$$\eta = \frac{\mu f E}{s} \quad \text{Eqn. A 42}$$

From Eqn. A 35, Eqn. A 41, Eqn. A 42, we can write:

$$\Psi = \left\{ \frac{(1 + \eta) + i \left(\frac{\omega}{\omega_D} \right)}{(1 + \eta)^2 + i \left(\frac{\omega_c}{\omega} + \frac{\omega}{\omega_D} \right)^2} \right\} \quad \text{Eqn. A 43}$$

The attenuation coefficient can be written as [39]:

$$\alpha = \frac{\omega}{s} \text{Im} \{ \sqrt{c'} \} \quad \text{Eqn. A 44}$$

Where we use the standard definition of acoustic velocity, $s = \sqrt{\frac{c}{\rho}}$. Since $\frac{e^2}{c\epsilon} \ll$

1, we can simplify the attenuation coefficient to:

$$\alpha = \frac{e^2}{2c\epsilon} \frac{\omega_c}{s} \left(\frac{(1 + \eta)}{(1 + \eta)^2 + \left(\frac{\omega_c}{\omega} + \frac{\omega}{\omega_D} \right)^2} \right) \quad \text{Eqn. A 45}$$

If the electric field opposes the wave propagation vectors, we change $\eta \rightarrow (-\eta)$. Under normal circumstances, $\alpha > 0$, and there is attenuation of acoustic waves in the material. With an applied electric field, $\alpha \leq 0$, and there is acoustic gain in the system (Fig. A 1). Note that the attenuation coefficient is dependent on the direction (or polarity) of the electric field, and thus α is not symmetric about $E = 0$. Instead, α is anti-symmetric about the point $E = \frac{s}{\mu}$. Unlike this situation, the attenuation/amplification in a standing wave cavity is ideally independent of the polarity of the electric field. We use Eqn. A 45 as a starting point for our own analysis for acoustoelectric amplification in standing waves in resonators made from GaN. The experimental arrangement and measured results for CdS based on Hutson and White's experiment are shown in Fig. A 2 and Fig. A 3 respectively.

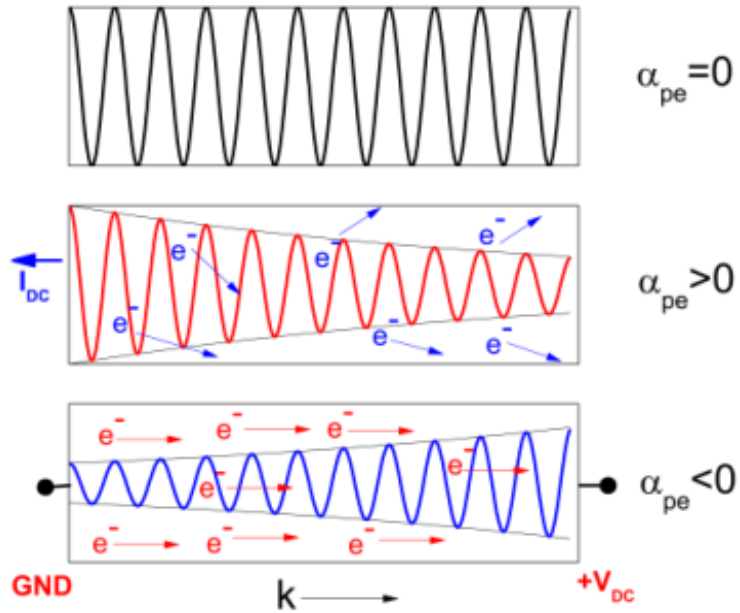


Fig. A 1 : A graphical depiction of the theory of acoustoelectric amplification for travelling waves in piezoelectric semiconductors.

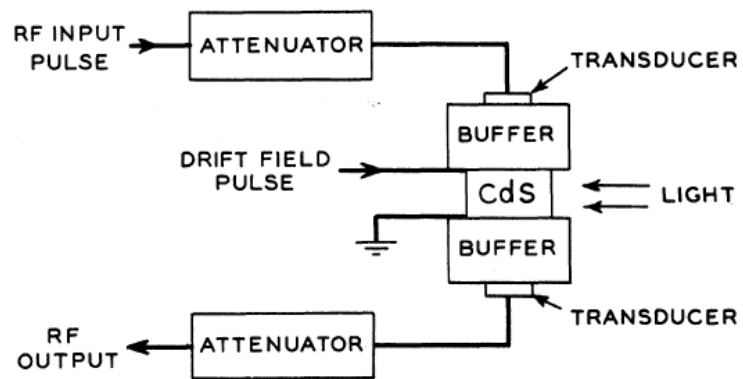


Fig. A 2 : Experimental arrangement for the first demonstration of acoustoelectric amplification of travelling waves in piezoelectric semiconductors (here CdS). (From Hutson *et al* [40]).

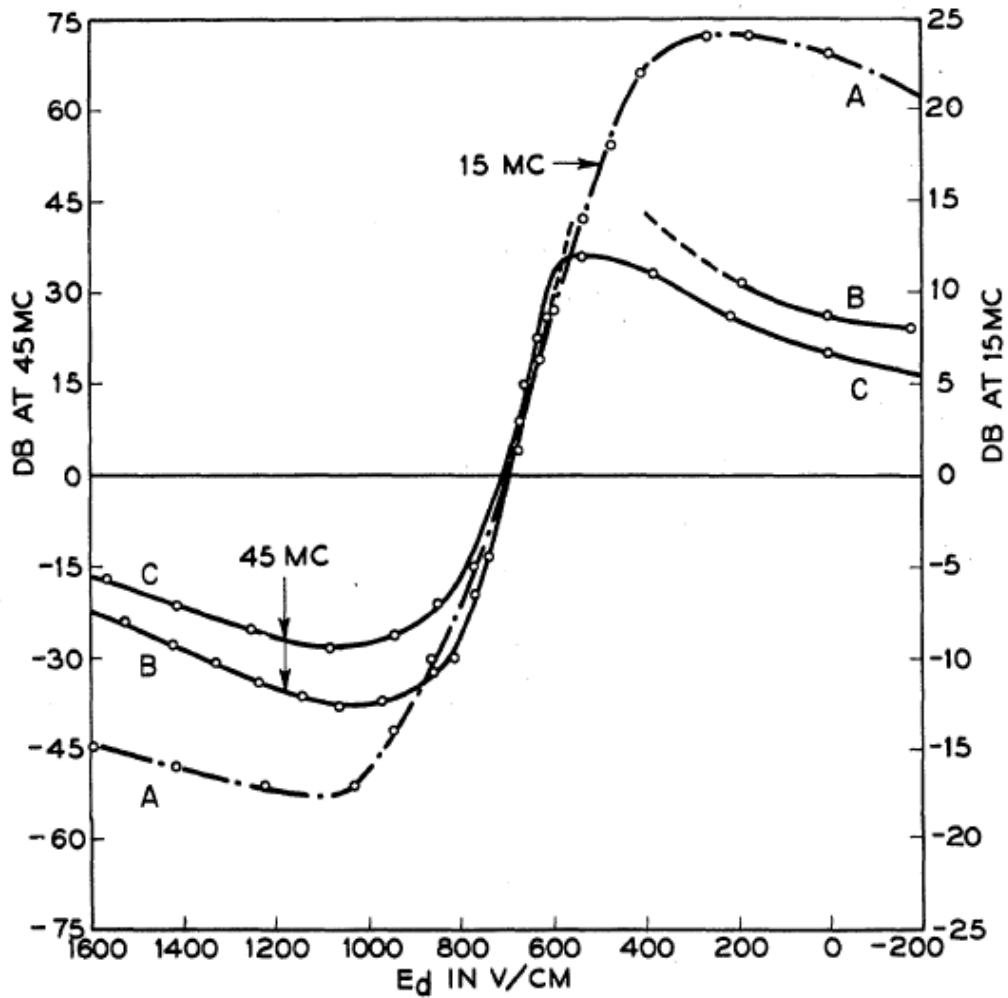


Fig. A 3 : The first experimental results on acoustoelectric amplification in a bulk piezoelectric semiconductor. (From Hutson et al [40]). The data show the amplification of a 45 MHz ultrasonic (travelling wave) signal applied to a 7 mm thick crystal of CdS. With the increase in the DC electric fields, the acoustic loss decreased. Above a certain threshold, the attenuation was found to be negative, implying a net gain in the acoustic signal. This phenomenon was explained using phonon-electron interaction in bulk CdS.

Bibliography

- [1] A. Rogalski, "Infrared detectors: status and trends," *Progress in Quantum Electronics*, vol. 27, pp. 59-210, 2003.
- [2] P. W. Kruse, *Uncooled Thermal Imaging : Arrays, Systems, and Applications*. Bellingham, Wash., USA: SPIE Press, 2001.
- [3] L. Becker, "Influence of IR sensor technology on the military and civil defense," presented at the Proc. SPIE 6127, Quantum Sensing and Nanophotonic Devices III, San Jose, CA, 2006.
- [4] P. Martyniuk and A. Rogalski, "HOT infrared photodetectors," *Opto-Electronics Review*, vol. 21, pp. 239-257, 2013/06/01 2013.
- [5] R. A. Wood, "Monolithic Silicon Microbolometer Arrays," in *Semiconductors and Semimetals*. vol. 47, W. K. Paul and D. S. David, Eds., ed: Elsevier, 1997, pp. 43-121.
- [6] F. Niklaus, C. Vieider, and H. Jakobsen, "MEMS-based uncooled infrared bolometer arrays: a review," *Proc. SPIE*, vol. 6836, pp. 68360D-68360D, 2007.
- [7] P. R. Norton, "Infrared detectors in the next millennium," *Proc. SPIE*, vol. 3698, pp. 652-665, 1999.
- [8] A. D. Oliver and K. D. Wise, "A 1024-element bulk-micromachined thermopile infrared imaging array," *Sensors and Actuators A: Physical*, vol. 73, pp. 222-231, 1999.
- [9] P. Muralt, "Micromachined infrared detectors based on pyroelectric thin films," *Reports on Progress in Physics*, vol. 64, p. 1339, 2001.
- [10] J. R. Vig, R. L. Filler, and Y. Kim, "Uncooled IR imaging array based on quartz microresonators," *Journal of Microelectromechanical Systems*, vol. 5, pp. 131-137, Jun 1996.

- [11] Y. Kim and J. R. Vig, "Experimental results on a quartz microresonator IR sensor," *Proceedings IEEE Ultrasonics Symposium* pp. 449-453, 1997.
- [12] Y. Kim and J. R. Vig, "Experimental results on a quartz microresonator IR sensor," in *Proceedings IEEE Ultrasonics Symposium*, 1997, pp. 449-453.
- [13] P. Kao and S. Tadigadapa, "Micromachined quartz resonator based infrared detector array," *Sensors and Actuators A: Physical*, vol. 149, pp. 189-192, 2009.
- [14] P. Kao, D. Allara, and S. Tadigadapa, "Fabrication and performance characteristics of high-frequency micromachined bulk acoustic wave quartz resonator arrays," *Measurement Science & Technology*, vol. 20, Dec 2009.
- [15] J. R. Vig, R. L. Filler, and Y. Kim, "Microresonator sensor arrays," *Proc. IEEE Frequency Control Symposium*, pp. 852-869, 1995.
- [16] J. R. Vig, R. L. Filler, and Y. Kim, "Uncooled IR imaging array based on quartz microresonators," *IEEE Journal of Microelectromechanical Systems (JMEMS)*, vol. 5, pp. 131-137, 1996.
- [17] C. Chen, X. Yi, J. Zhang, and B. Xiong, "Micromachined uncooled IR bolometer linear array using VO₂ thin films," *International Journal of Infrared and Millimeter Waves*, vol. 22, pp. 53-58, 2001.
- [18] V. Thakar and M. Rais-Zadeh, "Temperature-compensated piezoelectrically actuated Lamé-mode resonators," in *IEEE MEMS*, 2014, pp. 214-217.
- [19] V. A. Thakar, Z. Wu, A. Peczkalski, and M. Rais-Zadeh, "Piezoelectrically Transduced Temperature-Compensated Flexural-Mode Silicon Resonators," *IEEE Journal of Microelectromechanical Systems (JMEMS)*, vol. 22, pp. 815-823, 2013.
- [20] J. H. Lee, I. Bargatin, T. O. Gwinn, M. Vincent, K. A. Littau, R. Maboudian, *et al.*, "Microfabricated silicon carbide thermionic energy converter for solar electricity generation," in *IEEE MEMS*, Paris, France, 2012, pp. 1261-1264.
- [21] M. Shossig, "Optical absorption layers for infrared radiation," in *Bio and Nano Packaging Techniques for Electron Devices*, G. Gerlach and K.-J. Wolter, Eds., ed Heidelberg: Springer Verlag, Berlin, 2012, pp. 355-381.
- [22] N. Liu, M. Mesch, T. Weiss, M. Hentschel, and H. Giessen, "Infrared perfect absorber and its application as plasmonic sensor," *Nano Letters*, vol. 10, pp. 2342-2348, Jul 2010.
- [23] G. K. Mor, S. Kim, M. Paulose, O. K. Varghese, K. Shankar, J. Basham, *et al.*, "Visible to near-infrared light harvesting in TiO₂ nanotube array-P3HT based heterojunction solar cells," *Nano Letters*, vol. 9, pp. 4250-7, Dec 2009.

- [24] V. J. Gokhale and M. Rais-Zadeh, "Phonon-Electron Interactions in Piezoelectric Semiconductor Bulk Acoustic Wave Resonators," *Sci. Rep.*, vol. 4, pp. 5617:1-5617:10, 2014.
- [25] A. Akhieser, "On the absorption of sound in solids," *Journal of Physics*, vol. 1, pp. 277-287, 1939.
- [26] V. B. Braginsky and V. P. Mitrofanov, in *Systems with Small Dissipation*, K. S. Thorne, Ed., ed Chicago, IL, USA: The University of Chicago Press, pp. 1-42.
- [27] S. Ghaffari, S. A. Chandorkar, S. Wang, E. J. Ng, C. H. Ahn, H. Vu, *et al.*, "Quantum Limit of Quality Factor in Silicon Micro and Nano Mechanical Resonators," *Scientific Reports*, vol. 3, Nov 19 2013.
- [28] S. Chandorkar, M. Agarwal, R. Melamud, R. Candler, K. Goodson, and T. Kenny, "Limits of quality factor in bulk-mode micromechanical resonators," in *Int. Conf. on MEMS*, 2008, pp. 74-77.
- [29] V. T. Srikar and S. D. Senturia, "Thermoelastic damping in fine-grained polysilicon flexural beam resonators," *IEEE Journal of Microelectromechanical Systems*, vol. 11, pp. 499-504, 2002.
- [30] A. Duwel, R. N. Candler, T. W. Kenny, and M. Varghese, "Engineering MEMS Resonators With Low Thermoelastic Damping," *IEEE Journal of Microelectromechanical Systems (JMEMS)*, vol. 15, pp. 1437-1445, 2006.
- [31] R. Tabrizian, M. Rais-Zadeh, and F. Ayazi, "Effect of phonon interactions on limiting the f.Q product of micromechanical resonators," in *International Solid-State Sensors, Actuators and Microsystems Conference, (TRANSDUCERS 2009)*, 2009, pp. 2131-2134.
- [32] A. Akhieser, "On the absorption of sound in metals," *Journal of Physics*, vol. 1, pp. 289-297, 1939.
- [33] G. Weinreich and H. G. White, "Observation of the Acoustoelectric Effect," *Physical Review*, vol. 106, pp. 1104-1106, 1957.
- [34] V. E. Henrich and G. Weinreich, "Pulsed Ultrasonic Studies of Acoustoelectric Effect Ultrasonic Attenuation and Trapping in CdS," *Physical Review*, vol. 178, pp. 1204-1217, 1969.
- [35] M. Pomerantz, "Ultrasonic Loss and Gain Mechanisms in Semiconductors," *Proc. IEEE*, vol. 53, pp. 1438-1451, 1965.
- [36] Y. V. Gulyaev and F. S. Hickernell, "Acoustoelectronics: History, present state, and new ideas for a new era," *Journal of Acoustical Physics*, vol. 51, pp. 81-88, Jan-Feb 2005.
- [37] F. S. Hickernell, "The piezoelectric semiconductor and acoustoelectronic device development in the sixties," *IEEE Transactions on Ultrasonics, Ferroelectrics and Frequency Control*, vol. 52, pp. 737-745, 2005.

- [38] H. J. Mcskimin, A. R. Hutson, and T. B. Bateman, "Some Measurements of Wave Velocities and Elastic Moduli for Cadmium Sulphide," *Journal of the Acoustical Society of America*, vol. 33, pp. 856-862, 1961.
- [39] A. R. Hutson and D. L. White, "Elastic Wave Propagation in Piezoelectric Semiconductors," *Journal of Applied Physics*, vol. 33, pp. 40-47, 1962.
- [40] A. R. Hutson, D. L. White, and J. H. Mcfee, "Ultrasonic Amplification in CdS," *Physical Review Letters*, vol. 7, pp. 237-240, 1961.
- [41] D. L. White, "Amplification of Ultrasonic Waves in Piezoelectric Semiconductors," *Journal of Applied Physics*, vol. 33, pp. 2547-2554, 08/00/ 1962.
- [42] V. J. Gokhale, Y. Sui, and M. Rais-Zadeh, "Novel uncooled detector based on gallium nitride micromechanical resonators," in *Proc. SPIE: Infrared Technology and Applications*, Baltimore, MD, 2012, p. 835319.
- [43] Y. Sui, V. J. Gokhale, O. A. Shenderova, G. G. McGuire, and M. Rais-Zadeh, "A Thin-Film Infrared Absorber using CNT/Nanodiamond Nanocomposite," in *MRS Proceedings*, San Francisco, 2012, pp. ff05-04.
- [44] K. Mizuno, J. Ishii, H. Kishida, Y. Hayamizu, S. Yasuda, D. N. Futaba, *et al.*, "A black body absorber from vertically aligned single-walled carbon nanotubes," *Proc Natl Acad Sci U S A*, vol. 106, pp. 6044-7, Apr 2009.
- [45] J. Lehman, E. Theocharous, G. Eppeldauer, and C. Pannell, "Gold-black coatings for freestanding pyroelectric detectors," *Measurement Sci. & Tech.*, vol. 14, pp. 916-922, Jul 2003.
- [46] V. J. Gokhale, O. A. Shenderova, G. E. McGuire, and M. Rais-Zadeh, "Infrared Absorption Properties of Carbon Nanotube/Nanodiamond Based Thin Film Coatings," *IEEE Journal of Microelectromechanical Systems (JMEMS)*, vol. 23, pp. 191-197, 2014.
- [47] V. J. Gokhale, P. D. Myers, and M. Rais-Zadeh, "Subwavelength Plasmonic Absorbers for Spectrally Selective Resonant Infrared Detectors," presented at the IEEE Sensors, Valencia, Spain, 2014.
- [48] A. D. Bykhovski, V. V. Kaminski, M. S. Shur, Q. C. Chen, and M. A. Khan, "Pyroelectricity in gallium nitride thin films," *Applied Physics Letters*, vol. 69, p. 3254, 1996.
- [49] M. S. Shur, A. D. Bykhovski, and R. Gaska, "Pyroelectric and Piezoelectric Properties of Gan-Based Materials," *MRS Online Proceedings Library*, vol. 537, 1998.
- [50] I. L. Guy, S. Muensit, and E. M. Goldys, "Electrostriction in gallium nitride," *Applied Physics Letters*, vol. 75, pp. 3641-3643, 12/06/ 1999.

- [51] M. Willatzen and B. Lassen, "Nonlinearities and piezoelectric fields in AlN/GaN wurtzite heterostructures," *Journal of Applied Physics*, vol. 100, p. 124309, 2006.
- [52] M. Willatzen, B. Lassen, L. C. L. Y. Voon, and R. V. N. Melnik, "Dynamic coupling of piezoelectric effects, spontaneous polarization, and strain in lattice-mismatched semiconductor quantum-well heterostructures," *Journal of Applied Physics*, vol. 100, Jul 15 2006.
- [53] M. Willatzen and L. C. Lew Yan Voon, "Static and dynamic effects due to electrostriction in GaN/AlN," *Journal of Physics: Condensed Matter*, vol. 19, 2007.
- [54] M. Willatzen, L. Wang, and L. C. Lew Yan Voon, "Electrostriction in GaN/AlN heterostructures," *Superlattices and Microstructures*, vol. 43, pp. 436-440, 2008.
- [55] M. Willatzen and L. C. L. Y. Voon, "Static and dynamic effects due to electrostriction in GaN/AlN," *Journal of Physics: Condensed Matter*, vol. 19, p. 506202, 2007.
- [56] R. Quay, C. Moglestue, V. Palankovski, and S. Selberherr, "A temperature dependent model for the saturation velocity in semiconductor materials," *Materials Science in Semiconductor Processing*, vol. 3, pp. 149-155, 3/1/ 2000.
- [57] A. Rogalski, "Infrared detectors for the future," *Acta Physica Polonica-Series A General Physics*, vol. 116, p. 389, 2009.
- [58] V. J. Gokhale, O. A. Shenderova, G. E. McGuire, and M. Rais-Zadeh, "Infrared Absorption Properties of Carbon Nanotube/Nanodiamond Based Thin Film Coatings," *IEEE Journal of Microelectromechanical Systems*, accepted, to be published 2013.
- [59] A. N. Cleland and M. L. Roukes, "Noise processes in nanomechanical resonators," *Journal of Applied Physics*, vol. 92, pp. 2758-2769, Sep 1 2002.
- [60] F. L. Walls and J. R. Vig, "Fundamental Limits on the Frequency Stabilities of Crystal-Oscillators," *IEEE Transactions on Ultrasonics Ferroelectrics and Frequency Control*, vol. 42, pp. 576-589, Jul 1995.
- [61] H. J. Lee, K. K. Park, P. Cristman, O. Oralkan, M. Kupnik, and B. T. Khuri-Yakub, "A Low-Noise Oscillator based on a Multi-Membrane CMUT for High Sensitivity Resonant Chemical Sensors," in *IEEE Micro Electro Mechanical Systems*, 2009, pp. 761-764.
- [62] J. E. Y. Lee, B. Bahreyni, Z. Yong, and A. A. Seshia, "A Single-Crystal-Silicon Bulk-Acoustic-Mode Microresonator Oscillator," *Electron Device Letters, IEEE*, vol. 29, pp. 701-703, 2008.
- [63] V. J. Gokhale and M. Rais-Zadeh, "Uncooled Infrared Detectors Using Gallium Nitride on Silicon Micromechanical Resonators," *IEEE Journal of Microelectromechanical Systems (JMEMS)*, vol. accepted Dec 2013, in press, 2013.

- [64] V. J. Gokhale, J. Roberts, and M. Rais-Zadeh, "High performance bulk mode gallium nitride resonators and filters," in *16th International Solid-State Sensors, Actuators and Microsystems Conference (Transducers 2011)*, Beijing, 2011, pp. 926-929.
- [65] G. Piazza, P. J. Stephanou, and A. P. Pisano, "Piezoelectric aluminum nitride vibrating contour-mode MEMS resonators," *Journal of Microelectromechanical Systems*, vol. 15, pp. 1406-1418, Dec 2006.
- [66] M. Rais-Zadeh, V. J. Gokhale, A. Ansari, M. Faucher, D. Theron, Y. Cordier, *et al.*, "Gallium Nitride as an Electromechanical Material," *IEEE Journal of Microelectromechanical Systems (JMEMS)*, vol. under review, 2014.
- [67] T. R. Albrecht, P. Grutter, D. Horne, and D. Rugar, "Frequency-Modulation Detection Using High-Q Cantilevers for Enhanced Force Microscope Sensitivity," *Journal of Applied Physics*, vol. 69, pp. 668-673, Jan 15 1991.
- [68] M. Liger, "Uncooled Carbon Microbolometer Imager," PhD Doctoral Thesis, California Institute of Technology, Pasadena, CA, 2006.
- [69] K. Stephan and A. Laesecke, "The Thermal Conductivity of Fluid Air," *Journal of Physical and Chemical Reference Data*, vol. 14, pp. 227-234, 1985.
- [70] M. Kohin and N. R. Butler, "Performance limits of uncooled VOx microbolometer focal plane arrays," *Proc. SPIE*, vol. 5406, pp. 447-453, 2004.
- [71] V. J. Gokhale and M. Rais-Zadeh, "Sensitive uncooled IR detectors using gallium nitride resonators and silicon nitride absorbers," presented at the Solid-State Sensors, Actuators and Microsystems Workshop, Hilton Head, SC, 2012.
- [72] C. M. Jha, G. Bahl, R. Melamud, S. A. Chandorkar, M. A. Hopcroft, B. Kim, *et al.*, "High resolution microresonator-based digital temperature sensor," *Applied Physics Letters*, vol. 91, pp. 074101-3, 08/13/ 2007.
- [73] C. Cabuz, S. Shoji, K. Fukatsu, E. Cabuz, K. Minami, and M. Esashi, "Fabrication and packaging of a resonant infrared sensor integrated in silicon," *Sensors and Actuators A: Physical*, vol. 43, pp. 92-99, 5// 1994.
- [74] J. R. C. Wan-Thai Hsu, and Clark T.-C. Nguyen, "A resonant temperature sensor based on electrical spring softening," presented at the 11th Int. Conf. on Solid-State Sensors & Actuators (Transducers'01), Munich, Germany, 2001.
- [75] Y. Hui and M. Rinaldi, "Fast and high resolution thermal detector based on an aluminum nitride piezoelectric microelectromechanical resonator with an integrated suspended heat absorbing element," *Applied Physics Letters*, vol. 102, pp. 093501-4, 4 March 2013.

- [76] Y. Hui, Z. Qian, G. Hummel, and M. Rinaldi, "Pico-watts range uncooled infrared detector based on a freestanding piezoelectric resonant microplate with nanoscale metal anchors," presented at the Solid-State Sensors, Actuators and Microsystems Workshop, Hilton Head Island, South Carolina, 2014.
- [77] A. Ansari, V. J. Gokhale, V. A. Thakar, J. Roberts, and M. Rais-Zadeh, "Gallium nitride-on-silicon micromechanical overtone resonators and filters," in *IEEE Electron Device Meeting (IEDM'11)*, Washington, DC, 2011, pp. 20.3.1 - 20.3.4.
- [78] T. Boström, G. Westin, and E. Wäckelgård, "Optimization of a solution-chemically derived solar absorbing spectrally selective surface," *Solar energy materials and solar cells*, vol. 91, pp. 38-43, 2007.
- [79] W. Lang, K. Kuhl, and H. Sandmaier, "Absorbing layers for thermal infrared detectors," in *Solid State Sensors and Actuators*, San Francisco, CA, 1991, pp. 635-638.
- [80] M. Gradhand and O. Breitenstein, "Preparation of nonconducting infrared-absorbing thin films," *Review of Scientific Instruments*, vol. 76, p. 053702, 2005.
- [81] I. Mellouki, N. Bennaji, and N. Yacoubi, "IR characterization of graphite black-coating for cryogenic detectors," *Infrared physics & technology*, vol. 50, pp. 58-62, 2007.
- [82] I. Mellouki, O. Touayar, T. Ktari, and N. Yacoubi, "Deposition and characterization of graphite-black coating for absolute pyroelectric detectors," *Infrared physics & technology*, vol. 45, pp. 273-279, 2004.
- [83] J. Lehman, A. Sanders, L. Hanssen, B. Wilthan, J. Zeng, and C. Jensen, "Very black infrared detector from vertically aligned carbon nanotubes and electric-field poling of lithium tantalate," *Nano-Letters*, vol. 10, pp. 3261-3266, Aug 2010.
- [84] H. Shi, J. G. Ok, H. W. Baac, and L. J. Guo, "Low density carbon nanotube forest as an index-matched and near perfect absorption coating," *Appl. Phys. Lett.*, vol. 99, p. 211103, Nov 2011.
- [85] C. Koechlin, S. Maine, S. Rennesson, R. Haidar, B. Tretout, J. Jaeck, *et al.*, "Potential of carbon nanotubes films for infrared bolometers," in *Proc. SPIE*, San Francisco, 2011, p. 794521.
- [86] P. Merel, J. B. A. Kpetsu, C. Koechlin, S. Maine, R. Haidar, J. L. Pelouard, *et al.*, "Infrared sensors based on multi-wall carbon nanotube films," *Comptes Rendus Physique*, vol. 11, pp. 375-380, Jul 2010.
- [87] S. Maine, C. Koechlin, S. Rennesson, J. Jaeck, S. Salort, B. Chassagne, *et al.*, "Complex optical index of single wall carbon nanotube films from the near-infrared to the terahertz spectral range," *Applied Optics*, vol. 51, pp. 3031-5, May 2012.
- [88] Á. Kukovecz, R. Smajda, M. Óze, H. Haspel, Z. Kónya, and I. Kiricsi, "Pyroelectric temperature sensitization of multi-wall carbon nanotube papers," *Carbon*, vol. 46, pp. 1262-1265, Aug 2008.

- [89] J. H. Lehman, K. E. Hurst, A. M. Radojevic, A. C. Dillon, and R. M. Osgood, Jr., "Multiwall carbon nanotube absorber on a thin-film lithium niobate pyroelectric detector," *Optics Letters*, vol. 32, pp. 772-4, Apr 2007.
- [90] Y. Sui, V. J. Gokhale, O. A. Shenderova, G. E. McGuire, and M. Rais-Zadeh, "A thin-film infrared absorber using CNT/nanodiamond nanocomposite," *MRS Proceedings*, vol. 1452, pp. ff05-04, May 2012.
- [91] V. J. Gokhale, Y. Sui, and M. Rais-Zadeh, "Novel uncooled detector based on gallium nitride micromechanical resonators," *Infrared Technology and Applications Xxxviii, Pts 1 and 2*, vol. 8353, p. 835319, 2012.
- [92] A. Martinez, S. Uchida, Y.-W. Song, T. Ishigure, and S. Yamashita, "Fabrication of carbon nanotube-poly-methylmethacrylate composites for nonlinear photonic devices," *Optics Express*, vol. 16, pp. 11337-11343, Jul 2008.
- [93] S. C. Hens, G. Cunningham, G. McGuire, and O. Shenderova, "Nanodiamond-assisted dispersion of carbon nanotubes and hybrid nanocarbon-based composites," *Nanoscience and Nanotechnology Letters*, vol. 3, pp. 75-82, Feb 2011.
- [94] X. J. Wang, J. D. Flicker, B. J. Lee, W. J. Ready, and Z. M. Zhang, "Visible and near-infrared radiative properties of vertically aligned multi-walled carbon nanotubes," *Nanotechnology*, vol. 20, p. 215704, May 27 2009.
- [95] H. Ye, X. J. Wang, W. Lin, C. P. Wong, and Z. M. Zhang, "Infrared absorption coefficients of vertically aligned carbon nanotube films," *Appl. Phys. Lett.*, vol. 101, Oct 1 2012.
- [96] F. J. Garcia-Vidal, J. M. Pitarke, and J. B. Pendry, "Effective medium theory of the optical properties of aligned carbon nanotubes," *Physics Review Letters*, vol. 78, pp. 4289-4292, Jun 1997.
- [97] P. Christensen, B. Jakosky, H. Kieffer, M. Malin, H. McSween, Jr., K. Neelson, *et al.*, "The Thermal Emission Imaging System (THEMIS) for the Mars 2001 Odyssey Mission," *Space Science Reviews*, vol. 110, pp. 85-130, 2004/01/01 2004.
- [98] C. Wu, B. Neuner, G. Shvets, J. John, A. Milder, B. Zollars, *et al.*, "Large-area wide-angle spectrally selective plasmonic absorber," *Physical Review B*, vol. 84, p. 075102, 08/01/ 2011.
- [99] C. Koechlin, P. Bouchon, F. Pardo, J.-L. Pelouard, and R. Haïdar, "Analytical description of subwavelength plasmonic MIM resonators and of their combination," *Optics express*, vol. 21, pp. 7025-7032, 2013.
- [100] R. Gordon, "Light in a subwavelength slit in a metal: Propagation and reflection," *Physical Review B*, vol. 73, p. 153405, 2006.
- [101] M. G. Nielsen, D. K. Gramotnev, A. Pors, O. Albrektsen, and S. I. Bozhevolnyi, "Continuous layer gap plasmon resonators," *Optics express*, vol. 19, pp. 19310-19322, 2011.

- [102] K. Aydin, V. E. Ferry, R. M. Briggs, and H. A. Atwater, "Broadband polarization-independent resonant light absorption using ultrathin plasmonic super absorbers," *Nature Communications*, vol. 2, Nov 2011.
- [103] A. D. Hanser and K. R. Evans, "Development of the Bulk GaN Substrate Market," in *Technology of Gallium Nitride Crystal Growth*. vol. 133, D. Ehrentraut, E. Meissner, and M. Bockowski, Eds., ed: Springer Berlin Heidelberg, 2010, pp. 3-27.
- [104] V. Cimalla, J. Pezoldt, and O. Ambacher, "Group III nitride and SiC based MEMS and NEMS: materials properties, technology and applications," *Journal of Physics D: Applied Physics*, vol. 40, p. 6386, 2007.
- [105] S. Nakamura and M. R. Krames, "History of Gallium Nitride-Based Light-Emitting Diodes for Illumination," *Proceedings of the IEEE*, vol. 101, pp. 2211-2220, 2013.
- [106] N. Chaaben, T. Boufaden, A. Fouzri, M. S. Bergaoui, and B. E. Jani, "High resolution X-ray diffraction of GaN grown on Si (1 1 1) by MOVPE," *Applied Surface Science*, vol. 253, pp. 241-245, 10/31/ 2006.
- [107] S. J. Pearton, R. J. Shul, G. F. McLane, and C. Constantine, "Reactive ion etching of III-V nitrides," *Solid-State Electronics*, vol. 41, pp. 159-163, 2// 1997.
- [108] V. J. Gokhale, Y. Shim, and M. Rais-Zadeh, "Observation of the Acoustoelectric Effect in Gallium Nitride Micromechanical Bulk Acoustic Filters," in *IEEE International Frequency Control Symposium (IFCS 2010)*, 2010, pp. 524-529.
- [109] V. J. Gokhale, J. Roberts, and M. Rais-Zadeh, "High-performance bulk-mode gallium nitride resonators and filters," in *International Conference on Solid-State Sensors, Actuators and Microsystems (Transducers'11)*, Beijing, China, 2011.
- [110] A. Ansari, V. J. Gokhale, V. A. Thakar, J. Roberts, and M. Rais-Zadeh, "Gallium Nitride-on-Silicon Micromechanical Overtone Resonators and Filters," *IEEE International Electron Devices Meeting (IEDM)*, 2011.
- [111] A. Ansari and M. Rais-Zadeh, "HEMT-based read-out of a thickness-mode AlGaIn/GaN resonator," in *IEEE International Electron Devices Meeting (IEDM)*, 2013, pp. 18.3.1-18.3.4.
- [112] A. Ansari and M. Rais-Zadeh, "A Thickness-Mode AlGaIn/GaN Resonant Body High Electron Mobility Transistor," *IEEE Transactions on Electron Devices*, vol. under review, 2014.
- [113] A. Polian, M. Grimsditch, and I. Grzegory, "Elastic constants of gallium nitride," *Journal of Applied Physics*, vol. 79, pp. 3343-3344, 03/15/ 1996.
- [114] J. Kolník, Ī. H. Oğuzman, K. F. Brennan, R. Wang, P. P. Ruden, and Y. Wang, "Electronic transport studies of bulk zincblende and wurtzite phases of GaN based on an ensemble Monte

- Carlo calculation including a full zone band structure," *Journal of Applied Physics*, vol. 78, pp. 1033-1038, 1995.
- [115] A. F. Wright, "Elastic properties of zinc-blende and wurtzite AlN, GaN, and InN," *Journal of Applied Physics*, vol. 82, pp. 2833-2839, 1997.
- [116] M. Yamaguchi, T. Yagi, T. Azuhata, T. Sota, K. Suzuki, S. Chichibu, *et al.*, "Brillouin scattering study of gallium nitride: elastic stiffness constants," *Journal of Physics: Condensed Matter*, vol. 9, p. 241, 1997.
- [117] M. Martyniuk, G. Parish, H. Marchand, P. T. Fini, S. P. DenBaars, and L. Faraone, "Nanoindentation of laterally overgrown epitaxial gallium nitride," *Electronic Materials Letters*, vol. 8, pp. 111-115, 2012/04/01 2012.
- [118] W. C. Oliver and G. M. Pharr, "An improved technique for determining hardness and elastic modulus using load and displacement sensing indentation experiments," *Journal of materials research*, vol. 7, pp. 1564-1583, 1992.
- [119] M. D. Drory, J. W. Ager, T. Suski, I. Grzegory, and S. Porowski, "Hardness and fracture toughness of bulk single crystal gallium nitride," *Applied Physics Letters*, vol. 69, pp. 4044-4046, 1996.
- [120] R. Nowak, M. Pessa, M. Suganuma, M. Leszczynski, I. Grzegory, S. Porowski, *et al.*, "Elastic and plastic properties of GaN determined by nano-indentation of bulk crystal," *Applied Physics Letters*, vol. 75, pp. 2070-2072, 1999.
- [121] G. Yu, H. Ishikawa, T. Egawa, T. Soga, J. Watanabe, T. Jimbo, *et al.*, "Mechanical properties of the GaN thin films deposited on sapphire substrate," *Journal of Crystal Growth*, vol. 189-190, pp. 701-705, 6/15/ 1998.
- [122] S. O. Kucheyev, J. E. Bradby, J. S. Williams, C. Jagadish, M. Toth, M. R. Phillips, *et al.*, "Nanoindentation of epitaxial GaN films," *Applied Physics Letters*, vol. 77, pp. 3373-3375, 2000.
- [123] C.-H. Tsai, S.-R. Jian, and J.-Y. Juang, "Berkovich nanoindentation and deformation mechanisms in GaN thin films," *Applied Surface Science*, vol. 254, pp. 1997-2002, 1/30/ 2008.
- [124] A. Guedes, S. Shelton, R. Przybyla, I. Izyumin, B. Boser, and D. A. Horsley, "Aluminum nitride pMUT based on a flexurally-suspended membrane," in *Solid-State Sensors, Actuators and Microsystems Conference (TRANSDUCERS), 2011 16th International*, 2011, pp. 2062-2065.
- [125] P. Murali and J. Baborowski, "Micromachined Ultrasonic Transducers and Acoustic Sensors Based on Piezoelectric Thin Films," *Journal of Electroceramics*, vol. 12, pp. 101-108, 2004/01/01 2004.

- [126] L. C. Popa and D. Weinstein, "2DEG electrodes for piezoelectric transduction of AlGaIn/GaN MEMS resonators," in *European Frequency and Time Forum & International Frequency Control Symposium (EFTF/IFC), 2013 Joint*, 2013, pp. 922-925.
- [127] L. C. Popa and D. Weinstein, "Switchable piezoelectric transduction in AlGaIn/GaN MEMS resonators," in *Solid-State Sensors, Actuators and Microsystems (TRANSDUCERS & EUROSENSORS XXVII), 2013 Transducers & Eurosensors XXVII: The 17th International Conference on*, 2013, pp. 2461-2464.
- [128] A. Ansari, V. J. Gokhale, J. Roberts, and M. Rais-Zadeh, "Monolithic integration of GaN-based micromechanical resonators and HEMTs for timing applications," in *IEEE International Electron Devices Meeting (IEDM)*, 2012, pp. 15.5.1-15.5.4.
- [129] R. Abdolvand and F. Ayazi, "Enhanced Power Handling and Quality Factor in Thin-Film Piezoelectric-on-Substrate Resonators," in *IEEE Ultrasonics Symposium*, 2007, pp. 608-611.
- [130] R. Abdolvand, H. M. Lavasani, G. K. Ho, and F. Ayazi, "Thin-Film Piezoelectric-on-Silicon Resonators for High-Frequency Reference Oscillator Applications," *IEEE Transactions on Ultrasonics Ferroelectrics and Frequency Control*, vol. 55, pp. 2596-2606, Dec 2008.
- [131] G. K. Ho, R. Abdolvand, A. Sivapurapu, S. Humad, and F. Ayazi, "Piezoelectric-on-silicon lateral bulk acoustic wave micromechanical resonators," *IEEE Journal of Microelectromechanical Systems (JMEMS)*, vol. 17, pp. 512-520, Apr 2008.
- [132] R. Abdolvand and F. Ayazi, "High-frequency monolithic thin-film piezoelectric-on-substrate filters," *International Journal of Microwave and Wireless Technologies*, vol. 1, pp. 29-35, Feb 2009.
- [133] A. Muller, D. Neculoiu, G. Konstantinidis, A. Stavrinidis, D. Vasilache, A. Cismaru, *et al.*, "6.3-GHz Film Bulk Acoustic Resonator Structures Based on a Gallium Nitride/Silicon Thin Membrane," *IEEE Electron Device Letters*, vol. 30, pp. 799-801, Aug 2009.
- [134] L. Popa and D. Weinstein, "L-Band Lamb Mode Resonators in Gallium Nitride MMIC Technology," in *IEEE International Frequency Control Symposium*, Taipei, Taiwan, 2014.
- [135] A. Ansari and M. Rais-Zadeh, "An 8.7 GHz GaN micromechanical resonator with an integrated AlGaIn/GaN HEMT," in *Solid-State Sensors, Actuators and Microsystems Workshop (Hilton Head)*, Hilton Head Island, SC, USA, 2014.
- [136] "IEEE Standard on Piezoelectricity," *ANSI/IEEE Std 176-1987*, pp. 1-60, 1988.
- [137] J. Kaitila, "BAW Device Basics," in *RF Bulk Acoustic Wave Filters for Communications*, K.-y. Hashimoto, Ed., ed Norwood, MA: Artech House, 2009, pp. 51-90.
- [138] V. Siklitsky. (1998, 11/30/2013). *Semiconductors on NSM-Gallium Nitride (1998 ed.)*. Available: <http://www.ioffe.ru/SVA/NSM/>

- [139] S. Y. Mensah, N. G. Mensah, V. W. Elloh, G. K. Banini, F. Sam, and F. K. A. Allotey, "Propagation of ultrasonic waves in bulk gallium nitride (GaN) semiconductor in the presence of high-frequency electric field," *Physica E-Low-Dimensional Systems & Nanostructures*, vol. 28, pp. 500-506, Sep 2005.
- [140] R. Wang, S. A. Bhave, and K. Bhattacharjee, "High kt $2 \times Q$, multi-frequency Lithium Niobate Resonators," in *IEEE MEMS*, 2013, p. 165.
- [141] R. Ruby, P. Bradley, J. Larson, III, Y. Oshmyansky, and D. Figueredo, "Ultra-miniature high-Q filters and duplexers using FBAR technology," in *Solid-State Circuits Conference, 2001. Digest of Technical Papers. ISSCC. 2001 IEEE International*, 2001, pp. 120-121.
- [142] A. Ansari, V. J. Gokhale, J. Roberts, and M. Rais-Zadeh, "Monolithic integration of GaN-based micromechanical resonators and HEMTs for timing applications," in *IEEE International Electron Devices Meeting (IEDM 2012)*, 2012, pp. 15.5.1-15.5.4.
- [143] C. D. Nordquist and R. H. Olsson, "Power handling and intermodulation distortion of contour-mode AlN MEMS resonators and filters," in *Microwave Symposium Digest (MTT), 2011 IEEE MTT-S International*, 2011, pp. 1-4.
- [144] D. Royer and E. Dieulesaint, *Elastic Waves in Solids I: Free and Guided Propagation* vol. I. Berlin: Springer-Verlag, 2000.
- [145] N. Lobontiu, *Mechanical Design of Microresonators : Modeling and Applications*. New York: McGraw-Hill, 2006.
- [146] V. T. Srikar and S. D. Senturia, "Thermoelastic damping in fine-grained polysilicon flexural beam resonators," *J. Microelectromech. Syst.*, vol. 11, pp. 499-504, 2002.
- [147] Z. Hao and F. Ayazi, "Support loss in the radial bulk-mode vibrations of center-supported micromechanical disk resonators," *Sensors and Actuators A: Physical*, vol. 134, pp. 582-593, 15 March 2007.
- [148] J. D. Maines and E. G. S. Paige, "High-frequency acoustoelectric currents and departures from Ohm's law in thin platelets of CdS I. Linear behaviour," *Journal of Physics C: Solid State Physics*, vol. 2, p. 175, 1969.
- [149] P. Perlin, C. Jaubertie-Carillon, J. P. Itie, A. San Miguel, I. Grzegory, and A. Polian, "Raman scattering and x-ray-absorption spectroscopy in gallium nitride under high pressure," *Physical Review B*, vol. 45, pp. 83-89, 01/01/ 1992.
- [150] E. A. Henriksen, S. Syed, Y. Ahmadian, M. J. Manfra, K. W. Baldwin, A. M. Sergent, *et al.*, "Acoustic phonon scattering in a low density, high mobility AlGaIn/GaN field-effect transistor," *Applied Physics Letters*, vol. 86, pp. 252108-252108-3, 2005.

- [151] V. W. L. Chin, T. L. Tansley, and T. Osotchan, "Electron mobilities in gallium, indium, and aluminum nitrides," *Journal of Applied Physics*, vol. 75, pp. 7365-7372, 1994.
- [152] D. Pavlidis, "GaN Negative Differential Resistance Components with Terahertz Operation Capability: From Fundamentals to Devices," in *Optoelectronic Devices: III Nitrides*, M. Razeghi and M. Henini, Eds., ed Oxford: Elsevier, 2005, pp. 351-386.
- [153] V. T. Srikar and S. D. Senturia, "Thermoelastic damping in fine-grained polysilicon flexural beam resonators," *IEEE Journal of Microelectromechanical Systems*, vol. 11, pp. 499-504, 2002.
- [154] J. W. P. Hsu, M. J. Manfra, S. N. G. Chu, C. H. Chen, L. N. Pfeiffer, and R. J. Molnar, "Effect of growth stoichiometry on the electrical activity of screw dislocations in GaN films grown by molecular-beam epitaxy," *Applied Physics Letters*, vol. 78, pp. 3980-3982, Jun 18 2001.
- [155] D. C. Look and J. R. Sizelove, "Predicted maximum mobility in bulk GaN," *Applied Physics Letters*, vol. 79, pp. 1133-1135, 2001.
- [156] R. W. Smith, "Current Saturation in Piezoelectric Semiconductors," *Phys. Rev. Lett.*, vol. 9, pp. 87-90, 1962.
- [157] M. Faucher, A. Ben Amar, B. Grimbort, V. Brandli, M. Werquin, L. Buchailot, *et al.*, "GaN: A multifunctional material enabling MEMS resonators based on amplified piezoelectric detection," in *Joint Conference of the IEEE International Frequency Control and the European Frequency and Time Forum (FCS)*, 2011, pp. 1-5.
- [158] G. Piazza, P. J. Stephanou, and A. P. Pisano, "Piezoelectric aluminum nitride vibrating contour-mode MEMS resonators," *IEEE Journal of Microelectromechanical Systems*, vol. 15, pp. 1406-1418, Dec 2006.
- [159] W. Kun, W. Ark-Chew, and C. T. C. Nguyen, "VHF free-free beam high-Q micromechanical resonators," *IEEE Journal of Microelectromechanical Systems*, vol. 9, pp. 347-360, 2000.
- [160] N. Sepúlveda, J. Lu, D. M. Aslam, and J. P. Sullivan, "High-performance polycrystalline diamond micro-and nanoresonators," *IEEE Journal of Microelectromechanical Systems*, vol. 17, pp. 473-482, 2008.
- [161] B. K. Ridley, W. J. Schaff, and L. F. Eastman, "Hot-phonon-induced velocity saturation in GaN," *Journal of Applied Physics*, vol. 96, pp. 1499-1502, 2004.
- [162] J. D. Albrecht, R. P. Wang, P. P. Ruden, M. Farahmand, and K. F. Brennan, "Electron transport characteristics of GaN for high temperature device modeling," *Journal of Applied Physics*, vol. 83, pp. 4777-4781, 1998.
- [163] S. K. Abdelraheem, D. P. Blyth, and N. Balkan, "Amplification of ultrasonic waves in bulk GaN and AlGaIn/GaN heterostructures," *Physica Status Solidi a-Applications and Materials Science*, vol. 185, pp. 247-256, Jun 16 2001.

- [164] D. Jena, S. P. Alpay, and J. Mantese, "Functionally Graded Polar Heterostructures: New Materials for Multifunctional Devices," in *Polarization Effects in Semiconductors*, C. Wood and D. Jena, Eds., ed: Springer US, 2008, pp. 307-372.
- [165] Q. Z. Liu and S. S. Lau, "A review of the metal–GaN contact technology," *Solid-State Electronics*, vol. 42, pp. 677-691, 5/6/ 1998.
- [166] L. Dobos, B. Pécz, L. Tóth, Z. J. Horváth, Z. E. Horváth, A. Tóth, *et al.*, "Metal contacts to n-GaN," *Applied Surface Science*, vol. 253, pp. 655-661, 11/15/ 2006.
- [167] A. C. Schmitz, A. T. Ping, M. A. Khan, Q. Chen, J. W. Yang, and I. Adesida, "Metal contacts to n-type GaN," *Journal of Electronic Materials*, vol. 27, pp. 255-260, 1998/04/01 1998.
- [168] R. B. Karabalin, M. H. Matheny, X. L. Feng, E. Defay, G. Le Rhun, C. Marcoux, *et al.*, "Piezoelectric nanoelectromechanical resonators based on aluminum nitride thin films," *Applied Physics Letters*, vol. 95, Sep 7 2009.
- [169] D. C. Look, D. C. Reynolds, J. R. Sizelove, R. L. Jones, C. W. Litton, G. Cantwell, *et al.*, "Electrical properties of bulk ZnO," *Solid State Communications*, vol. 105, pp. 399-401, 1998.
- [170] D. C. Look, "Recent advances in ZnO materials and devices," *Materials Science and Engineering: B*, vol. 80, pp. 383-387, 22 March 2001.
- [171] J. D. Albrecht, P. P. Ruden, S. Limpijumnong, W. R. L. Lambrecht, and K. F. Brennan, "High field electron transport properties of bulk ZnO," *Journal of Applied Physics*, vol. 86, pp. 6864-6867, 1999.
- [172] S. Karmann, R. Helbig, and R. A. Stein, "Piezoelectric properties and elastic constants of 4H and 6H SiC at temperatures 4K-320K," *Journal of Applied Physics*, vol. 66, pp. 3922-3924, 1989.
- [173] *SiC Materials and Devices* vol. 1. Singapore: World Scientific Publishing Co., 2006.
- [174] I. A. Khan and J. A. Cooper, Jr., "Measurement of high-field electron transport in silicon carbide," *IEEE Transactions on Electron Devices*, vol. 47, pp. 269-273, 2000.
- [175] S. Adachi, *Physical Properties of III-V Semiconductor Compounds*. USA: John Wiley & Sons, 1992.
- [176] S. Adachi, *GaAs and related materials*. NJ, USA: World Scientific Publishing Co. , 1994.
- [177] J. D. Maines, F. G. Marshall, E. G. S. Paige, and R. A. Stuart, "Gigahertz acousto-electric oscillations in zinc oxide," *Physics Letters A*, vol. 26, pp. 388-389, 3/11/ 1968.

- [178] P. Mohanty, D. A. Harrington, K. L. Ekinci, Y. T. Yang, M. J. Murphy, and M. L. Roukes, "Intrinsic dissipation in high-frequency micromechanical resonators," *Physical Review B*, vol. 66, Aug 15 2002.
- [179] P. Mohanty, D. A. Harrington, and M. L. Roukes, "Measurement of small forces in micron-sized resonators," *Physica B*, vol. 284, pp. 2143-2144, Jul 2000.
- [180] A. R. Hutson, "Piezoelectric Scattering and Phonon Drag in ZnO and CdS," *Journal of Applied Physics*, vol. 32, pp. 2287-2296, 1961.
- [181] A. R. Hutson, "Acousto-Electric Explanation of Non-Ohmic Behavior in Piezoelectric Semiconductors and Bismuth," *Physical Review Letters*, vol. 9, pp. 296-302, 1962.